Finite Element Analysis of Insulated Railroad Joints

By

Anne K. Himebaugh

A Thesis submitted to the Faculty of the
Virginia Polytechnic Institute and State University
In partial fulfillment of the requirements for the degree of

Master of Science
In
Civil Engineering

Raymond H. Plaut, Chairman
David A. Dillard
Elisa D. Sotelino

November 28, 2006
Blacksburg, Virginia

Keywords: Insulated Railroad Joint, Finite Element, Elastic Foundation, Hertz Contact Theory
© Anne K. Himebaugh 2006

Finite Element Analysis of Insulated Railroad Joints

By Anne K. Himebaugh
Dr. Raymond H. Plaut, Chairman
Charles E. Via, Jr. Department of Civil and Environmental Engineering

(Abstract)

In recent years, the lifetime of an insulated railroad joint in the field has decreased due to increasing wheel loads. The goal of this research is to investigate possible changes in insulated rail joint design in order to improve the performance of the insulated joint. The finite element program ABAQUS is used to model the supported butt joint. In this model, the rail, joint bars, epoxy, and ties surrounding the joint are modeled using solid elements. The remaining ties are modeled as an elastic foundation. The rail is subjected to a tensile load, as well as a vertical wheel load that is applied to the rail using Hertz contact theory.

Parametric studies are performed by varying the tie width, joint bar length, and joint bar dimensions. Two different wheel load locations are also investigated: centered about the end post, and halfway between the tie under the end post and the tie just to the left of the end post.

The vertical displacement of the rail and insulated joint is one measure used to determine the effect of the parameters on the insulated joint. However, since the most common cause of failure in insulated rail joints is the debonding of the epoxy, this research also focuses on the stresses present in the epoxy when the joint is subjected to a static wheel load. The two out-of-plane shear stresses as well as the normal peel stress are used to compare the various designs of the joint.

Acknowledgements

I would like to thank all of those at Virginia Tech who have contributed to my education and have supported me through my graduate study. I would like to express my sincere gratitude to my advisor and committee chairman, Dr. Plaut, who placed his faith and guidance in me and encouraged me to work hard throughout this process. I would also like to thank my committee members: Dr. Dillard for his support, direction, and wonderful explanations to help me further understand the basics of my research; and Dr. Sotelino for her many recommendations and always cheerful words of wisdom.

I would also like to express my gratitude to Dave Davis and Muhammad Akhtar at TTCI, who provided their vast knowledge of railroad design to help me complete this research.

I will forever be grateful to the many educators who have given me such an incredible basis for my education, from my teachers at Turpin High School to the professors at Purdue University and Virginia Tech. My educational success would not have been the same without them.

I would like to thank my parents and step-parents for encouraging me in all of my endeavors. They have supported me emotionally and monetarily for too many years. I would also like to thank my entire family, who have motivated me to aspire to higher education. They have all known when to push, when to hold my hand, when to send a smile, and when to let go.

To all of my friends from my home in Cincinnati as well as my fellow Boilers and Hokies, and everywhere in between: from studying together to being there for a talk, or a song and a dance, you have all been there for me, and I would not be who I am without you.

I would like to express my deepest gratitude to my roommate, Rebecca Lattyak, who has been so easy-going and encouraging and let me bring a little bit of Purdue to Virginia Tech.

This research was funded by the Association of American Railroads, through the Transportation Technology Center, Inc.

Table of Contents

(Abstract) ii
Acknowledgements iii
Table of Contents iv
List of Figures vi
List of Tables x
Chapter 1 Introduction and Literature Review 1
1.1 Introduction 1
1.2 Literature Review 2
1.2.1 Lap Joints 2
1.2.2 Rail Foundation 2
1.2.3 Ties and Rail Foundation 3
1.2.4 Contact Stresses 3
1.2.5 Previous Research 4
1.3 Research Objectives 6
Chapter 2 Background 7
2.1 Lap Joints 7
2.1.1 Single Lap Joint 7
2.1.2 Finite Element Model of Single Lap Joint 9
2.1.3 Combined Shear and Bending in Joint 12
2.2 Beam on Elastic Foundation 15
2.2.1 Verification of Elastic Foundation in Finite Element Model 16
2.3 Hertz Contact Patch Theory 19
Chapter 3 Finite Element Model 21
3.1 Ties and Elastic Foundation 21
3.2 Mesh Convergence 23
3.3 Length Convergence 27
3.4 Implementation of Hertz Contact Theory 29
3.5 Parametric Studies 29
3.5.1 Tie Width 30
3.5.2 Location of Wheel Load 30
3.5.3 Joint Bar Length 31

3.5.4 Joint Bar Moment of Inertia 32
Chapter 4 Analysis and Results 33
4.1 Tie Width 34
4.1.1 Load at End Post 34
4.1.2 Load Between Ties 41
4.2 Joint Bar Length 44
4.2.1 Load at End Post 44
4.3 Joint Bar Moment of Inertia 47
4.3.1 Load at End Post 47
4.3.2 Load Between Ties 53
Chapter 5 Summary and Conclusions 57
5.1 Summary of Results 57
5.1.1 Tie Width 57
5.1.2 Joint Bar Length 58
5.1.3 Joint Bar Moment of Inertia 59
5.1.4 Wheel Load Location 62
5.2 Conclusions 62
5.3 Recommendations for Further Research 62
References 64
Appendix A 67
Appendix B 72
Vita 75

List of Figures

Figure 1.1: Cross-section and Plan View of (a) Standard and (b) Tapered Insulated Joints 5
Figure 1.2: Cross-section of Insulated Rail Joint 6
Figure 2.1: Single Lap Joint 7
Figure 2.2: Deformed Configuration of a Single Lap Joint 8
Figure 2.3: Shear Stress Profile Along Single Lap Joint 9
Figure 2.4: Finite Element Mesh of Single Lap Joint (a) Entire Lap Joint (b) Close Up of Overlap 10
Figure 2.5: Schematic of Single Lap Joint Finite Element Model 11
Figure 2.6: Shear Stress Along a Single Lap Joint 11
Figure 2.7: Simplified Insulated Railroad Joint; (a) Cross-section, (b) Isometric 12
Figure 2.8: Shear Stress Profile, τ_{xz}, of Simplified Joint Subjected to Tensile Load 13
Figure 2.9: Shear Stress Profile of Simplified Joint Subjected to Bending 14
Figure 2.10: Shear Stress Profiles, τ_{xz}, of Simplified Joint 15
Figure 2.11: Winkler's Beam on Elastic Foundation Model 16
Figure 2.12: Hetényi Test Rail Model 17
Figure 2.13: ABAQUS Test Rail Model 18
Figure 2.14: Beam on Full Elastic Foundation 19
Figure 3.1: Effective Length of Solid Element Ties; (a) 9-in.-Wide Tie, (b) 11-in.-Wide Tie 22
Figure 3.2: Top View of Elastic Foundation Contact Areas 23
Figure 3.3: One-fourth Rail Used in Mesh and Length Convergence Studies 24
Figure 3.4: Deflected Shapes of a Half Single Rail Supported by 9-in. Ties 25
Figure 3.5: Deflected Shapes of a Half Single Rail Supported by 11-in. Ties 26
Figure 3.6: Length Convergence of Rail Supported by 9-in. Ties 27
Figure 3.7: Length Convergence of Rail Supported by 11-in. Ties 28
Figure 3.8: Insulated Rail Joint with 36-in. Joint Bar, Load at End Post 30
Figure 3.9: Insulated Rail Joint with 36-in. Joint Bar, Load Between Ties 31
Figure 3.10: Insulated Rail Joint with 48-in. Joint Bars, Load at End Post 31
Figure 3.11: Joint Bars with Increasing Moments of Inertia 32
Figure 4.1: Epoxy Coordinate System 33
Figure 4.2: Epoxy Shown in Symmetric Loading 34
Figure 4.3: Displaced Shapes for Different Tie Widths 35
Figure 4.4: Deflected Tie Shape 36

Figure 4.5: Out-of-Plane Shear Stress, τ_{yz}, in Epoxy; 9-in. Ties; 36-in. Standard Joint Bars; Load at End Post 37
Figure 4.6: Out-of-Plane Shear Stress, τ_{yz}, in Epoxy; 11-in. Ties; 36-in. Standard Joint Bars; Load at End Post 37
Figure 4.7: Out-of-Plane Shear Stress, τ_{xy}, in Epoxy; 9-in. Ties; 36-in. Standard Joint Bars; Load at End Post 38
Figure 4.8: Out-of-Plane Shear Stress, τ_{xy}, in Epoxy; 11-in. Ties; 36-in. Standard Joint Bars; Load at End Post 38
Figure 4.9: Shear Stress Profiles of Epoxy Along Joint 39
Figure 4.10: Peel Stress in Epoxy; 9-in. Ties; 36-in. Standard Joint Bars; Load at End Post 40
Figure 4.11: Peel Stress in Epoxy; 11-in. Ties; 36-in. Standard Joint Bars; Load at End Post 40
Figure 4.12: Displaced Shapes for Different Tie Widths with Load at End Post and Load Between Ties 41
Figure 4.13: Out-of-Plane Shear Stress, τ_{yz}, in Epoxy; 9-in. Ties; 36-in. Standard Joint Bars; Load Between Ties 42
Figure 4.14: Out-of-Plane Shear Stress, τ_{yz}, in Epoxy; 11-in. Ties; 36-in. Standard Joint Bars; Load Between Ties 42
Figure 4.15: Out-of-Plane Shear Stress, τ_{xy}, in Epoxy; 9-in. Ties; 36-in. Standard Joint Bars; Load Between Ties 42
Figure 4.16: Out-of-Plane Shear Stress, τ_{xy}, in Epoxy; 11-in. Ties; 36-in. Standard Joint Bars; Load Between Ties 43
Figure 4.17: Peel Stress in Epoxy; 9-in. Ties; 36-in. Standard Joint Bars; Load Between Ties .. 44
Figure 4.18: Peel Stress in Epoxy; 11-in. Ties; 36-in. Standard Joint Bars; Load Between Ties 44
Figure 4.19: Displaced Shapes for Different Joint Bar Lengths 45
Figure 4.20: Out-of-Plane Shear Stress, τ_{yz}, in Epoxy; 9-in. Ties; 48-in. Standard Joint Bars; Load at End Post 46
Figure 4.21: Out-of-Plane Shear Stress, τ_{xy}, in Epoxy; 9-in. Ties; 48-in. Standard Joint Bars; Load at End Post 46
Figure 4.22: Peel Stress in Epoxy; 9-in. Ties; 48-in. Standard Joint Bars; Load at End Post 46
Figure 4.23: Displaced Shapes for Different Joint Bar Moments of Inertia 47
Figure 4.24: Bending Moment Distribution with Increasing Joint Bar Moments of Inertia 48
Figure 4.25: Out-of-Plane Shear Stress, τ_{yz}, in Epoxy; 9-in. Ties; 36-in. Joint Bars with 2*Std. Joint Bar Moment of Inertia; Load at End Post 49

Figure 4.26: Out-of-Plane Shear Stress, τ_{yz}, in Epoxy; 9-in. Ties; 36-in. Joint Bars with 3*Std. Joint Bar Moment of Inertia; Load at End Post 49
Figure 4.27: Out-of-Plane Shear Stress, τ_{xy}, in Epoxy; 9-in. Ties; 36-in. Joint Bars with 2*Std. Joint Bar Moment of Inertia; Load at End Post 50
Figure 4.28: Out-of-Plane Shear Stress, τ_{xy}, in Epoxy; 9-in. Ties; 36-in. Joint Bars with 3*Std. Joint Bar Moment of Inertia; Load at End Post 50
Figure 4.29: Peel Stress in Epoxy; 9-in. Ties; 36-in. Joint Bars with 2*Std. Joint Bar Moment of Inertia; Load at End Post 51
Figure 4.30: Peel Stress in Epoxy; 9-in. Ties; 36-in. Joint Bars with 3*Std. Joint Bar Moment of Inertia; Load at End Post 51
Figure 4.31: Elastic Peel Stresses in Double-Lap Joint 52
Figure 4.32: Displaced Shapes for Different Joint Bar Moments of Inertia; Load Between Ties 53
Figure 4.33: Out-of-Plane Shear Stress, τ_{yz}, in Epoxy; 9-in. Ties; 36-in. Joint Bars with 2*Std. Joint Bar Moment of Inertia; Load Between Ties 54
Figure 4.34: Out-of-Plane Shear Stress, τ_{yz}, in Epoxy; 9-in. Ties; 36-in. Joint Bars with 3*Std. Joint Bar Moment of Inertia; Load Between Ties 54
Figure 4.35: Out-of-Plane Shear Stress, τ_{xy}, in Epoxy; 9-in. Ties; 36-in. Joint Bars with 2*Std. Joint Bar Moment of Inertia; Load Between Ties 55
Figure 4.36: Out-of-Plane Shear Stress, τ_{xy}, in Epoxy; 9-in. Ties; 36-in. Joint Bars with 3*Std. Joint Bar Moment of Inertia; Load Between Ties 55
Figure 4.37: Peel Stress in Epoxy; 9-in. Ties; 36-in. Joint Bars with 2*Std. Joint Bar Moment of Inertia; Load Between Ties 56
Figure 4.38: Peel Stress in Epoxy; 9-in. Ties; 36-in. Joint Bars with 3*Std. Joint Bar Moment of Inertia; Load Between Ties 56
Figure 5.1: Comparing Maximum Stresses for Different Tie Widths; End Post Loading 57
Figure 5.2: Comparing Maximum Stresses for Different Tie Widths; Load Between Ties 58
Figure 5.3: Comparing Maximum Stresses for Different Joint Bar Lengths 58
Figure 5.4: Maximum Displacements for Increasing Joint Bar Moments of Inertia 59
Figure 5.5: Relative Displacement Longitudinally Along Rail 60
Figure 5.6: Comparing Maximum Stresses for Different Joint Bar Moments of Inertia; End Post Loading 61
Figure 5.7: Comparing Maximum Stresses for Different Joint Bar Moments of Inertia; Load Between Two Ties 61
Figure A.1: Isometric View of Rail Model Used in Mesh Convergence Study 67

Figure A.2: Mesh 1: (a) Entire Rail Model, (b) Close-Up Near Load Application Point 68
Figure A.3: Mesh 2: (a) Entire Rail Model, (b) Close-Up Near Load Application Point 69
Figure A.4: Mesh 3: (a) Entire Rail Model, (b) Close-Up Near Load Application Point 70
Figure A.5: Mesh 4: (a) Entire Rail Model, (b) Close-Up Near Load Application Point 71
Figure B.1: Isometric View of IJ Model Mesh..... 72
Figure B.2: IJ Model Mesh: (a) Half of Model, (b) Close-Up Near Load Application Point (End Post)..... 73
Figure B.3: Cross-section of IJ Model Mesh..... 74

List of Tables

Table 3.1: Characteristics of Meshes Considered in Convergence Study 25
Table A.1: Mesh 1 Details 68
Table A.2: Mesh 2 Details 69
Table A.3: Mesh 3 Details 70
Table A.4: Mesh 4 Details 71

CHAPTER 1 INTRODUCTION AND LITERATURE REVIEW

1.1 Introduction

Rail joints are used in the rail industry to connect two lengths of rail. Insulated railroad joints (IJs) serve another function as well: they prevent electrical current from flowing between the two rails. This electrical insulation discretizes sections of the track, which allows for detection of train locations and track break detection as well as the ability to isolate sections of track, such as those near a railroad crossing.

Insulated railroad joints are composed of the lengths of rail connected by two joint bars. Bolts, which are isolated from the joint bars and rails by thimbles, are used to mechanically fasten together the joint, while epoxy is used as the adhesive between the joint bars and rails. A layer of insulating fabric is included in the epoxy layer. An insulated filler, called the end post, is placed at the termination of the two lengths of rail at the joint. A joint can either be supported, when a tie is placed directly below the end post, or suspended.

The basic design of IJs has been in place for 135 years, and has changed very little over time. Due to increasing train axle loads on higher tonnage lines, failures of these IJs have begun to occur as little as 12-18 months after installation, which is approximately 10% of the lifetime of the adjoining rails. The costs, including parts, labor, and rail disruption, associated with replacing the failed joints can be quite significant. Improvement of the current IJ design is needed to address this growing problem (Dillard et al., 2006).

Many factors contribute to the failure of the insulated joint, such as insufficient quality control of the components of the joint, the dynamic loading generated by the rail discontinuity present at the joint, and the degradation of the foundation beneath the joint. The environment can also impact the bond, when adhesive cracking occurs and moisture is allowed to seep into the epoxy. The presence of water can cause debonding of the epoxy, resulting in the two lengths of rail, which are subjected to high longitudinal forces as well as bending moments from transverse wheel loading, pulling apart.

Debonding of the epoxy was actually determined to be the most common failure scenario in a sample of twenty IJs removed from the field. In this mechanical bond failure, the epoxy begins to "unzip" from the rail, causing the two lengths of rail to pull apart from one another (Davis et al., 2004).

This research focuses on a finite element analysis of standard IJs subjected to a static vertical wheel load and a tensile axial load. The commercial finite element analysis software ABAQUS (2004) is used to model possible configurations of the standard insulated rail joint. The stresses found in the epoxy layer of these various design options are examined to determine if these various design options could improve the performance of the insulated railroad joint.

1.2 Literature Review

1.2.1 Lap Joints

While the amount of research conducted on the finite element analysis of rail joints is limited, much work has been performed using finite element analysis to model lap joints. Bogdanovich and Kizzhakkethara (1999), Zgoul and Crocombe (2004), Campilho et al. (2005), and Yang et al. (2004) used the finite element program ABAQUS to model single and double lap joints, verifying the ability of two-dimensional and three-dimensional finite element models to predict stresses and joint strength of composite lap joints under tensile loads. In their experimental and numerical analyses of single lap joints, Matthews et al. (1995) demonstrated that high tensile peel stresses in the adhesive are centralized in a small region near the edge of the overlap. Hua et al. (2006) used ABAQUS to model the environmental degradation of ductile adhesive bond joints.

1.2.2 Rail Foundation

When the analysis of the deformation of rails under wheel loads was first developed, a rail supported by a continuous elastic foundation was used for calculations. With the steadily increasing wheel loads, the steadily decreasing cross tie spacings, and the increased rail cross-sections utilized by the rail industry today, this assumption is enhanced (Kerr, 2003). In his analysis of the rail as a beam on a continuous elastic foundation, Kerr (2003) used the governing differential equations and solutions proposed investigated by Winkler (1867) and further investigated by Hetényi (1946) (which are discussed in detail in Section 2.2) to determine the deflected shape and resulting bending moments of the rail due to the applied wheel loads.
The elastic foundation approach was confirmed by Kerr and Cox (1999), in their analysis of bonded insulated railroad joints, comparing their analytical results to experimental tests of actual bonded joints. One drawback, however, to using an elastic foundation to model ballast and ties supporting a rail is that the springs used to represent the foundation can be in both compression and tension. This means that not only do the elastic foundation springs apply an upward force to rail when it deflects downward, but conversely they can apply a downward force to the rail when the rail deflects upward.

1.2.3 Ties and Rail Foundation

Profillidis (2000) analyzed railroad ties to ascertain the effect of wheel loading on ties and subsequently on the supporting ballast and subgrade. In examining the spacing of ties, he determined that decreasing the tie spacing would better distribute the load on the foundation and result in smaller stresses in the foundation. He proposed that the optimum spacing of ties is approximately 19.6 in. to 23.6 in. His analysis also revealed that plastic deformations in ties are negligible and may be ignored, thus elastic behavior can be assumed in analyzing railroad ties.

Profillidis' analysis of multiple ties along the length of the rail showed that the effect of a wheel load when applied directly above a tie is negligible beyond the third successive tie on either side of the point of application of the load. This means that the effect of a wheel load is only felt by five ties centered about the wheel load.

In their examination of the pressure exerted by ties on the supporting ballast, Indraratna and Wadud (2005) determined that the contact pressure between the tie and the ballast may be assumed to be uniform. The effective length of the contact area between the tie and ballast, based on the work of Jeffs and Tew (1991), is one-third the total length of the tie under each rail. According to AREMA (2005), this effective length is also currently assumed in railroad design.

1.2.4 Contact Stresses

Hertz contact theory (Hertz, 1882), described in Section 2.3, has been used in stress analysis for bodies in contact, and is often applied to the contact between a wheel and rail. Burton (1975) supported the use of the Hertz contact patch in his review of the wheel-rail contact problem, stating that since the "wheels and rails are never perfectly rigid", the initial contact point between the two should spread into a finite area and "it is essential to have quantitative information on the size and shape of the contact patch, and on the distribution of the stresses in its immediate neighborhood."

The ability of the Hertz theory to correctly model the wheel-rail contact near a rail end, such as at an end post, was investigated by Chen (2003). His elastic-plastic model revealed that as the wheel load moves toward a rail end, larger plastic zones with increased von Mises stresses occur in the rail, which could cause deterioration of the rail end. In comparing his elastic-plastic model with Hertz contact theory, he learned that the contact length increases, thus decreasing the peak contact pressure, as the center of the wheel load moves closer to the rail end.

Another aspect of research on wheel-rail contact has focused on the dynamics of the problem. Wen et al. (2005) investigated the wheel-rail contact dynamically using finite element analysis. Their sensitivity studies into the effects of axle load and train speed on dynamic vertical forces,

stresses, and strain distributions in the railhead determined that the maximum vertical load due to the dynamic impact of the wheel was approximately 2.6 times the static force. Their work also concluded that increasing the axle load also increased the dynamic load and resulting stresses in the railhead, while increasing the train speed had very little effect on the load and stresses.

Chen and Kuang (2002) investigated the use of Hertz theory as it pertained to modeling the contact stress near insulated railroad joints. Their work focused on the contact pressure felt by the rail and insulated joint when subjected to a transverse wheel load, as well as the shear stress distributions in the rail. They demonstrated that traditional Hertzian contact theory may not be able to predict the wheel contact stress distributions around rail joints, depending on the material properties of the joint. They revealed that an IJ adhesive with a higher Young's modulus, such as epoxy-fiberglass with a Young's modulus of 6,500 ksi, may result in a more uniform pressure distribution than the two-dimensional parabolic distribution proposed by Hertz (1882). The epoxy used in this thesis has a significantly lower Young's modulus, 350 ksi. In their analyses involving epoxies with different material properties, Chen and Kuang also determined that an epoxy with a lower Young's modulus could result in higher maximum shear stresses in the entire insulated joint, especially when compared to a rail without the presence of an IJ. This increased shear stress was most noticeable at the contact point between the wheel and the top of the insulated joint, and its influence decreases along the depth of the joint. The location of this maximum shear stress, at the top of the joint bar, can also be seen in the work performed by Davis et al. (2004), which describes the mechanical failure of the bond as an "unzipping" of the epoxy initiated at the top of the end post.

Much of the research conducted on the wheel-rail contact problem and Hertz contact theory has focused on the contact between the wheel and the rail, rather than the resulting stresses in the rail and joint. However, the work of Chen and Kuang (2003) did show that variation of the maximum shear stress distribution decreased along the depth of the joint when a Hertz contact patch was used, and since the focus of this analysis is on the stresses found in the adhesive, which is a distance away from the top surface of the rail, the Hertzian contact patch has been used rather than using a single concentrated force to represent the vertical wheel load.

1.2.5 Previous Research

This research is part of a multi-tasked project intended to improve the current design of insulated railroad joints. This work uses finite element analysis to examine the stresses in the epoxy layer of the joint, which could result in a mechanical failure of the joint. Previous research also funded by the Transportation Technology Center, Inc. has been conducted by Professors R. H. Plaut and

D. A. Dillard, with undergraduate students Adric Eckstein, Seth Lambrecht, and Heike Lohse-Busch. Adric Eckstein performed a finite element analysis of both a suspended standard insulated joint, and a suspended tapered insulated joint, both of which are shown in Figure 1.1.

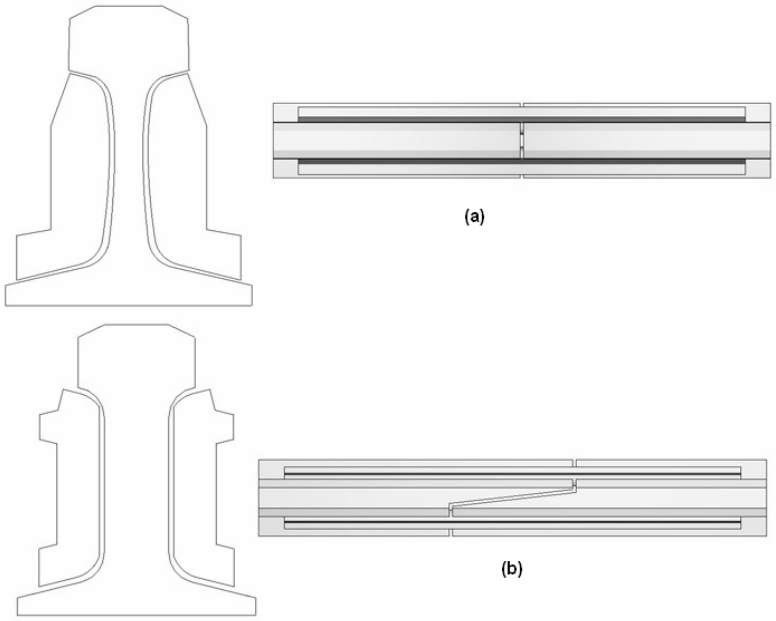

Figure 1.1: Cross-section and Plan View of (a) Standard and (b) Tapered Insulated Joints

He determined that the shear strain in the adhesive was small enough so that the resulting shear stresses transferred to the bolts were not significant enough to cause the bolts to contribute to the failure of the joint. His work concluded that the adhesive carried the majority of the axial and transverse loadings applied to the rail and joint, thus the bolts were not included in the remaining analyses. His work also showed that a tapered joint could reduce the shear stresses in the epoxy by two-thirds when compared with the standard IJ (Eckstein et al., 2005). Seth Lambrecht continued the investigation into tapered joints, varying the taper angle. His work determined that the best design of a tapered joint would have a length of at least 8 in., with an optimal length of 27 in. and an angle of 2.39 degrees. This design would yield lower stresses in the epoxy layer. Heike Lohse-Busch performed numerical analyses of adhesively bonded joints using Winkler springs and the Rayleigh-Ritz method to calculate vertical deflections and bending moment distributions of both standard and tapered joints. Her results confirmed the findings of the finite element analyses by both Adric Eckstein and Seth Lambrecht (Lambrecht and Lohse-Busch, 2006).

1.3 Research Objectives

The objective of this thesis is to use finite element analysis to investigate possible improvements to the design of insulated railroad joints. First the finite element analysis program ABAQUS is tested to verify its ability to correctly model the interaction of the rail and epoxy. These results are compared to the shear lag model of single lap joints proposed by Volkersen (1938). The use of the elastic foundation interaction in the ABAQUS model is also examined, and the resulting displacement curves are compared to the beam on elastic foundation equations proposed by Winkler (1867) and further investigated by Hetényi (1946). Convergence studies of mesh size and rail length are conducted in order to refine the finite element model to be used in ABAQUS.

In this thesis, a supported standard insulated rail joint is modeled with solid finite elements. Figure 1.2 shows the cross-section of the standard joint to be modeled.

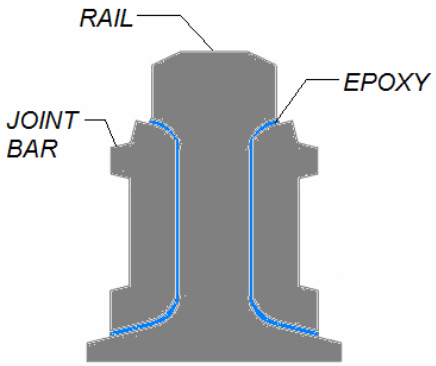

Figure 1.2: Cross-section of Insulated Rail Joint

Parametric studies of the widths and joint bar dimensions are conducted. The resulting displaced shapes of the joints as well as shear and peel stresses found in the epoxy layer are compared for the various designs. These will help to determine what design modifications can be made in order to improve the insulated rail joint and increase its life expectancy.

CHAPTER 2 BACKGROUND

2.1 Lap Joints

Analyzing an insulated railroad joint can be a very complex problem. Tensile stresses in the rail result in shear stress in the epoxy layer, while bending of the rail and joint can produce additional stresses in the adhesive.

2.1.1 Single Lap Joint

To begin to understand the shear stress component in the adhesive between the joint bars and the rail of the insulated railroad joint, a simpler model of a single lap joint was analyzed first. In a single lap joint, two bars (adherends) are overlapped, joined together with an adhesive, and then subjected to a tensile load, as shown in Figure 2.1.

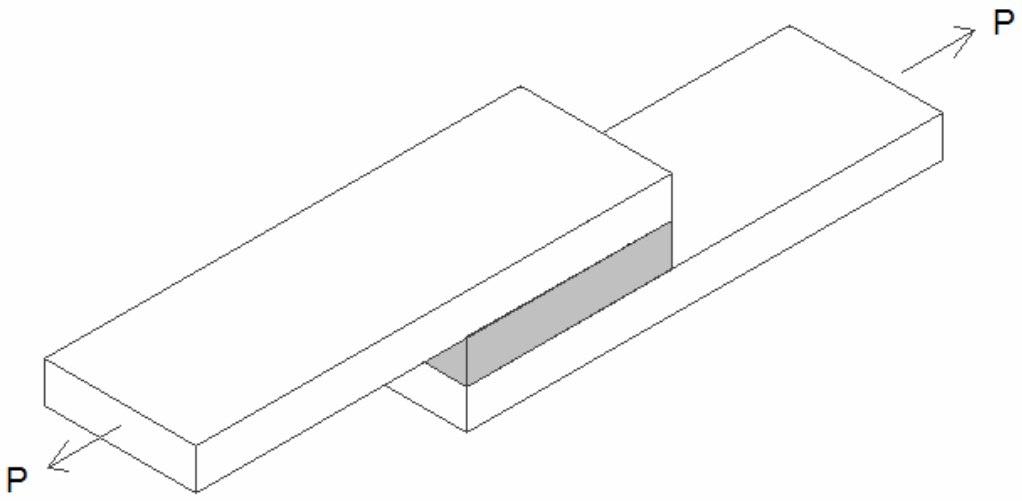

Figure 2.1: Single Lap Joint

When the two adherends are considered to be deformable, not rigid, the phenomenon of differential shear, or shear lag, occurs in the adhesive of the joint. This occurrence of shear lag, investigated first by Volkersen (1938), causes the adhesive to deform as shown below.

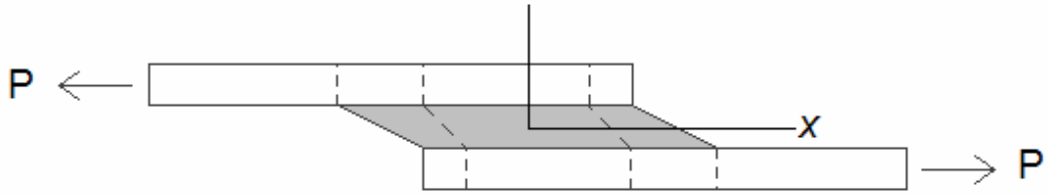

Figure 2.2: Deformed Configuration of a Single Lap Joint

Due to this shear lag, the tensile strain in the adherends is at a maximum at one end of the overlap and zero at the other. According to Adams et al. (1997), "Thus, assuming continuity of the adhesive/adherend interface, the uniformly sheared parallelograms of adhesive . . . become distorted to shapes given" above, in Figure 2.2. Through Volkersen's analysis of the differential shear, the following relationship between the shear stress in the adhesive and the longitudinal distance along the overlap was determined:

$$\tau(x) = \frac{P}{bl}\left[\frac{\omega}{2}\frac{\cosh(\omega X)}{\sinh(\omega/2)} + \left(\frac{\psi - 1}{\psi + 1}\right)\frac{\omega}{2}\frac{\sinh(\omega X)}{\cosh(\omega/2)}\right] \qquad (2.1)$$

where

$$\omega^2 = (1+\psi)\phi \qquad (2.2)$$

$$\psi = t_1 / t_2 \qquad (2.3)$$

$$\phi = \frac{Gl^2}{Et_1t_3} \qquad (2.4)$$

$$X = x/l \qquad (2.5)$$

In this analysis, P is the tensile load applied to the joint; b is the width of the joint; l is the length of the joint; t_1, t_2, t_3 are the thicknesses of the upper adherend, lower adherend, and adhesive, respectively; G is the shear modulus of the adhesive; and E is the modulus of elasticity of the adherends. The longitudinal distance along the overlap is defined by the variable x, where $x = 0$ at the center of the joint.

Shear lag produces a shear stress profile as shown in Figure 2.3 below.

Figure 2.3: Shear Stress Profile Along Single Lap Joint

Notice that the shear stress is a maximum along the edges of the adherends and a minimum at the center of the overlap, according to Volkersen's analysis. However, this is a result of the material solution proposed by Volkersen. In an elasticity solution, the shear stresses at the edges of the adherend, where $x = \pm l / 2$, are zero, since the air at the edge of the overlap cannot apply a shear stress to the adhesive.

2.1.2 Finite Element Model of Single Lap Joint

A finite element model of a single lap joint was built using ABAQUS (2006) to verify the ability of solid elements to accurately model shear deformations and stresses in the adhesive layer. This model consisted of two steel bars, whose physical properties were the same as rail steel, and epoxy, again with the same properties as the epoxy to be used in the insulated rail joint. The bars had dimensions of 25 in. width, 1.6 in. depth, and 100 in. length. The epoxy had a thickness of 0.01 in. The length of the overlap was 12.5 in. The model consisted of 736,674 linear tetrahedral elements. Shown in Figures 2.4 (a) and (b) is the finite element mesh of the entire single lap joint model as well as a close-up of the overlap of the two adherends, respectively.

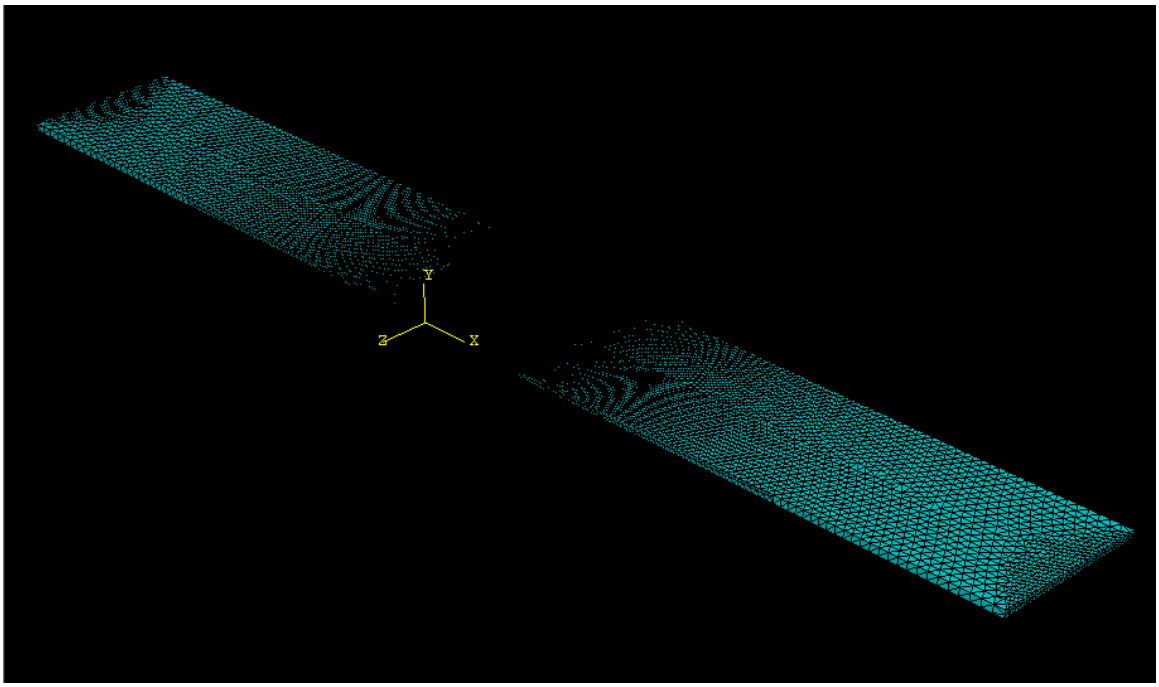

(a)

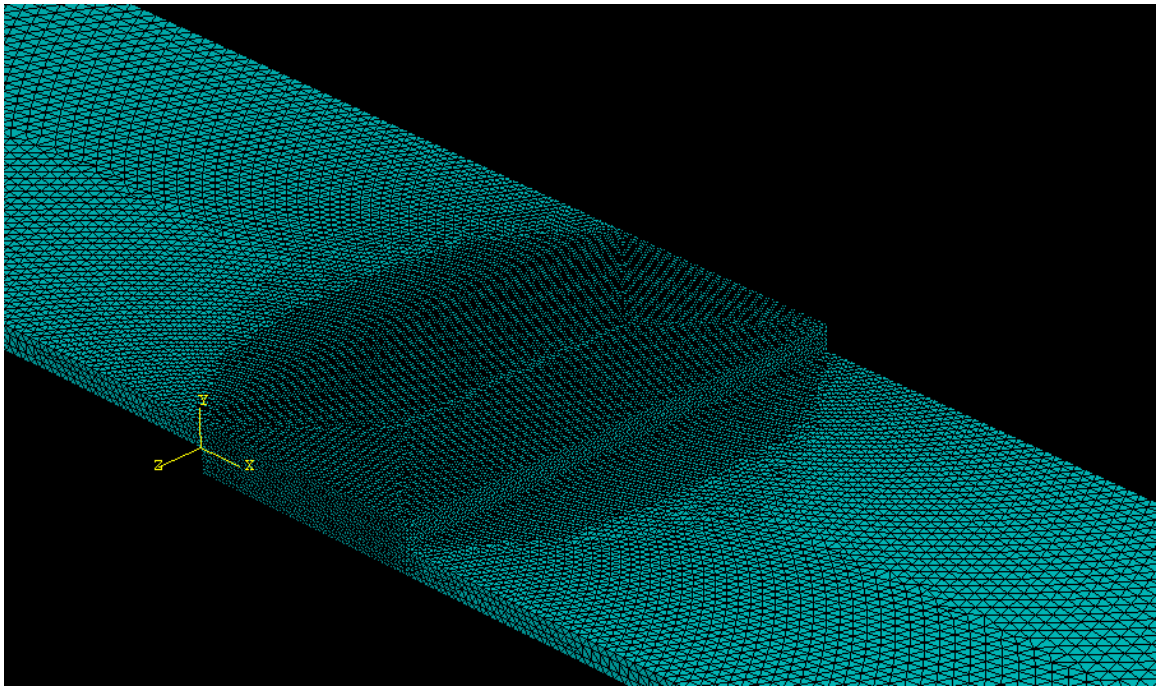

(b)

Figure 2.4: Finite Element Mesh of Single Lap Joint (a) Entire Lap Joint (b) Close Up of Overlap

A side view schematic of this model is shown in Figure 2.5, to illustrate the boundary load conditions applied to the single lap joint.

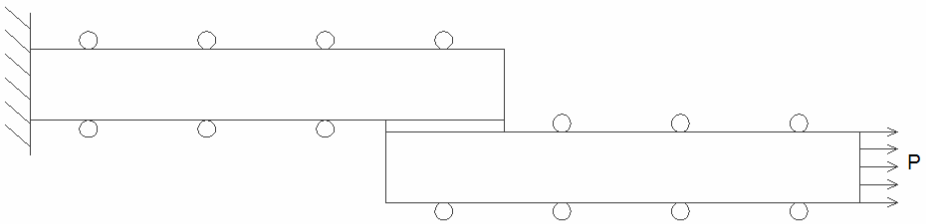

Figure 2.5: Schematic of Single Lap Joint Finite Element Model

In the finite element model, the upper adherend was fixed at the end away from the joint, while the lower adherend was free. Both adherends were constrained in the vertical direction. The tensile load, P, was applied as a pressure over the free end of the lower adherend.

The shear stress results of this model were then compared to those of the numerical model with similar dimensions, predicted by Volkersen's equations, as shown in Figure 2.6.

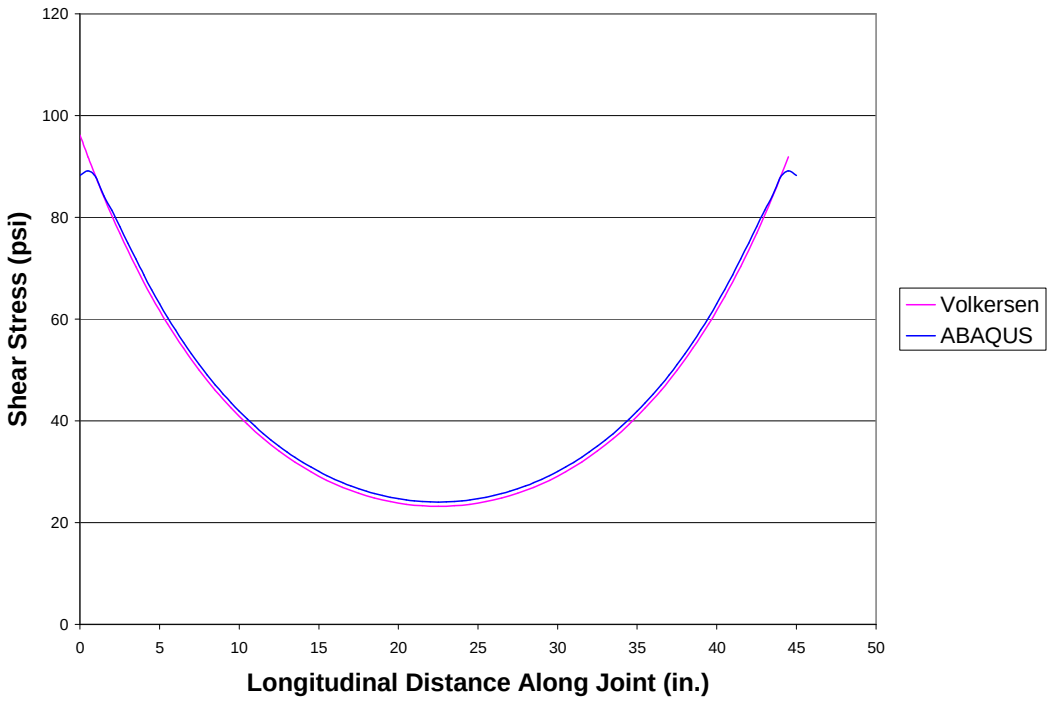

Figure 2.6: Shear Stress Along a Single Lap Joint

As can be seen in Figure 2.6, the finite element model followed Volkersen's model, thus confirming the use of solid elements to accurately model the stresses in the adhesive.

2.1.3 Combined Shear and Bending in Joint

Because the insulated railroad joint is subjected to both shear and bending loadings, a finite element model of a simplified joint was built to investigate the interaction of these two stresses on the epoxy adhesive. This model consisted of 89,216 linear hexahedral elements.

A cross-section and isometric schematic of this simplified joint are shown below in Figures 2.7 (a) and (b), respectively. To save on computing cost, symmetry was used and only half of the simplified joint was analyzed. The plane of symmetry, meaning that the translation in the x direction as well as the rotation about the y and z axes are zero, is shown below in Figure 7b. Also shown are the points *C* and *B*, which correspond to the center of the joint bar and edge of the joint bar, respectively. These will be used later.

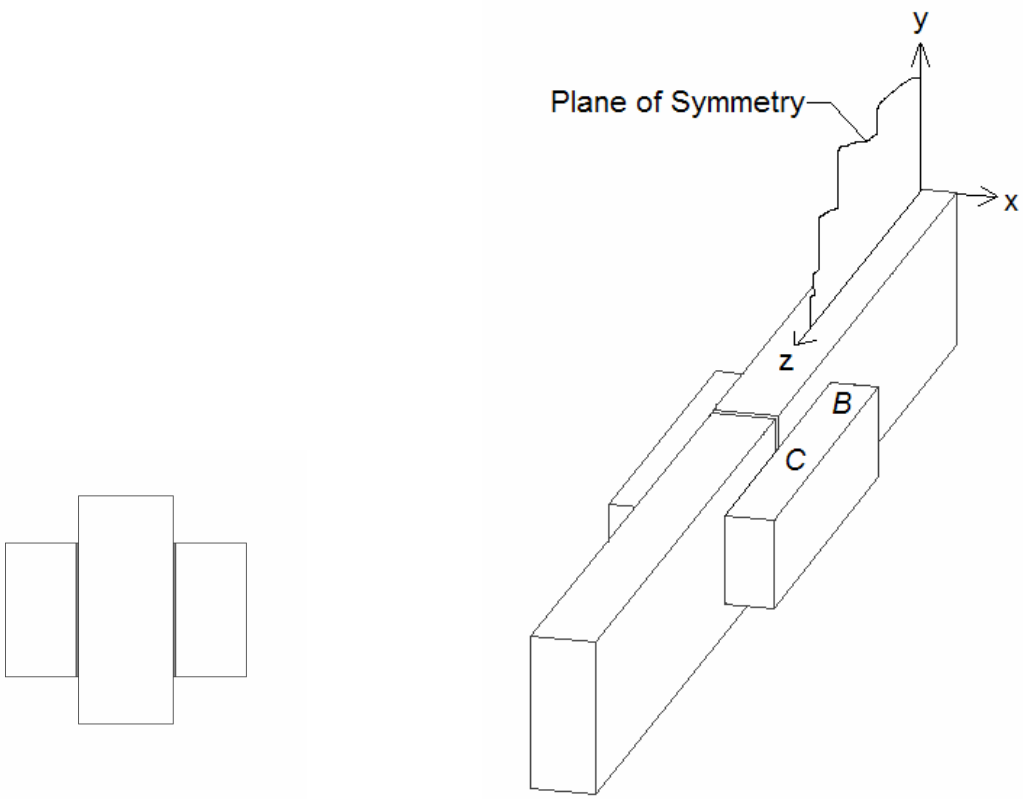

(a) (b)

Figure 2.7: Simplified Insulated Railroad Joint; (a) Cross-section, (b) Isometric

First a model was analyzed in which the only load applied to the model was tension in the "rail".

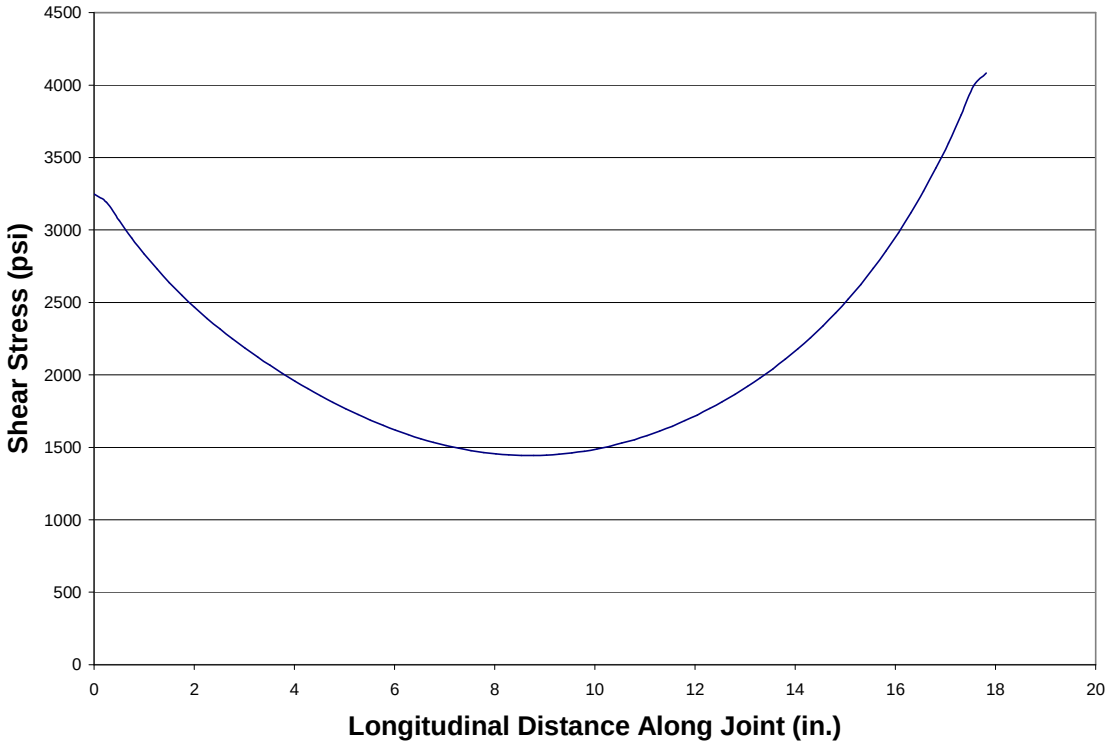

Figure 2.8: Shear Stress Profile, τ_{xz}, of Simplified Joint Subjected to Tensile Load

In Figure 2.8, a longitudinal distance of zero corresponds to the edge of the epoxy closer to the middle of the joint (Point C in Figure 2.7(b)), whereas a longitudinal distance of approximately 18 in. corresponds to the edge of the epoxy farther away from the center of the joint (Point B in Figure 2.7(b)). The resulting shear stress profile of τ_{xz} is not symmetric about the center of the joint. The shear stress is greater at the edge of the joint corresponding to Point B, the joint bar, which is the thicker of the two adherends. The shear stress is less at the edge corresponding to Point C, the rail, which is the thinner adherend. This is because the applied load is attracted to the thicker member in order to maintain strain compatibility across the two adherends.

After analyzing the simplified joint with only the tensile load applied, another loading was analyzed using the same finite element model, in which only the transverse wheel load was applied to the center of the joint. The shear stress profile in the adhesive layer is shown below in Figure 2.9.

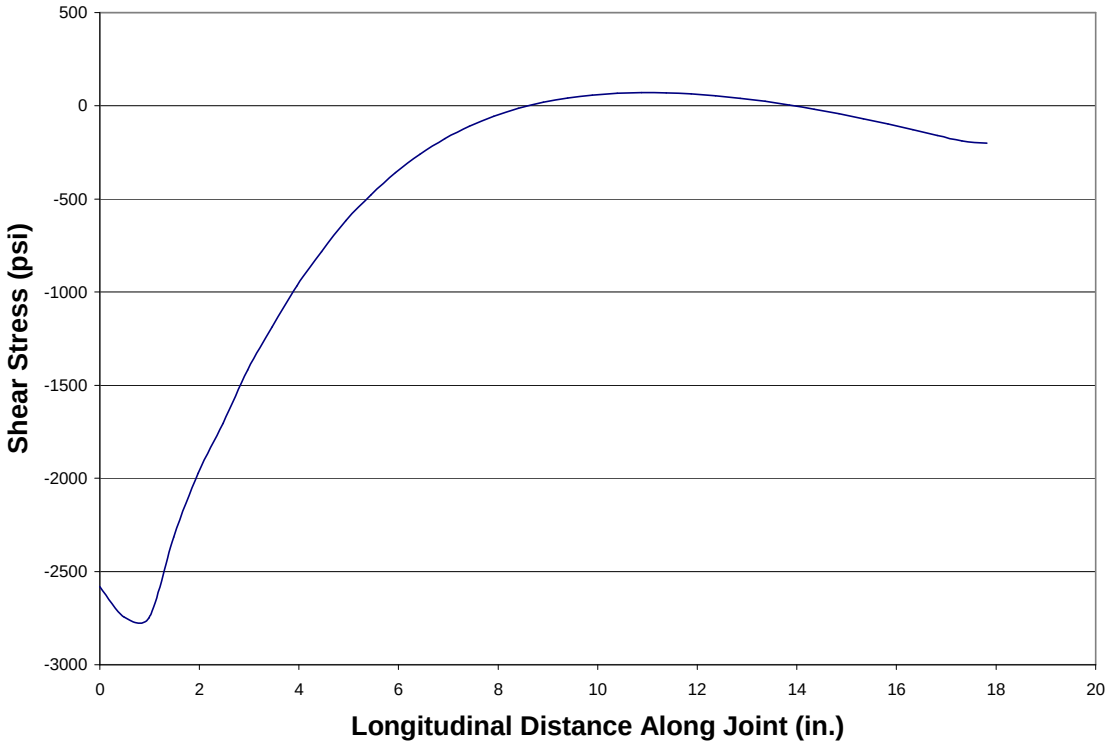

Figure 2.9: Shear Stress Profile of Simplified Joint Subjected to Bending

When the simplified joint is only subjected to bending, the shear stress magnitude in the epoxy is greatest near the longitudinal distance of 0 in. This point corresponds to Point C in Figure 2.7(b), the center of the joint bar.

Finally, the simplified joint was subjected to both tensile and transverse loading. The resulting shear stresses are shown in Figure 2.10.

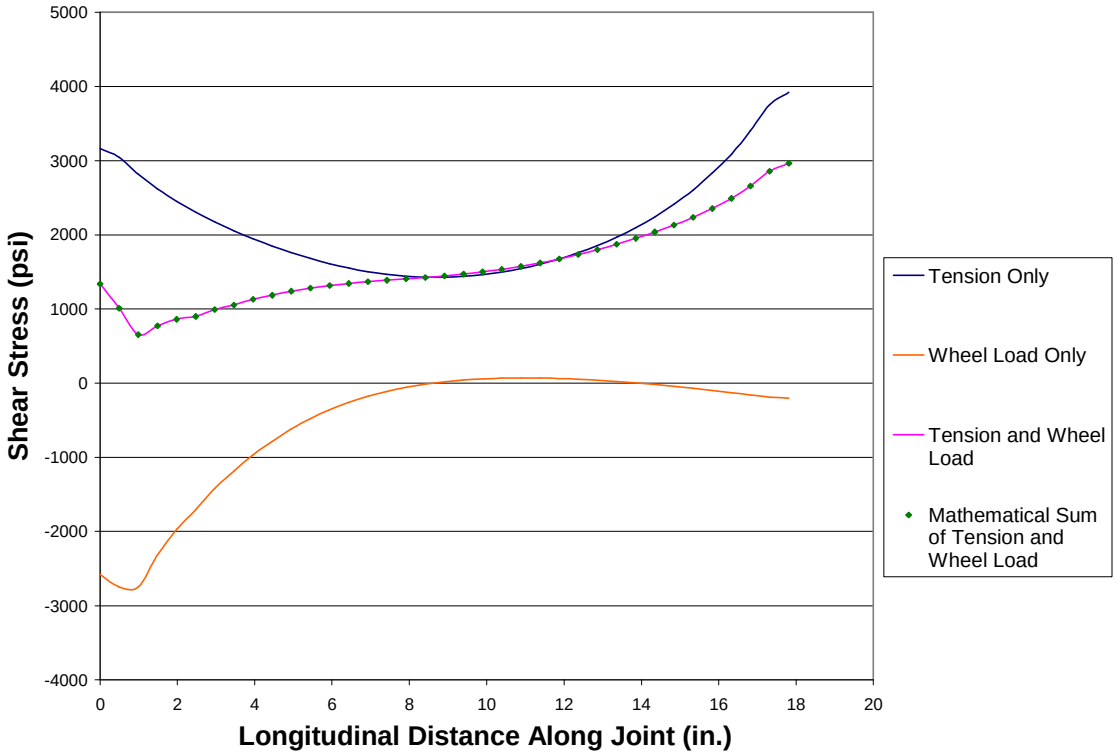

Figure 2.10: Shear Stress Profiles, τ_{xz}, of Simplified Joint

It is interesting to notice that the shear stress of the combined tensile and transverse wheel load is the sum of the shear stresses caused by tension and wheel load separately.

2.2 Beam on Elastic Foundation

For analytical purposes, a beam supported by a soil foundation is often modeled using Winkler's beam on elastic foundation theory, where the soil is represented by a continuous distribution of springs along the length of the beam, as shown in Figure 2.11.

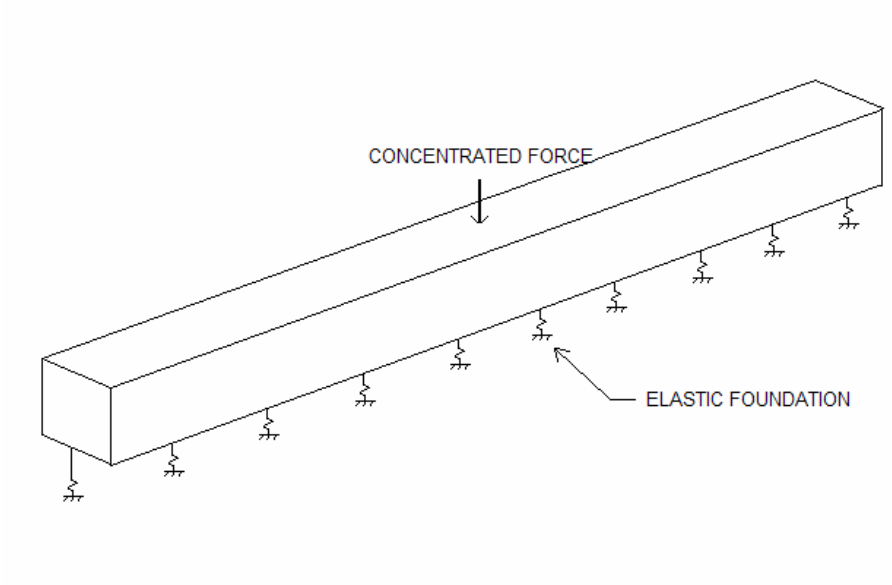

Figure 2.11: Winkler's Beam on Elastic Foundation Model

According to Winkler (1867), and further investigated by Hetényi (1946), the equation representing the deflection curve of a beam in bending supported by an elastic foundation and subjected to a transverse loading is a fourth order differential equation, with a general solution of

$$y(x) = e^{\lambda x}(C_1 \cos \lambda x + C_2 \sin \lambda x) + e^{-\lambda x}(C_3 \cos \lambda x + C_4 \sin \lambda x) \qquad (2.6)$$

where

$$\lambda = \left(\frac{k}{4EI} \right)^{1/4} \qquad (2.7)$$

(Hetényi, 1946)

2.2.1 Verification of Elastic Foundation in Finite Element Model

In order to implement elastic foundation theory in ABAQUS, the Elastic Foundation Interaction was used to represent the ties and ballast supporting the rail. Interactions in ABAQUS are used to model such objects as connections between two points on a model as well as mechanical interactions between the model and its surroundings (ABAQUS, 2004). To verify the use of this interaction, a finite element test rail model was built in ABAQUS and then compared to a numerical model developed by Hetényi, which is based on Winkler's elastic foundation theory.

The "beam" used in both models was a 600-in.-long 136 RE Rail with a moment of inertia of 99.4 $in.^4$ In both the ABAQUS and Hetényi models, the value of the modulus of elasticity, E, was

30 x 10^6 lb/in.^{2}, and the concentrated load placed at the center of the rail was a wheel load of 32,500 lb.

This rail was placed upon an elastic foundation with a stiffness of 3,000 lb/in./in., a value representing a wood-tie track already compacted by traffic (Kerr, 2003).

2.2.1.1 Hetényi's Model

The Hetényi numerical model used for verification was a beam of infinite length placed upon an elastic foundation composed of springs with stiffness, *k*, which has units of force/deflection/length. Due to the long length of the beam in the finite element model, the equations for the infinite beam in Hetényi's model can be used for comparison. In this model, a concentrated force was applied at the center of the beam. The model is shown below, in Figure 2.12.

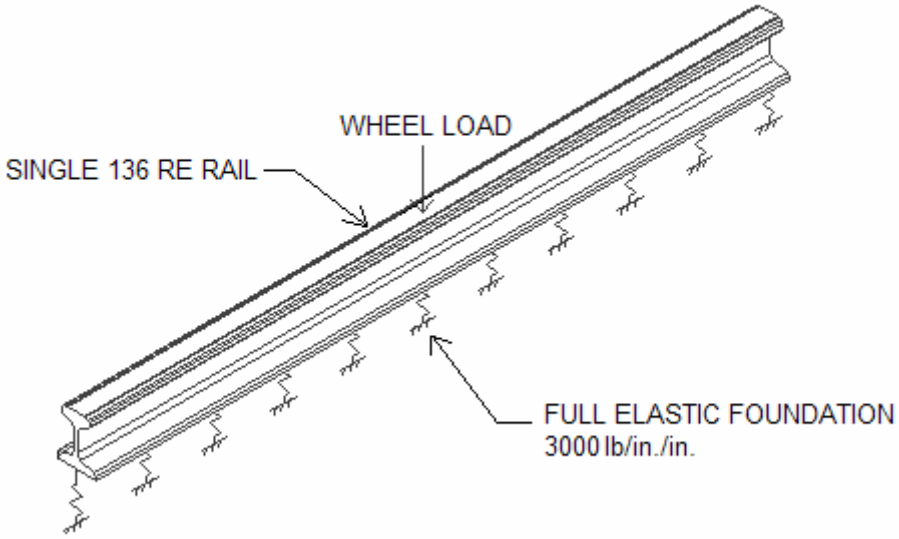

Figure 2.12: Hetényi Test Rail Model

The deflection of the beam along the length is defined by the following equation, for $x \geq 0$:

$$y(x) = \frac{P\lambda}{2k} e^{-\lambda x} (\cos \lambda x + \sin \lambda x) \qquad (2.8)$$

The value λ is defined in Equation 2.7. This deflection curve is only valid for values of x greater than zero, those being to the right of the application point of the concentrated force, P (Hetényi, 1946). The deflection for $x < 0$ is obtained by replacing x by $-x$ in Equation 2.8.

2.2.1.2 ABAQUS Model

For comparison with the numerical model of Hetényi, a finite element model with a very fine mesh was built in ABAQUS. This was then compared to a similar numerical model using Hetényi's equation. The Elastic Foundation Interaction used in ABAQUS requires selecting a face or area upon which the foundation will act, and specifying a stiffness. Since this elastic foundation acts over an area, the units of stiffness are force/deflection/area. Thus the value of stiffness used in the Hetényi model is divided by the width of the beam. The stiffness value of 3,000 lb/in./in. was divided by the width of the rail section, 6 in., to become a value of 500 lb/in./in.^{2}. The ABAQUS model is shown as a schematic in Figure 2.13.

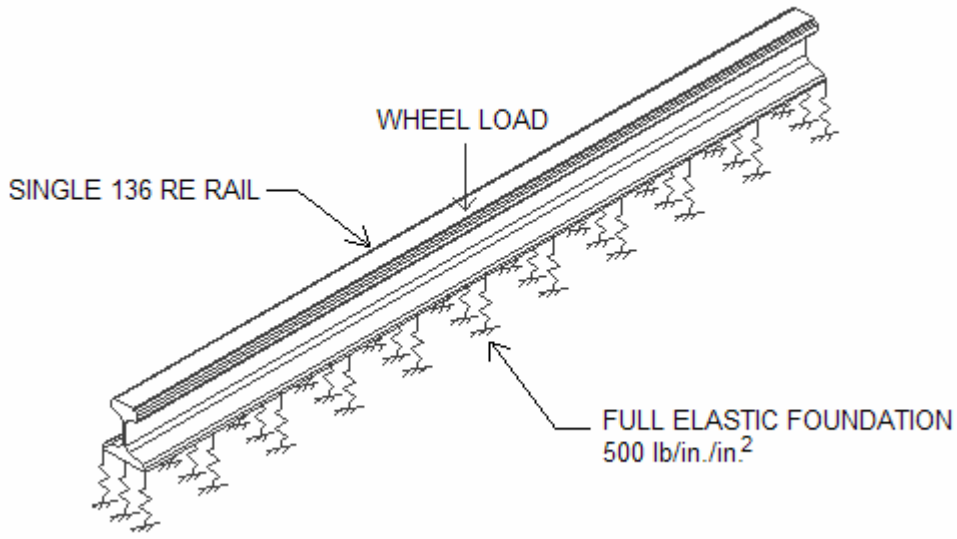

Figure 2.13: ABAQUS Test Rail Model

2.2.1.3 Comparing the Hetényi and ABAQUS Models

A comparison of the deflections found using ABAQUS and the equations developed by Hetényi is shown in Figure 2.14.

As shown, the deflected shape of the rail found using the elastic foundation interaction in ABAQUS is very much in agreement with the deflected shape found using the Hetényi beam on elastic foundation model, thus verifying the use of this ABAQUS tool as well as the value of the stiffness used.

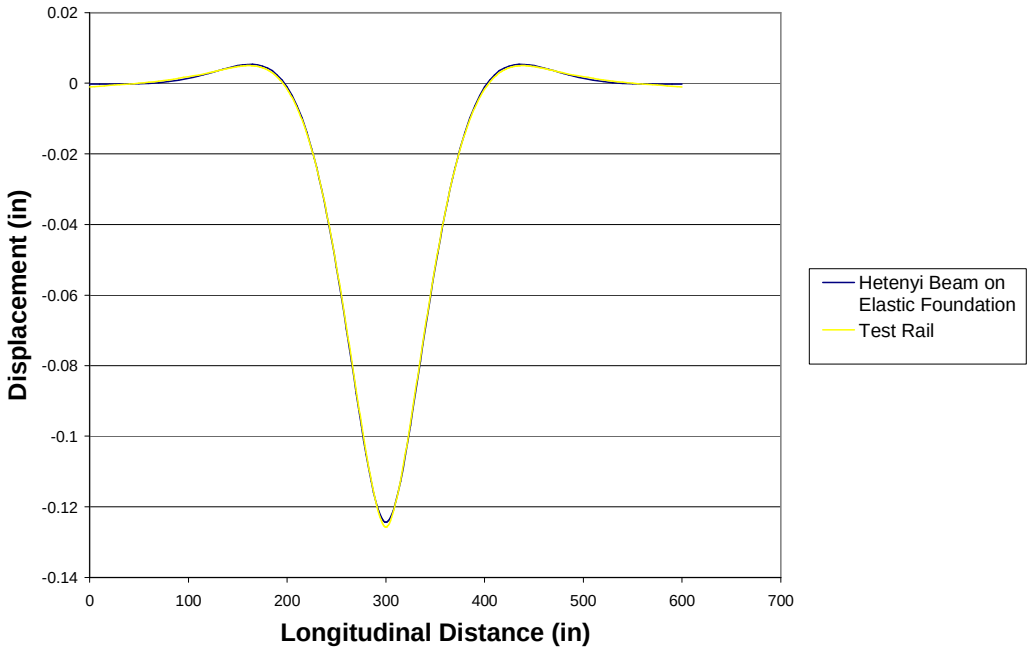

Figure 2.14: Beam on Full Elastic Foundation

2.3 Hertz Contact Patch Theory

According to Hertzian contact theory, the contact surface between two curved surfaces, such as a wheel and a rail, can be represented as an ellipse with a major semi-axis *a* and a minor semi-axis *b*. The pressure exerted over this elliptical area is parabolic in two directions and is defined according to the following equation:

$$p = p_0 \sqrt{1 - \left(\frac{x}{a}\right)^2 - \left(\frac{y}{b}\right)^2} \qquad (2.9)$$

where p_0 is the maximum contact pressure at the initial central contact point, and the coordinates *x* and *y* refer to distances from the initial contact point along the major semi-axis and minor semi-axis, respectively. The value of p_0 is given by

$$p_0 = \frac{3}{2}\left(\frac{W}{\pi ab}\right) \qquad (2.10)$$

where W is the applied normal force.

The magnitudes of a and b also depend on the applied normal force, as well as the profile and materials of the wheel and rail. They are expressed as

$$a = m\left[\frac{3\pi W\left(K_1 + K_2\right)}{4K_3}\right]^{1/3} \tag{2.11}$$

$$b = n\left[\frac{3\pi W\left(K_1 + K_2\right)}{4K_3}\right]^{1/3} \tag{2.12}$$

where

$$K_1 = \frac{1-\nu_w^2}{\pi E_w} \tag{2.13}$$

$$K_2 = \frac{1-\nu_R^2}{\pi E_R} \tag{2.14}$$

$$K_3 = \frac{1}{2}\left(\frac{1}{R_1} + \frac{1}{R_1'} + \frac{1}{R_2} + \frac{1}{R_2'}\right) \tag{2.15}$$

Here E_w, E_r, ν_w, and ν_r are the modulus of elasticity and Poisson's ratios of wheel and rail, respectively. R_1 and R_2 are defined as the principal rolling radii of the wheel and rail, respectively. R_1' and R_2' are the transverse radii of curvature of the wheel and rail, respectively.

The coefficients m and n in Equations 2.11 and 2.12 are functions of θ and can be found in a table in Dukkipati (2000). The variable θ is defined as

$$\theta = \cos^{-1}\left(\frac{K_4}{K_3}\right) \tag{2.16}$$

where

$$K_4 = \frac{1}{2}\left[\left(\frac{1}{R_1} + \frac{1}{R_1'}\right)^2 + \left(\frac{1}{R_2} + \frac{1}{R_2'}\right)^2 + 2\left(\frac{1}{R_1} - \frac{1}{R_1'}\right)\left(\frac{1}{R_2} - \frac{1}{R_2'}\right)\cos 2\varphi\right] \tag{2.17}$$

and φ is the angle between the normal planes that contain the curvatures $1/R_1$ and $1/R_2$. (Chen and Kuang, 2002).

CHAPTER 3 FINITE ELEMENT MODEL

For all of the finite element models built using ABAQUS to represent the insulated railroad joint, a single 136 RE rail with standard joint bar was used. The 136 RE rail has a moment of inertia of 99.4 in.^{4}, and two standard joint bars have a combined moment of inertia of 24.9 in.^{4}. Both the rail and joint bars are made of rail steel, which has a Young's modulus of 30,000,000 lb/in.^{2} and a Poisson's ratio of 0.287. The epoxy used to bond the joint bars to the rail has a Young's modulus of 350,000 lb/in.^{2} and a Poisson's ratio of 0.34. The rail was subjected to an axial tension of 300,000 lb as well as a transverse, vertical wheel load of 32,500 lb. Solid linear tetrahedral elements (designated C3D4) were used in the mesh in order to accurately represent the curved surfaces of the rail and joint bars. The material properties are all consistent with earlier work done on this project.

Described below is the approach to modeling the ties and ballast, as well as the results of investigations into simple models, varying the mesh and lengths of rail. The results will then be applied to models of the insulated joints

3.1 Ties and Elastic Foundation

In the finite element models of the insulated railroad joints developed in this research, a tie was to be placed directly beneath the end post. Since this would have a direct effect on the displacement at this location, it was decided to model several ties as solid elements in lieu of simply representing them as an elastic foundation.

Five ties were modeled as solid elements, with an effective length along the tie (perpendicular to the rail) of one-third the original tie length (Profillidis, 2000; AREMA, 2005). The rest of the ties, further along the length of the rail from the joint, were represented as an elastic foundation.

The dimensions of the ties used in the models were 9 in. x 7 in. x 102 in. and 11 in. x 7 in. x 120 in. Thus the effective length of a 9-in.-wide tie was 34 in. while the effective length of an 11-in.-wide tie was 40 in. The effective length is placed symmetrically underneath the rail, as shown below in Figures 3.1(a) and (b).

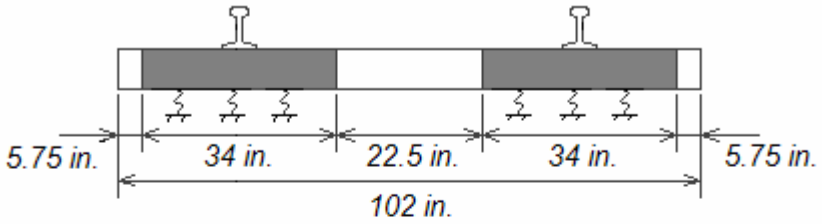

(a)

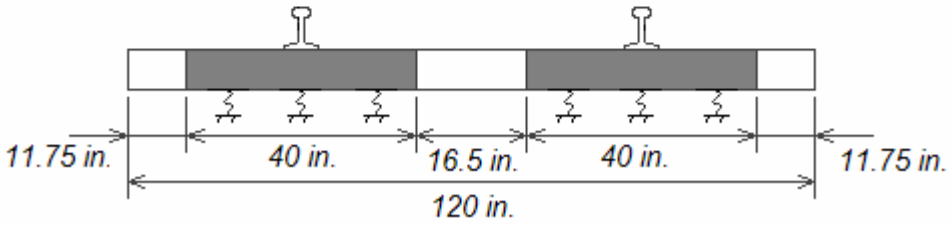

(b)

Figure 3.1: Effective Length of Solid Element Ties; (a) 9-in.-Wide Tie, (b) 11-in.-Wide Tie

The wood used in the model was considered to be oak. Due to the small deformations in the wooden ties, the wood was considered to be isotropic with an elastic modulus of 1,500,000 lb/in.^{2} and a Poisson's ratio of 0.3 (Profillidis, 2000).

In order to calculate the appropriate elastic foundation stiffness for the ties and ballast, the following equation was used:

$$K = \frac{\left(3{,}000\ lb/in.^2\right) * \left(Center\ to\ Center\ Tie\ Spacing\right)}{Area\ of\ Tie} \qquad (3.1)$$

As mentioned before, the value of 3,000 lb/in.^{2} is a value representing a wood-tie track, already compacted by traffic (Kerr, 2003). The center-to-center tie spacing used for both tie widths was 19.5 in. The area of one-third length of a 9-in.-wide tie was used in the above equation. The resulting stiffness, calculated below, was used to represent the ballast beneath the solid element ties of both 9-in. and 11-in. widths:

$$K = \frac{\left(3{,}000\ lb/in.^2\right) * \left(19.5\ in.\right)}{\left(9\ in.\right) * \left(\frac{100\ in.}{3}\right)} = 191\ lb/in.^3 \qquad (3.2)$$

To represent the remaining ties, the area used in the above equation was chosen as the contact area between the ties and the rail: the width of the tie multiplied by the width of the rail. The contact areas for both the solid element ties as well as examples of contact areas along the rail for the remaining ties are shown in Figure 3.2, highlighted in gray.

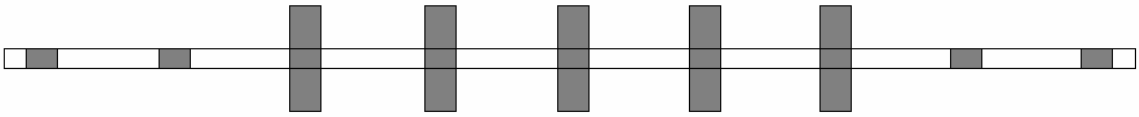

Figure 3.2: Top View of Elastic Foundation Contact Areas

The values of stiffness used for the 9-in. and 11-in. ties are shown below:

$$K = \frac{(3{,}000\ lb/in.^2) * (19.5\ in.)}{(9\ in.) * (6\ in.)} = 1{,}083.33\ lb/in.^3 \tag{3.3}$$

$$K = \frac{(3{,}000\ lb/in.^2) * (19.5\ in.)}{(11\ in.) * (6\ in.)} = 886.36\ lb/in.^3 \tag{3.4}$$

3.2 Mesh Convergence

In order to build an accurate finite element model in ABAQUS that was the most cost effective in terms of computer space and time, a mesh convergence study was conducted. In this study, a single rail on ties, utilizing the elastic foundation interaction, with a concentrated force representing the wheel load was built as a finite element model.

To simplify the model and decrease the computer time, only one-fourth of a single 136 RE rail was built in ABAQUS, as shown in Figure 3.3.

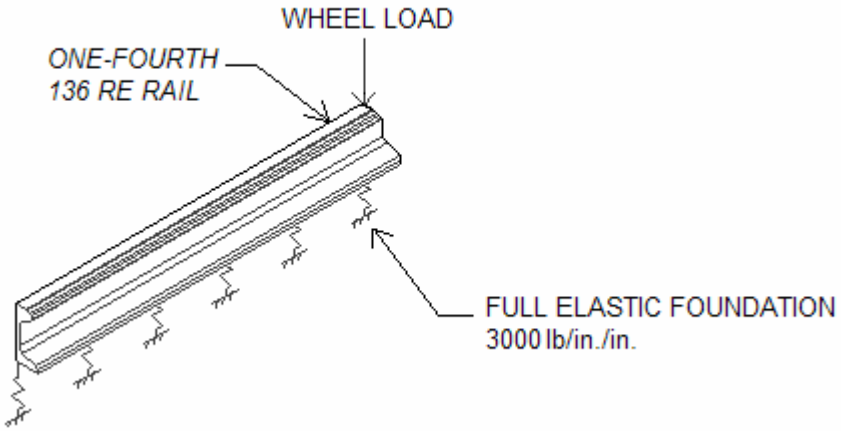

Figure 3.3: One-fourth Rail Used in Mesh and Length Convergence Studies

Again, symmetry about the longitudinal center line of the rail was used. At the end of the rail corresponding to the load application point, symmetry was applied, causing the deflection in the longitudinal direction and the rotation about the other two axes to remain zero. The other end of the rail was left free. A half length of 300 in. from the wheel load to the free end was used in the longitudinal direction.

Different meshes were used, varying the size and number of elements. This convergence study was performed for a rail both on 9 in. and 11 in. ties. The center-to-center spacing of the ties was kept at a distance of 19.5 in. for both tie sizes. Thirteen different meshes were used in this study, and it was discovered that the deflected shape of the rail model followed four different contours. Thus, only four representative meshes were selected for further discussion. The meshes were numbered with increasing refinement, so that Mesh 1 was the coarsest mesh and Mesh 4 was the finest mesh. The characteristics of the four meshes for each tie size are shown in Table 1. A more detailed description of the four meshes can be found in Appendix A.

	9 in. Ties				11 in. ties			
	Mesh 1	Mesh 2	Mesh 3	Mesh 4	Mesh 1	Mesh 2	Mesh 3	Mesh 4
Number of Elements	7,365	14,946	29,017	41,747	6,950	14,932	28,387	41,008
Run Time (s)	4	11	28	56	4	6	12	22
% Difference from Mesh 4	9.00%	1.70%	0.01%	-	20.80%	1.79%	0.01%	-

Table 3.1: Characteristics of Meshes Considered in Convergence Study

As can be seen, as the refinement of the mesh increases, so does the number of elements as well as the run time. The third row compares the vertical displacement of the bottom of the rail at the point of application of the wheel load of the different meshes with that of Mesh 4, the mesh with the most refinement. Shown below, in Figures 3.4 and 3.5, are graphical representations of the deflected shapes measured along the bottom of the rail.

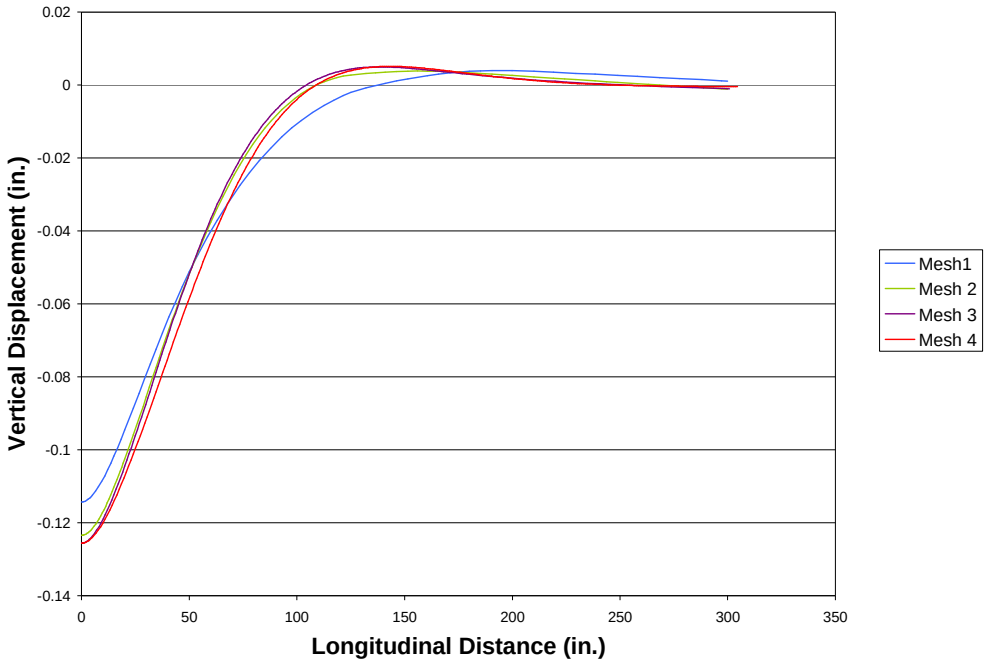

Figure 3.4: Deflected Shapes of a Half Single Rail Supported by 9-in. Ties

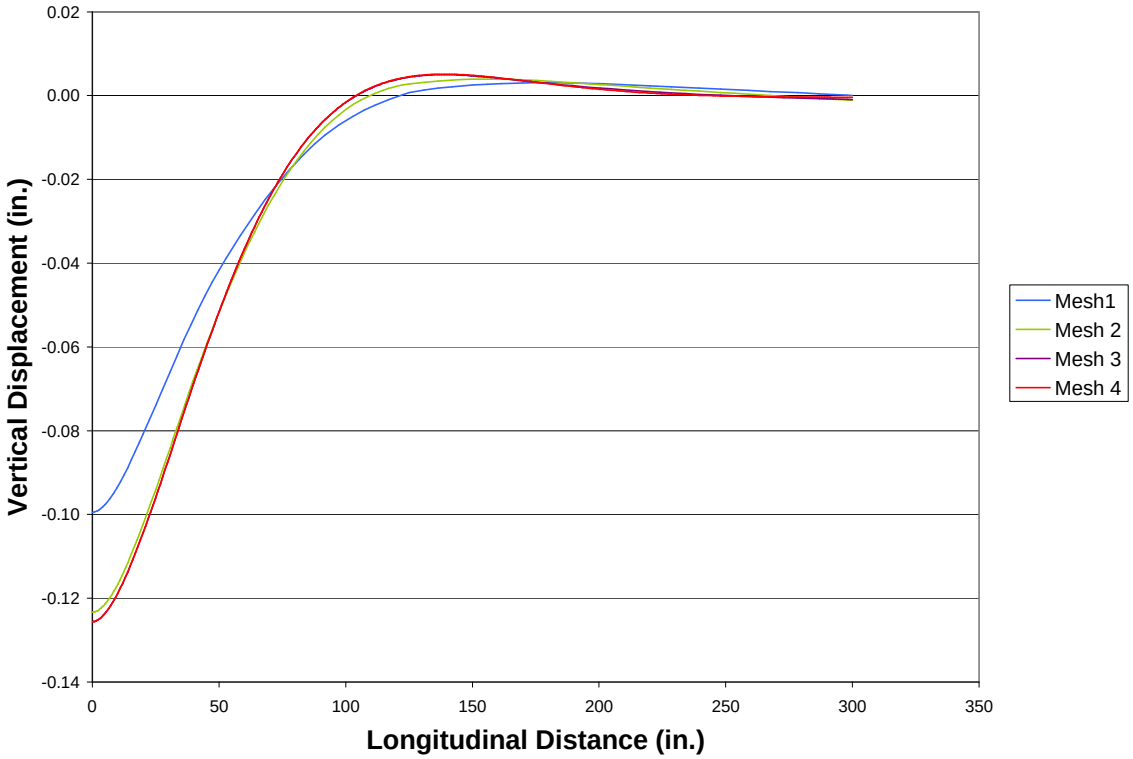

Figure 3.5: Deflected Shapes of a Half Single Rail Supported by 11-in. Ties

In these figures, the longitudinal distance of zero corresponds to the application point of the wheel load, while a longitudinal distance of 300 in. corresponds to the free end of the rail.

As shown in both the table and in the deflected shapes, as the mesh becomes increasingly coarse the stiffness of the model increases, causing the displacement at the point of load application to decrease dramatically.

Comparing the meshes and their respective deflected shapes, it is shown that in both rail configurations, the shapes for meshes 3 and 4 were very similar, and at many points indistinguishable. Thus, it was decided to use Mesh 3 as a starting point for developing the full model of the joint, since it yielded similar results to the finer Mesh 1, but halved the computer run time and would thus be easier to work with.

The mesh used for all variations of the insulated railroad joint model in this research is shown in detail in Appendix B. Shown is the mesh used for the vertical wheel load placed at the end post, where the mesh is the most refined. When the load is to be moved to another location along the joint, a similar mesh was used, with the refinement centered about the load application point.

One limitation to the mesh used for the finite element models is that the epoxy in the joint was modeled with only one element through the thickness. Since singularities exist along the edges of

the epoxy, the stress values found in the epoxy using the finite element models only give an engineering mechanics solution and do not take into account elasticity.

3.3 Length Convergence

Another aspect explored in the development of the model was the determination of the appropriate length of rail extending from the joint and wheel load application.

Three finite element models were built in ABAQUS to compare the effect of the length on the deflected shape of the rail. Again, a quarter 136 RE rail section was used, with a single concentrated point representing the wheel load. The boundary conditions were the same as those used in the mesh convergence study. The mesh used to compare these lengths was a very fine mesh, similar to that used in Mesh 4 in the mesh convergence study. Three different lengths, 300 in., 350 in., and 400 in., were compared using the two different tie widths, 9 in. and 11 in. Shown in Figures 3.6 and 3.7 are the deflected shapes of these models.

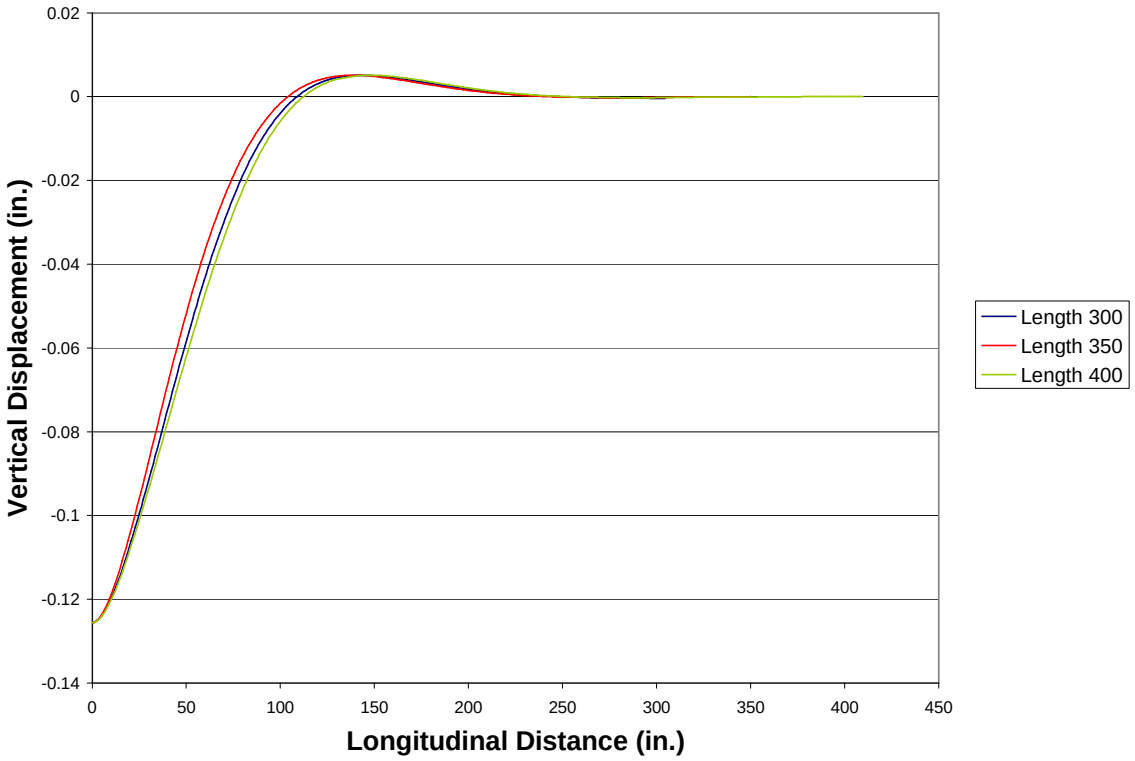

Figure 3.6: Length Convergence of Rail Supported by 9-in. Ties

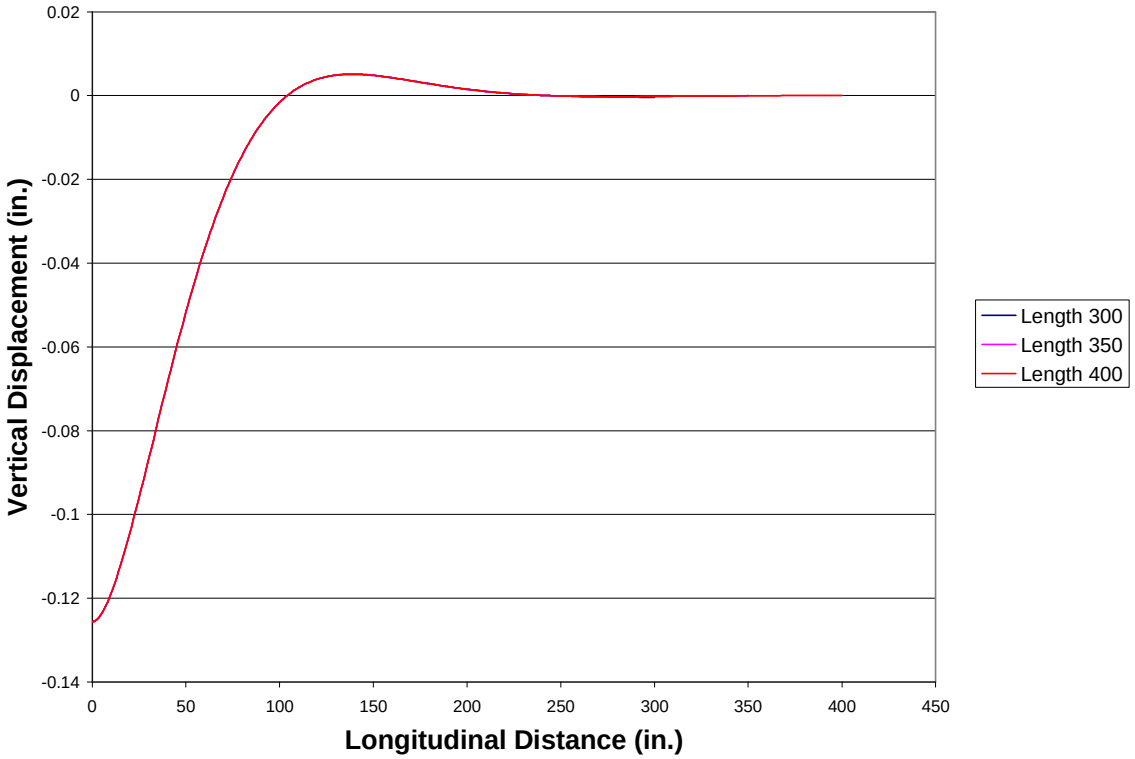

Figure 3.7: Length Convergence of Rail Supported by 11-in. Ties

In these graphs, a longitudinal distance of zero corresponds to the application point of the wheel load. Thus as the longitudinal distance increases, so does the distance from the wheel load. In Figure 3.6, it can be seen that while the shapes are very similar and the deflections at the wheel load are the same, the deflection functions are not exactly the same. However, these differences are not significant enough to justify the lengthening of the rail in order to improve accuracy in modeling. In Figure 3.7, the deflected shapes corresponding to different lengths are indistinguishable. The deflection curves for the rail supported by 9-in. ties are distinct while the deflection curves for the rail supported by 11-in. ties are not. This is due to the increased area over which the 11-in. ties are in contact with the rail. This larger area acts more like a full elastic foundation in contact with the entire bottom of the rail. Thus the differences in the resulting deflection curves for the three different lengths of rail supported by 11-in. ties are not noticeable.

From this study, it was concluded that a rail length of 300 in. on either side of the wheel load would be sufficient in providing accurate results. This specified length is also supported by the elastic foundation analytical model proposed by Hetényi (1946). In order to use this infinite beam solution to reasonably model a beam of finite length, the required length of the beam on

either side of the concentrated force must be greater than $(3\pi)/(4\lambda)$. Using the value of λ found earlier the required length of "beam" or rail for this model is 105 in. on either side of the wheel load. Thus, the length of 300 in. on either side of the wheel load, which was used for both the analytical and finite element models, is more than adequate to correctly model the rail and joint subjected to a vertical wheel load.

3.4 Implementation of Hertz Contact Theory

Utilizing the equations proposed by Hertz, values of the elliptical shape and parabolic distribution were calculated for the finite element model. Since the wheel and rail are composed of the same rail steel, the modulus of elasticity and Poisson's ratios were the same for both, and were 30,000 ksi and 0.287, respectively. In the model, a 36-in.-diameter wheel applying a load of 32,500 lb was used. The transverse radius of curvature of the 136 RE rail was 10 in. Both the transverse radius of curvature of the wheel and the principal rolling radius of the rail were considered to be infinity. The parameter φ from equation 2.17 was considered to be zero. Using these values, the value of θ was calculated to be 73.398°. Reading from a chart found in Dukkipati (2000), the interpolated values of *m* and *n* were found to be 1.2283 and 0.8319, respectively.

The result was an ellipse with a major semi-axis of 0.329 in., a minor semi-axis of 0.223 in., and an area of 0.23 in.^{2}. The equation for the resulting pressure distribution is

$$p(x,y) = \left(21{,}200\ lb/in.^2\right)\sqrt{1-\left(\frac{x}{0.329in.}\right)^2-\left(\frac{y}{0.223in.}\right)^2} \qquad (3.5)$$

This parabolic distribution was applied to the finite element model, approximated as multiple uniform pressures over small areas. The area of the ellipse was represented as 88 squares with area 0.0025 in.^{2} and 12 triangles with area 0.00125 in.^{2}, so the total area was 0.235 in.^{2}. The value of the uniform pressure over each small square was taken as Equation 3.2 evaluated at the center of the square. The value of the uniform pressure applied to the triangular areas was again Equation 3.2 evaluated at the third points of the triangle. The sum of these applied uniform pressures was calculated to ensure that the total force being applied to the model was still a wheel load of 32,500 lb.

3.5 Parametric Studies

Several parameters were investigated to examine their effects on the displacement and stress in the epoxy.

3.5.1 Tie Width

Two tie widths were considered: 9 in. and 11 in. The wheel load was placed at the end post, i.e., at the center of the insulated railroad joint, for both cases, as shown below in Figure 3.8.

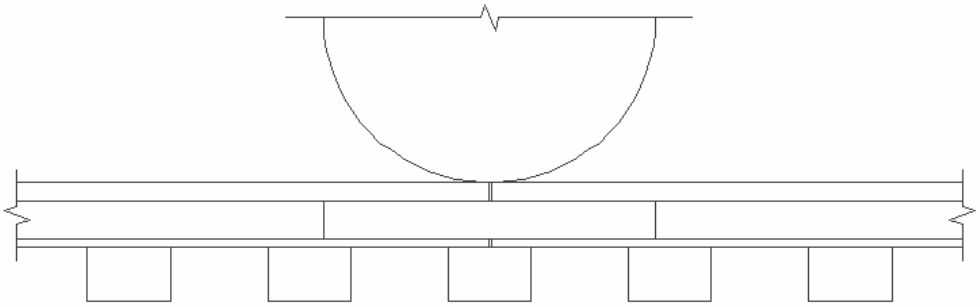

Figure 3.8: Insulated Rail Joint with 36-in. Joint Bar, Load at End Post

3.5.2 Location of Wheel Load

Two locations of the wheel load were considered, to determine the associated effect on displacement as well as on the pertinent stresses in the epoxy. The wheel load, represented by the contact patch as discussed above, was centered about the end post as well as halfway between the tie under the end post and the tie just to the left of the end post, as shown in Figure 3.9.

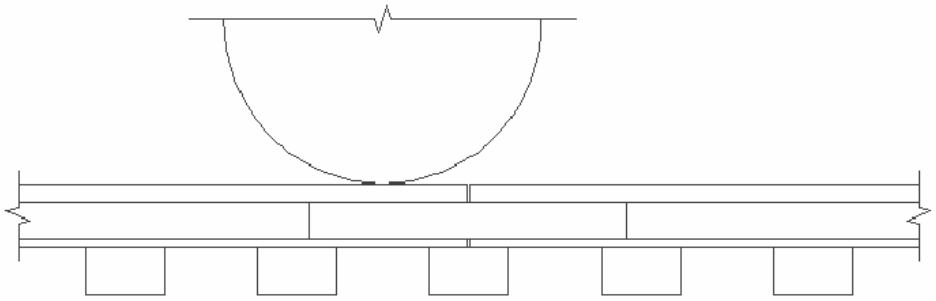

Figure 3.9: Insulated Rail Joint with 36-in. Joint Bar, Load Between Ties

3.5.3 Joint Bar Length

Two joint bar lengths, 36 in. and 48 in., were explored to see if perhaps a longer joint bar would decrease the displacement and decrease the stresses in the epoxy. The moments of inertia of the joint bars are the same for both cases. The 48-in. joint bar is supported by three 9-in. ties, as shown in Figure 3.10, and the results from the earlier 9-in.-tie model (with 36-in. joint bars) are used for comparison. The load is at the end post.

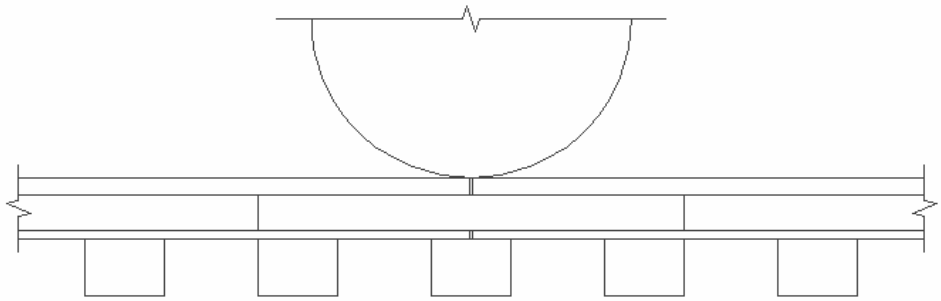

Figure 3.10: Insulated Rail Joint with 48-in. Joint Bars, Load at End Post

3.5.4 Joint Bar Moment of Inertia

The moment of inertia of the joint bar was increased from that of the standard joint bar to see if a stiffer joint bar would decrease the maximum displacement of the joint as well as decrease the stresses in the epoxy. As shown in Figure 3.11 below, the moment of inertia of a standard joint bar (a) was doubled (b) and tripled (c) simply by increasing the width of the joint bar.

(a) (b) (c)

Figure 3.11: Joint Bars with Increasing Moments of Inertia

In all three cases, the profile of the joint bar where it would fit to the 136 RE rail did not change, on the left side of the cross-sections in Figure 3.11, and thus the epoxy cross-section did not change.

CHAPTER 4 ANALYSIS AND RESULTS

As stated earlier, this research focuses on the stresses in the epoxy. For all finite element models of the insulated joint analyzed, the displaced shape, out-of-plane shear stresses, and peel stresses are compared to determine the influence of the parameters on the joint performance.

The displaced shapes of the rail and joint that are plotted here are the resulting vertical displacements of the bottom of the rail. A longitudinal distance of zero corresponds to the center of the wheel loading contact application.

In the stress contour plots, the resulting stresses have been transformed into the finite element local coordinate system. The locations of the ties are denoted by solid brown rectangles. The location of the wheel load is denoted by an arrow, and circles represent locations of maximum stress. The curved epoxy layer is flattened out to form a vertical plane for the figures.

The pertinent stresses in the analysis of the epoxy are the two out-of-plane shear stresses and the peel stresses. If the epoxy were to be a flat adhesive, as shown in Figure 4.1, these stresses would be τ_{yz}, τ_{xy}, and σ_y.

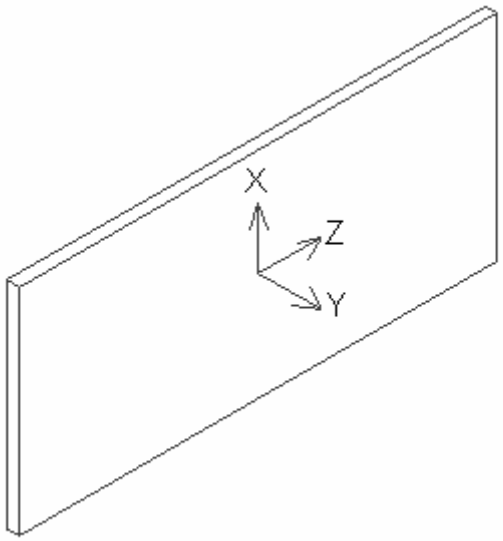

Figure 4.1: Epoxy Coordinate System

As seen with the Volkersen shear lag phenomenon, the largest out-of-plane shear stress is in the Y-Z plane; however, small strains, and therefore small shear stresses, do occur in the X-Y plane. The only shear stresses not presented here are the in-plane stresses associated with the X-Z plane,

which is parallel to the longitudinal axis of the rail. That is because the more significant deformations of the adhesive and resulting stresses occur out of plane.

For the analysis cases in which the wheel load is at the end post, only half of the epoxy is shown in the stress contour plots. In all of these symmetric loading cases, the stresses in the epoxy to the left of the wheel load are used for comparison, as shown below.

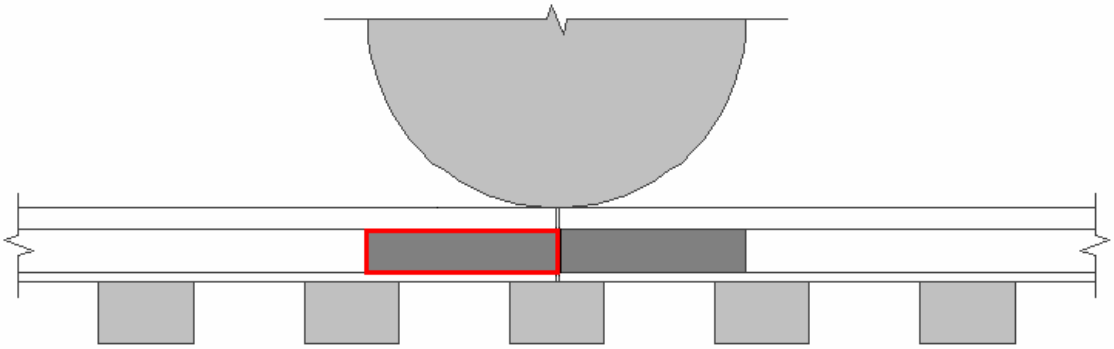

Figure 4.2: Epoxy Shown in Symmetric Loading

4.1 Tie Width

4.1.1 Load at End Post

Figure 4.3 shows the displaced shapes for a standard insulated joint, with a joint bar length of 36 in., the wheel load placed at the end post, and the rail supported by 9-in. or 11-in. ties. The maximum deflection of the rail and joint supported by 9-in. ties is 0.122 in., while the maximum deflection associated with 11-in. ties is 0.093 in., thus the ratio is 0.742 between the two maximum deflections. The larger effective area for the 11-in. ties causes an increase in total foundation resistance and results in a smaller deflection of the rail and joint. This displaced shape, which repeats in all of the finite element results, is consistent with that of a beam on elastic foundation subjected to a single concentrated force at the center of the beam, discussed earlier in section 2.2.1. Recall that in Figure 2.14, the maximum deflection of the native rail on a full elastic foundation was approximately 0.126 in. Thus including a joint supported by 9-in. ties has a minimal effect on the maximum displacement of the rail, while a joint supported by 11-in. ties decreases the maximum displacement by 24 percent.

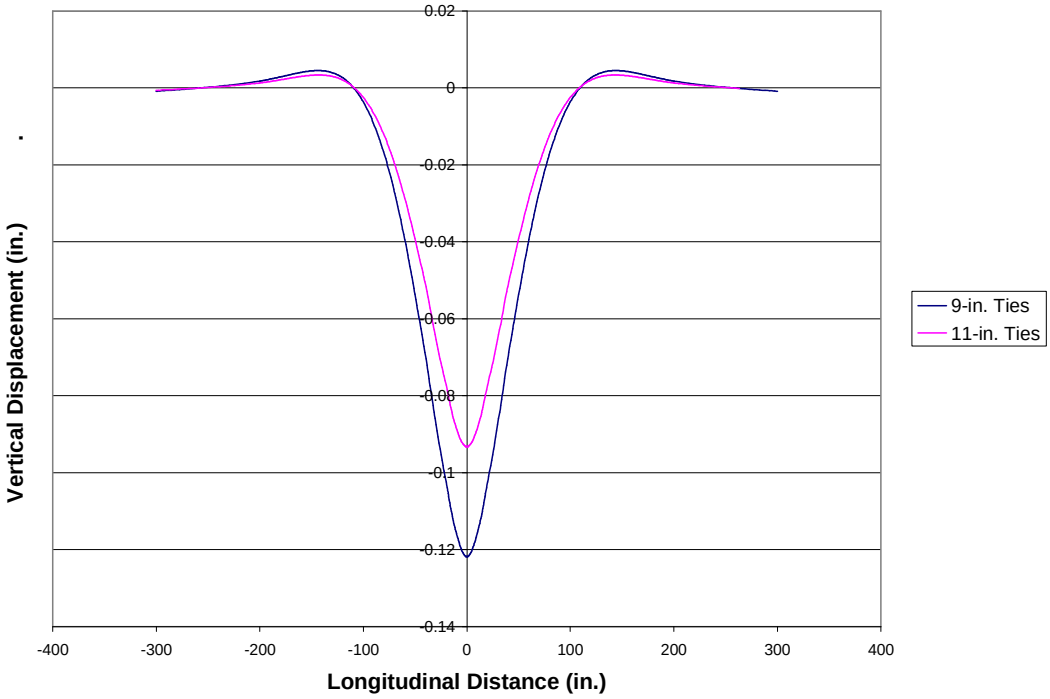

Figure 4.3: Displaced Shapes for Different Tie Widths

The relationship between the maximum displacements of the insulated rail joints supported by 9-in. and 11in. ties can also be verified using the beam on elastic foundation analysis. The equation for maximum displacement given by Hetényi (1946) is

$$y_{\max} = \frac{P\lambda}{2k} \tag{4.1}$$

Recall that *k* is the stiffness of the elastic foundation, in units of force/deflection/length, and, when divided by the width the rail, becomes force/deflection/area. Thus the stiffness of the elastic foundation used in these models becomes dependent on the effective area of the solid element ties on which the elastic foundation is applied. The load, *P*, modulus of elasticity of the joint, *E*, and moment of inertia of the joint, *I*, are the same for both the 9-in. and 11-in. tie models. Using the earlier definition of λ from equation 2.7, the relationship between the maximum displacements of the IJs on the two tie widths, which is dependent on the value of *k*, becomes dependent on the effective area of the solid element ties discussed in section 3.1. This calculation and resulting ratio between the two maximum displacements are shown below:

$$\frac{y_{9-in.\,Ties}}{y_{11-in.\,Ties}} = \left(\frac{Area_{9-in.\,Ties}}{Area_{11-in.\,Ties}} \right)^{3/4} = \left(\frac{(9\ in.)(34\ in.)}{(11\ in.)(40\ in.)} \right)^{3/4} = 0.762 \qquad (4.2)$$

The ratio between the two maximum displacements found using finite element analysis was 0.742, thus confirming that increasing the tie width does decrease the maximum displacement of the rail and insulated joint by approximately the same ratio in both types of analysis.

Earlier research on suspended joints supported by 9-in. ties, performed by Adric Eckstein and Heike Lohse-Busch, yielded a maximum displacement of the insulated joint of approximately 0.16 in. Supporting the joint by placing a tie directly under the end post thus decreases the maximum deflection by approximately 25 percent.

In all of the IJ finite element models, the solid ties were considered to be wood, which was assumed to be isotropic. In actuality, wood is an orthotropic material. Shown below in Figure 4.4 is a side view of the displaced shape of the middle tie corresponding to the IJ model with a 36-in. standard joint bar, supported by 9-in. ties. Also shown is the location of the rail as well as the application point of the vertical wheel load, depicted by an arrow.

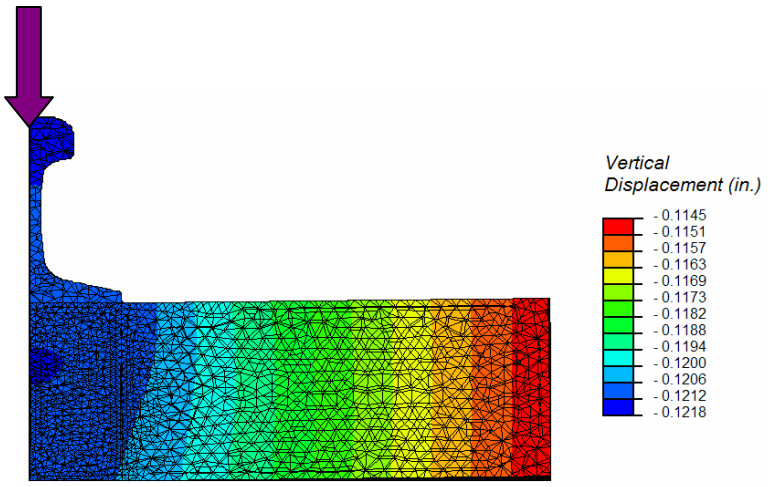

Figure 4.4: Deflected Tie Shape

As can be seen above, the slope of the tie deflection across the length of the tie is minimal, almost acting in rigid body motion. Thus it was not necessary to include the orthotropic nature of the wood. Modeling the ties surrounding the joint as solid elements in lieu of an elastic foundation was done to more accurately model the supported joint.

Figures 4.5 through 4.8 show the out-of-plane shear stresses, τ_{yz} and τ_{xy}, of the epoxy for an IJ composed of a standard 36-in. joint bar, supported by 9-in. and 11-in. ties and subjected to a

vertical wheel load at the end post.. The maximum out-of-plane shear stresses, τ_{yz}, for IJs supported by 9-in. and 11-in. ties are 4,647 psi and 4,296 psi, respectively. In both the 9-in. and 11-in. tie configurations, this maximum out-of-plane shear stress, τ_{yz}, occurs below the vertical wheel load where the vertical deflection is a maximum. At this location, the epoxy has a high curvature in order to follow the cross-sectional shape of the rail and joint bar. The maximum out-of-plane shear stresses, τ_{xy}, for IJs supported by 9-in. and 11-in. ties are 1,157 psi and 1,043 psi, respectively. While these maximum shear stresses occur at the same epoxy curvature point as the out-of-plane shear stresses, τ_{yz}, the maximum τ_{xy} shear stresses have now shifted to the outer edge of the epoxy away from the end post. However, for the out-of-plane shear stress τ_{xy}, stress concentrations can also be observed along the same outer edge, but at the upper curvature point in the epoxy.

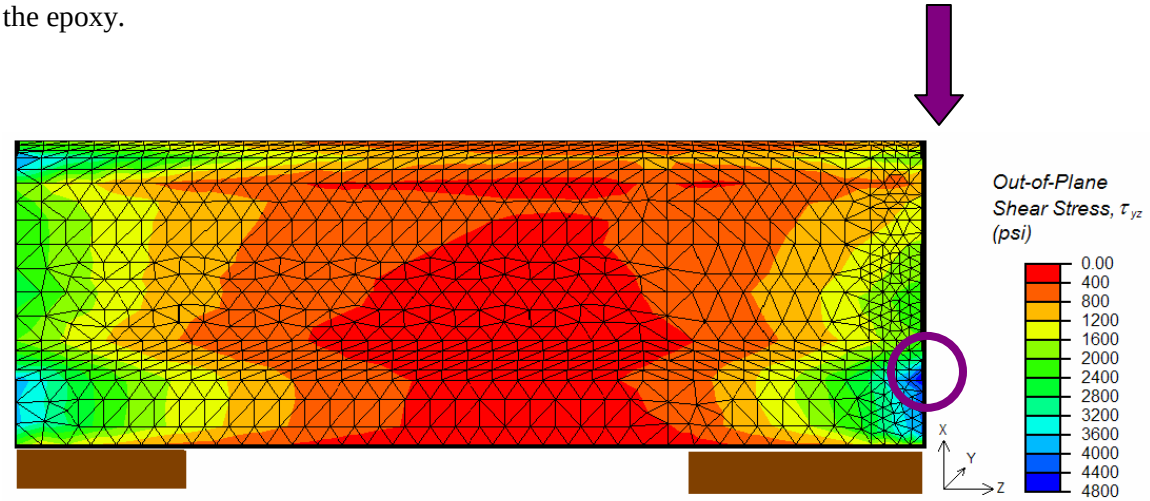

Figure 4.5: Out-of-Plane Shear Stress, τ_{yz}, in Epoxy; 9-in. Ties; 36-in. Standard Joint Bars; Load at End Post

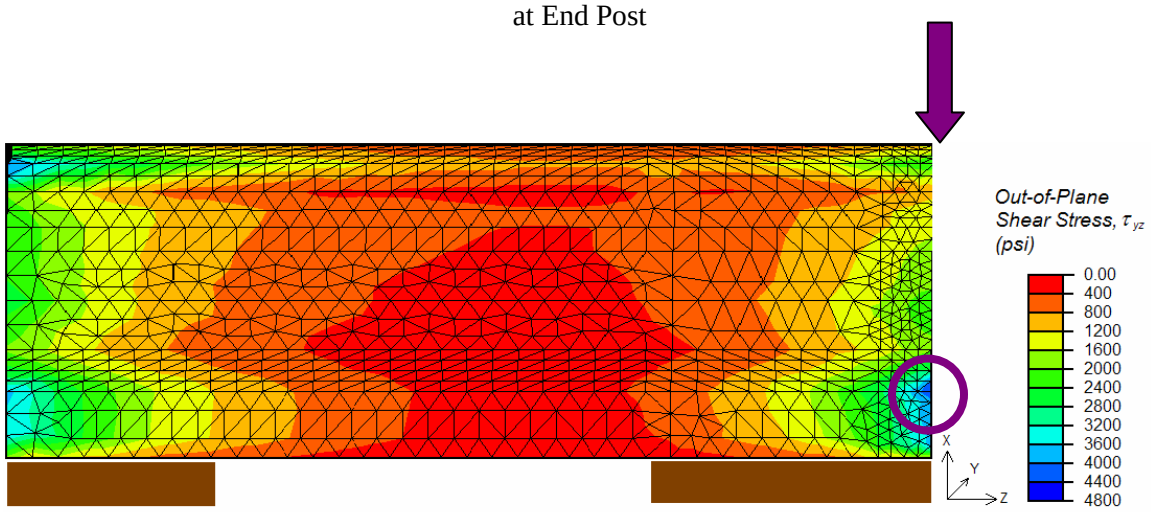

Figure 4.6: Out-of-Plane Shear Stress, τ_{yz}, in Epoxy; 11-in. Ties; 36-in. Standard Joint Bars; Load at End Post

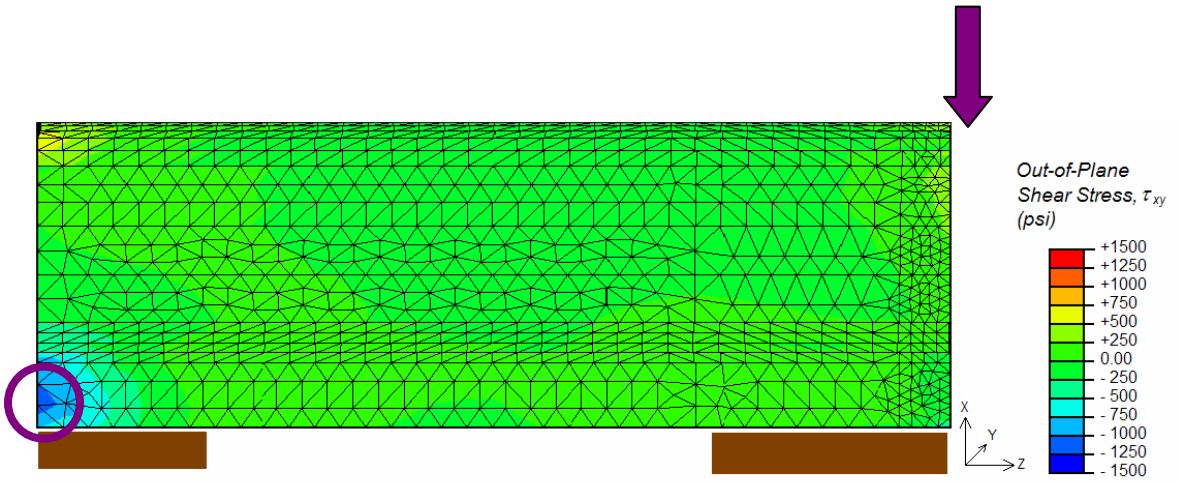

Figure 4.7: Out-of-Plane Shear Stress, τ_{xy}, in Epoxy; 9-in. Ties; 36-in. Standard Joint Bars; Load at End Post

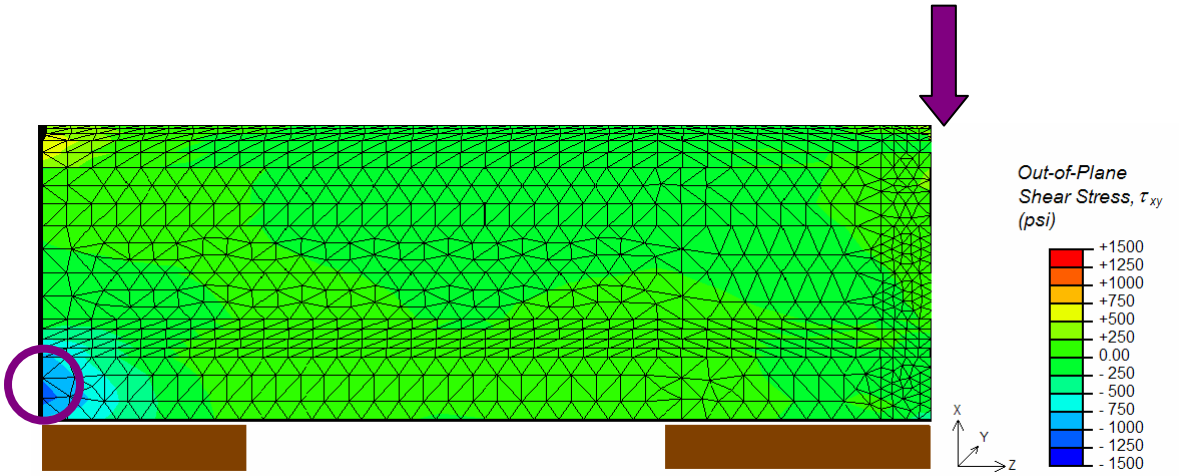

Figure 4.8: Out-of-Plane Shear Stress, τ_{xy}, in Epoxy; 11-in. Ties; 36-in. Standard Joint Bars; Load at End Post

As confirmed by the earlier investigation of Volkersen's equations, the magnitude of the major out-of-plane shear stress, τ_{yz}, along the joint is greatest at the edges and least at the center of the epoxy in both tie width cases. This is confirmed by the τ_{yz} shear stress profiles shown in Figure 4.9. In these stress profiles, a longitudinal distance of 0 in. corresponds to the edge of the joint adjacent to the end post, while a longitudinal distance of 18 in. corresponds to the edge of the joint away from the end post.

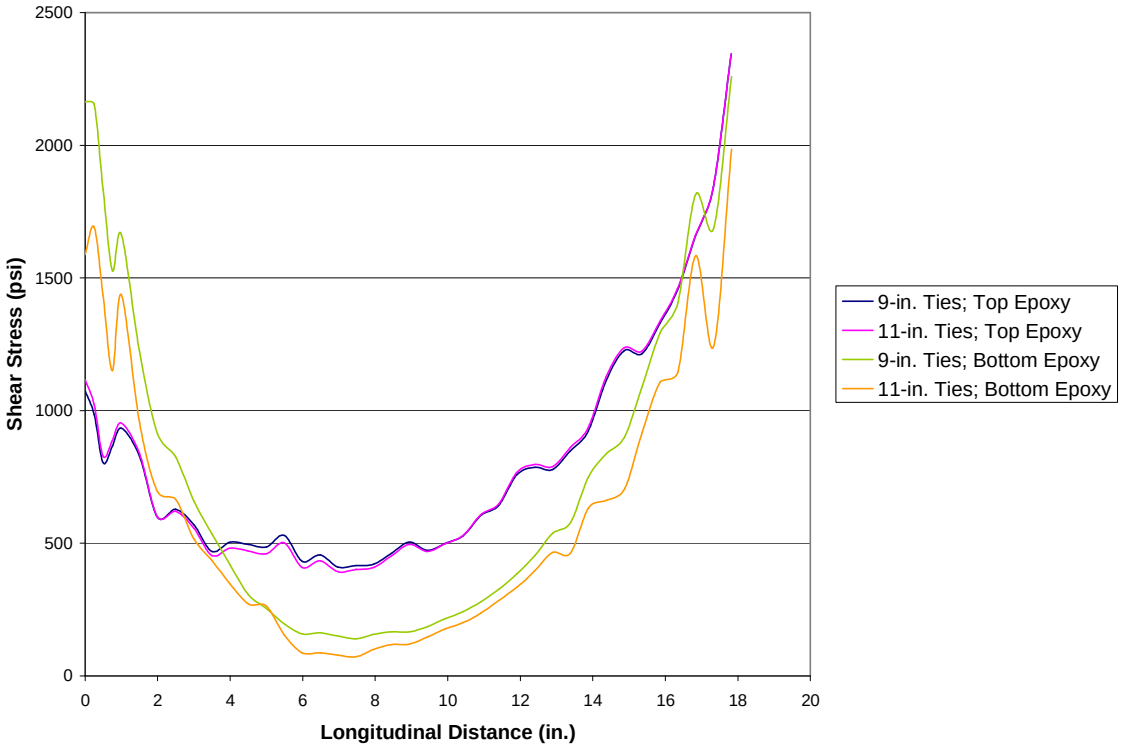

Figure 4.9: Shear Stress Profiles of Epoxy Along Joint

The stress profiles of the epoxy follow closely the shape predicted earlier by the simplified joint, shown in Figure 2.7. Note that the shear stress along the top of the joint is greatest at the outer edge and lower at the edge closer to the gap. Again this is a result of the differing stiffnesses between the rail and joint bars. The load is attracted to the stiffer member and thus the shear stress is greatest at the edge corresponding to the joint bar. This difference is less noticeable along the bottom of the epoxy. This is due to the additive properties of the stresses caused by the different loadings. While the bending stresses will magnify the asymmetry of the shear stresses (due to the tensile load) at the top of the epoxy, they will almost cancel out the asymmetry at the bottom of the epoxy. From Figure 4.9, one can also see that the shear stresses along the top edge of the epoxy for both models are almost indistinguishable in magnitude. However, along the bottom edge, the shear stress of the joint supported by 9-in. ties is consistently slightly greater than that of the joint supported by 11-in. ties.

Figures 4.10 and 4.11 show the peel stresses for these insulated joint configurations. The location of the maximum tensile peel stress is shown with a red circle and the maximum compressive peel stress (i.e., the most-negative value) is shown with a blue circle.

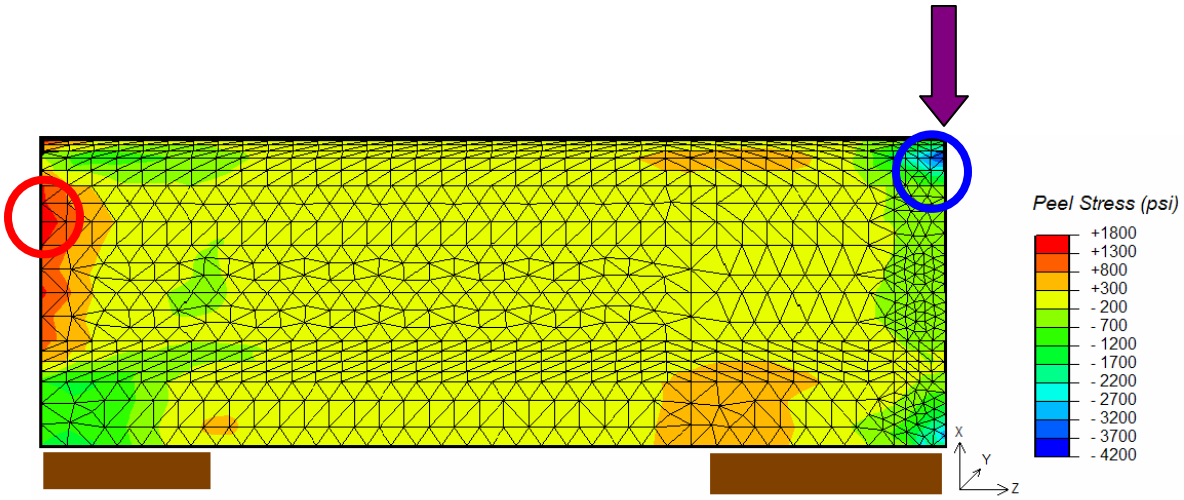

Figure 4.10: Peel Stress in Epoxy; 9-in. Ties; 36-in. Standard Joint Bars; Load at End Post

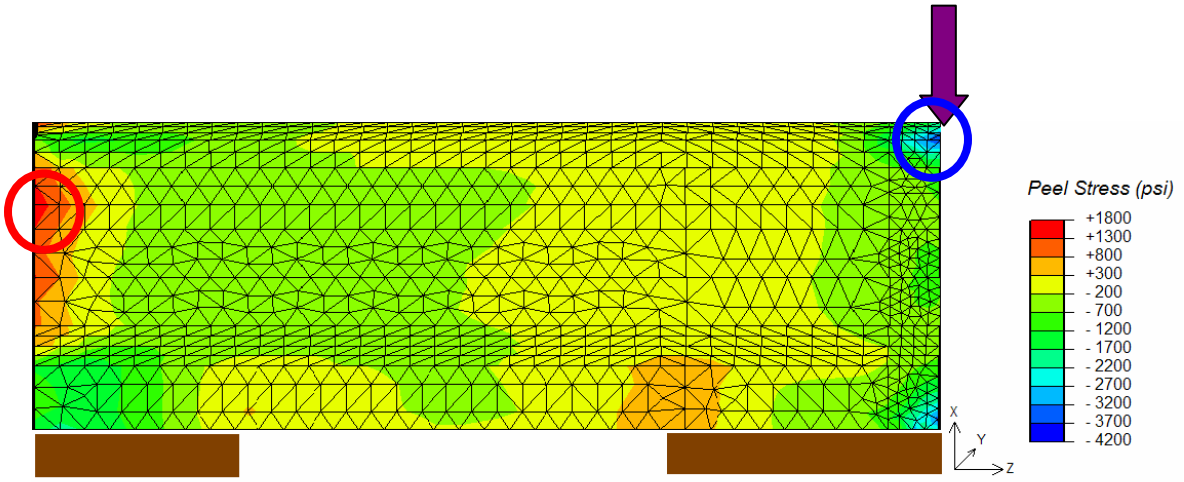

Figure 4.11: Peel Stress in Epoxy; 11-in. Ties; 36-in. Standard Joint Bars; Load at End Post

In both the joint supported by 9-in. ties and the joint supported by 11-in. ties, the maximum compressive peel stress occurs directly under the vertical wheel load. This is due to the fact that the vertical wheel load is pressing the rail head down, compressing the adhesive between the rail head and the joint bar. For the joint supported by 9-in. ties, the maximum compressive peel stress is 3,710 psi, while the maximum compressive peel stress for the 11-in. tie model is slightly lower at 3,032 psi. Both models also have a compressive peel stress concentration located below the wheel load application point at the bottom of the rail. This is due to the reaction force from the tie and ballast pressing the rail base up, compressing the epoxy. Similar to the compressive peel stress, the maximum tensile peel stress for both models occurs in the same location, the edge of the epoxy away from the end post. The maximum tensile peel stresses for IJs supported by 9-in. and 11-in. ties are 1,617 psi and 1,615 psi, respectively. Small tensile peel stress concentrations can also be observed in the lower part of the epoxy at the edges of ties.

4.1.2 Load Between Ties

Shown in Figure 4.12 are the displaced shapes of the joint supported by both 9-in. and 11- in. ties, with the load placed at the end post as well as between two ties. For a better comparison, displaced shapes of the models with the off-center load have been shifted to the right, so that the locations of the center of the wheel loads for both models are at the same longitudinal location.

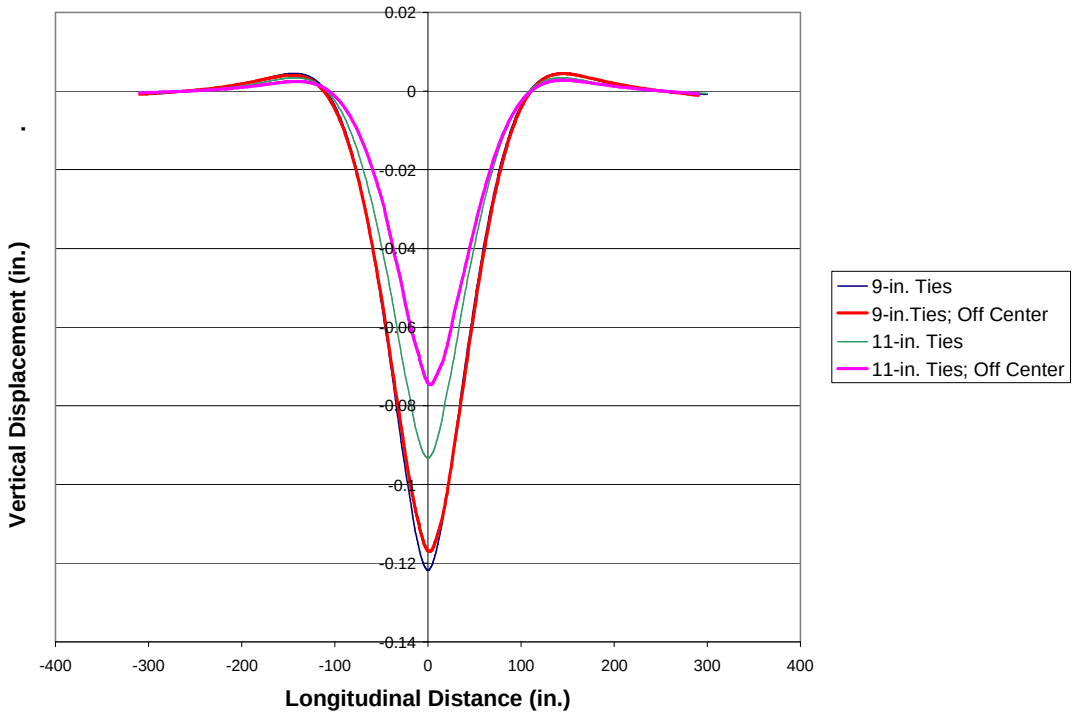

Figure 4.12: Displaced Shapes for Different Tie Widths with Load at End Post and Load Between Ties

The maximum displacement for both the 9-in. ties and the 11-in. tie joints decreases slightly when the load moves away from the end post. The difference is most noticeable in the joint supported by 11-in. ties. Also, the maximum vertical deflection does not occur directly below the center of the wheel load when the load is off-center. This is due to the asymmetry of the "rail-joint beam" surrounding the load. To the right of the load, the joint bar and rail, which combine for a larger moment of inertia, occur for a length of 27.75 in., while to the left, this larger moment of inertia only occurs for a length of 8.25 in.

The values of these maximum displacements for the IJ subjected to off-center loading and supported by 9-in. and 11-in. ties are 0.118 in. and 0.091 in. respectively. The ratio of these maximum displacements is 0.77, close to the expected value of 0.76 as discussed earlier.

Again, the maximum deflection is consistently less for the IJ when compared to the native rail.

Figures 4.13 through 4.16 depict the out-of-plane shear stresses, τ_{yz} and τ_{xy}, of the epoxy for an IJ composed of a standard 36-in. joint bar, supported by 9-in. and 11-in. ties and subjected to a vertical wheel load between two ties.

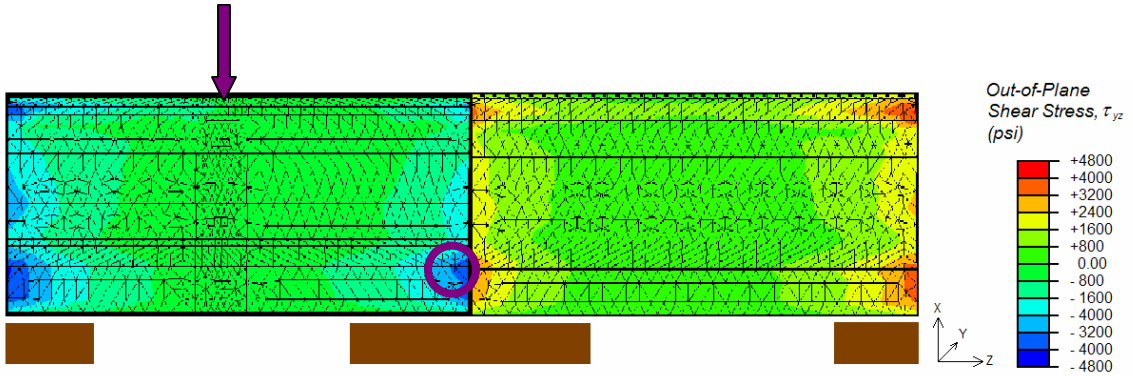

Figure 4.13: Out-of-Plane Shear Stress, τ_{yz}, in Epoxy; 9-in. Ties; 36-in. Standard Joint Bars; Load Between Ties

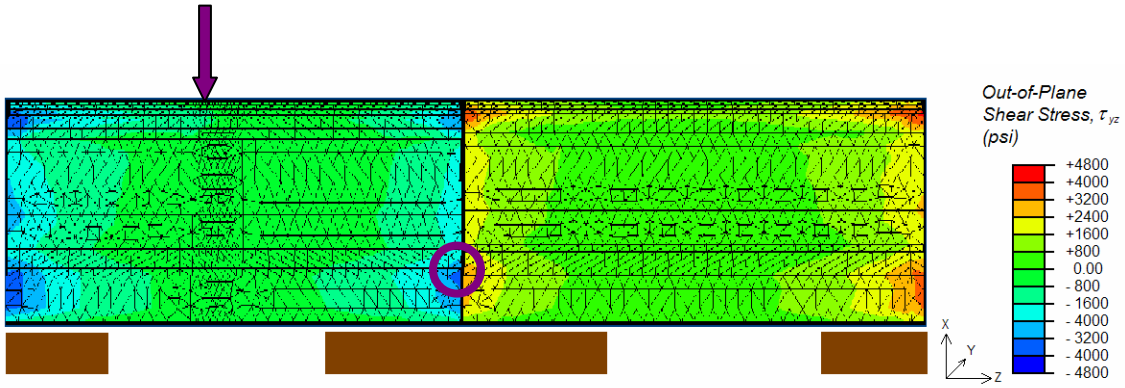

Figure 4.14: Out-of-Plane Shear Stress, τ_{yz}, in Epoxy; 11-in. Ties; 36-in. Standard Joint Bars; Load Between Ties

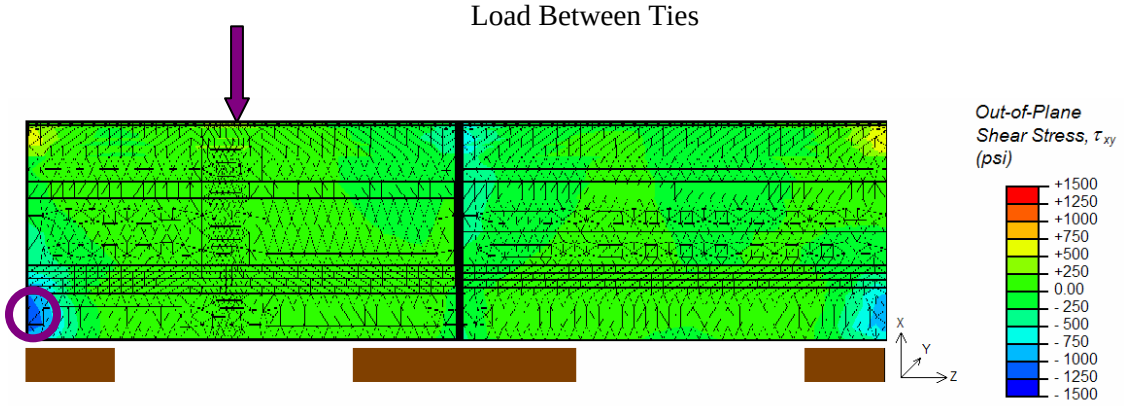

Figure 4.15: Out-of-Plane Shear Stress, τ_{xy}, in Epoxy; 9-in. Ties; 36-in. Standard Joint Bars; Load Between Ties

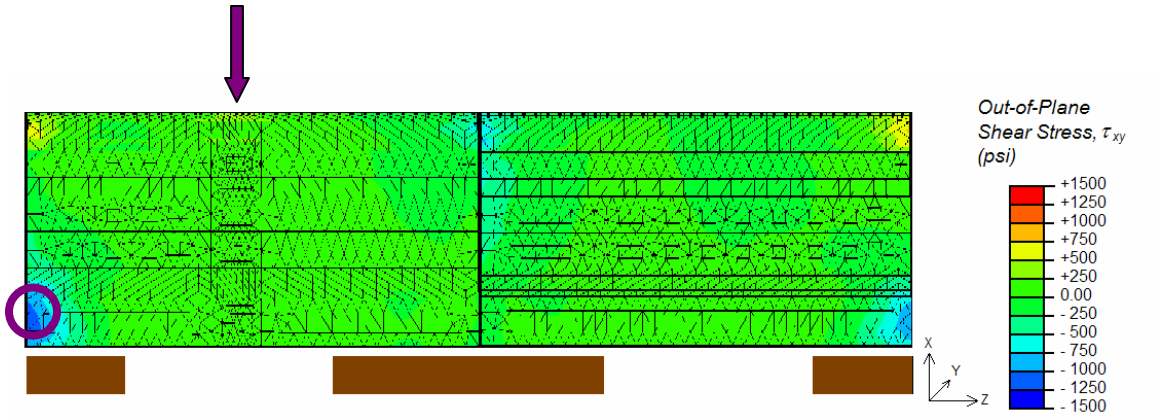

Figure 4.16: Out-of-Plane Shear Stress, τ_{xy}, in Epoxy; 11-in. Ties; 36-in. Standard Joint Bars; Load Between Ties

As with the load at the end post, the maximum τ_{yz} shear stress occurs at the edge of the epoxy nearest the end post and at the lower bend in the epoxy. The maximum τ_{yz} shear stress of the joint supported by 9-in. ties is 4,178 psi, and the maximum τ_{yz} shear stress of the joint supported by 11-in. ties is 4,009 psi. The phenomenon of shear lag is again present in these contours, since the magnitude of the shear stress along the joint is greatest at the edges and least at the center of the epoxy. Also, as with the load at the end post, the maximum τ_{xy} shear stress occurs at the edge of the epoxy away from the end post and at the lower bend in the epoxy. The maximum τ_{xy} shear stress of the joint supported by 9-in. ties is 1,212 psi, and the maximum τ_{xy} shear stress of the joint supported by 11-in. ties is 1,205 psi. All of these maximum out-of-plane shear stress values are lower than those found when the wheel load was centered at the end post.

Figures 4.17 and 4.18 show the peel stress contours for the off-center load with 9-in. and 11-in. ties, respectively. In both cases, the maximum compressive peel stress, as before, occurs just below the application point of the wheel load. The maximum tensile peel stress for both cases occurs in the epoxy on the rail not loaded by the wheel. This tensile stress does occur at the edge closest to the end post, and at a place of high curvature in the epoxy. The maximum compressive peel stress for the 9-in. tie model is 2,264 psi, while for the 11-in. tie model it is 2,253 psi. These values are also lower than those for the earlier models in which the wheel was placed at the end post. Again, compressive peel stress concentrations can be seen at tie locations. The maximum tensile peel stresses, however, are 1,659 psi and 1,624 psi for the 9-in. and 11-in. tie models, respectively. The location of the maximum tensile peel stress is significant due to the fact that many “unzipping” bond failures tend to initiate near the end post.

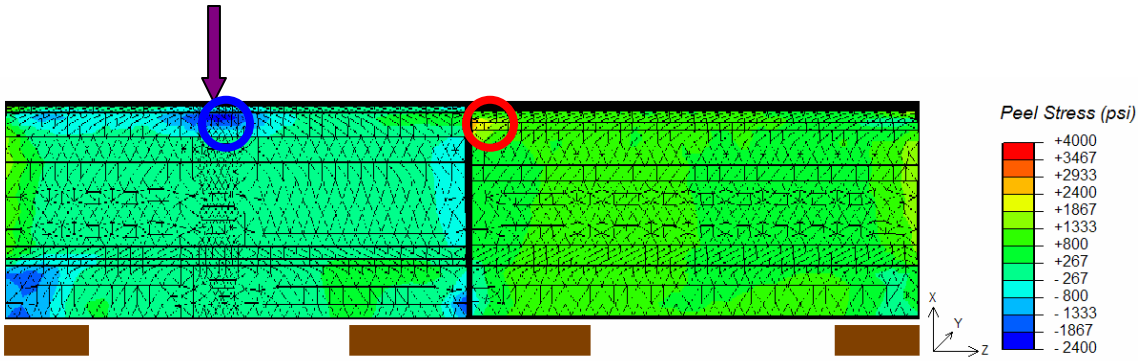

Figure 4.17: Peel Stress in Epoxy; 9-in. Ties; 36-in. Standard Joint Bars; Load Between Ties

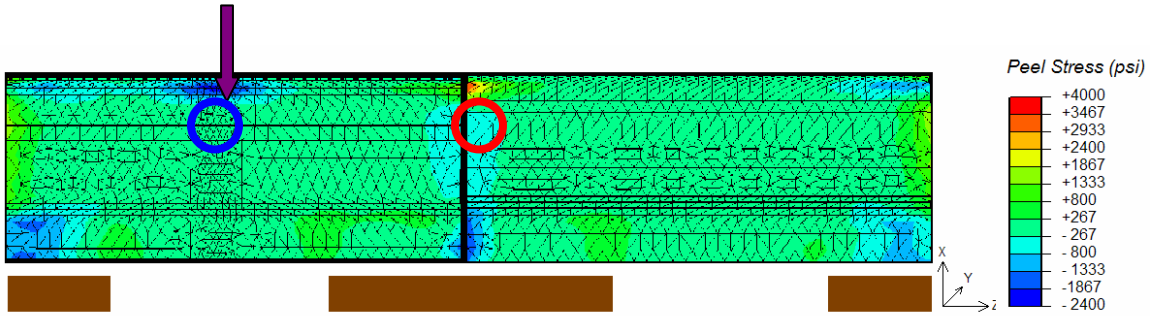

Figure 4.18: Peel Stress in Epoxy; 11-in. Ties; 36-in. Standard Joint Bars; Load Between Ties

4.2 Joint Bar Length

4.2.1 Load at End Post

The 48-in. joint bar is supported by 9-in. ties, and the results from the earlier 9-in. tie model with 36-in. joint bars in section 4.1.1 are used for comparison. As seen in Figure 4.19, the displacement of the IJ and surrounding rail is barely affected by the increased joint bar length. However, both of these displaced shapes again illustrate the point that the rail that includes a joint has a slightly smaller maximum displacement than the native rail.

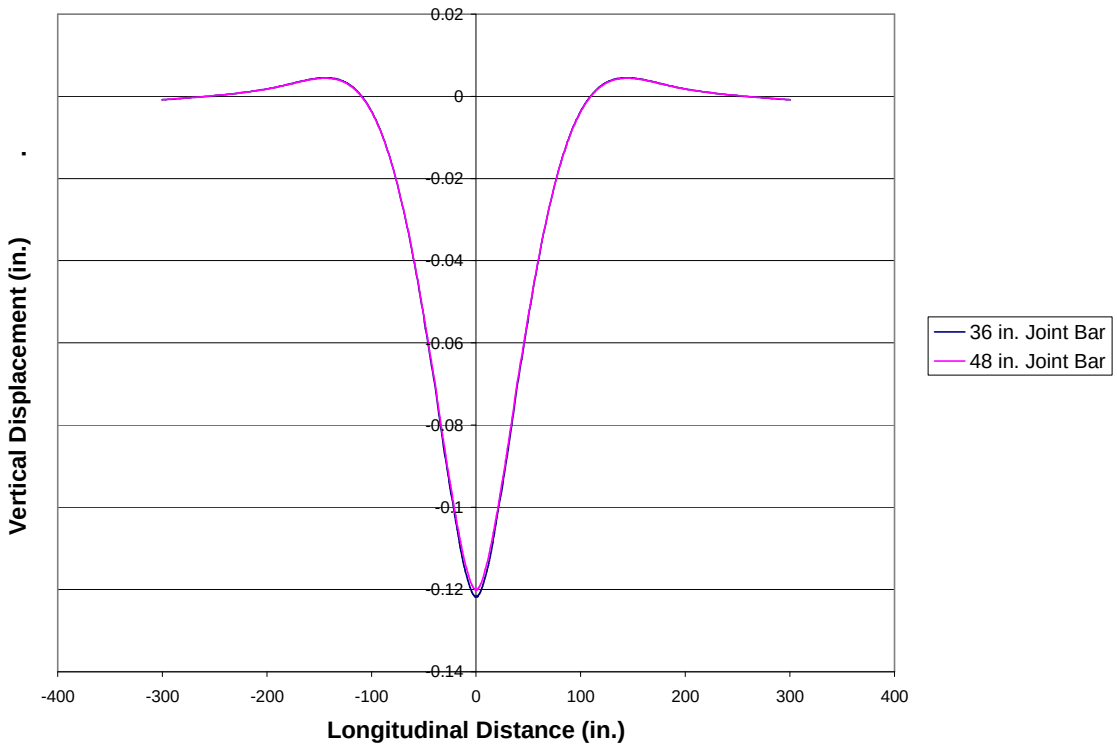

Figure 4.19: Displaced Shapes for Different Joint Bar Lengths

Again, due to symmetry, only one-half of the epoxy from this model is shown for the stress contour plots. Out-of-plane shear stress contours are depicted in Figures 4.20 and 4.21, and peel stress contours in Figure 4.22. As with the 36-in. joint bar, the 48-in. joint bar model has the maximum τ_{yz} shear stress occurring just below the wheel load at the lower bend in the epoxy, as well as the maximum τ_{xy} shear stress occurring at the edge away from the end post in the lower bend of the epoxy, with another τ_{xy} shear stress concentration located along this edge in the upper bend of the epoxy. This again demonstrates the phenomenon of shear lag. The maximum out-of-plane shear stressses, τ_{yz} and τ_{xy}, have magnitudes of 4,620 psi and 923 psi, respectively. Both of these values are slightly lower than the maximum out-of-plane shear stresses found with a 36-in. joint bar.

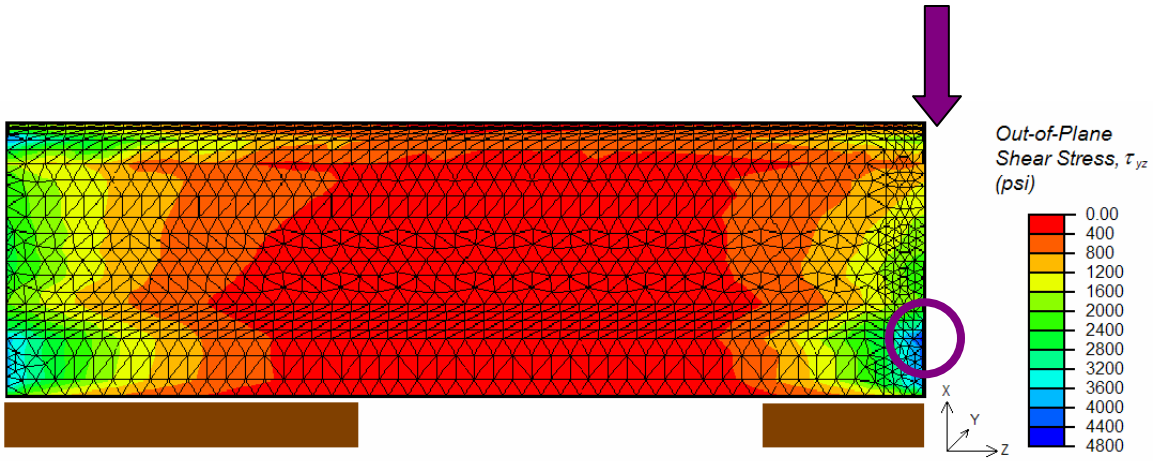

Figure 4.20: Out-of-Plane Shear Stress, τ_{yz}, in Epoxy; 9-in. Ties; 48-in. Standard Joint Bars; Load at End Post

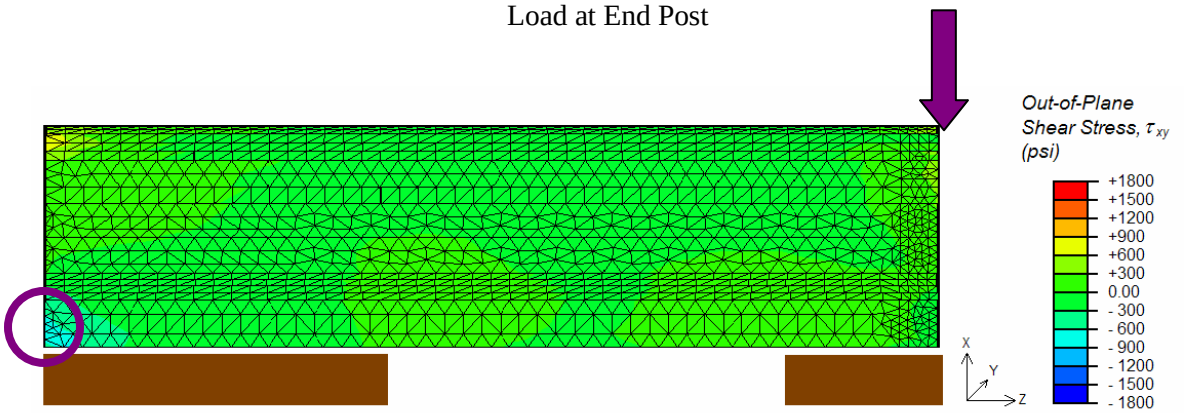

Figure 4.21: Out-of-Plane Shear Stress, τ_{xy}, in Epoxy; 9-in. Ties; 48-in. Standard Joint Bars; Load at End Post

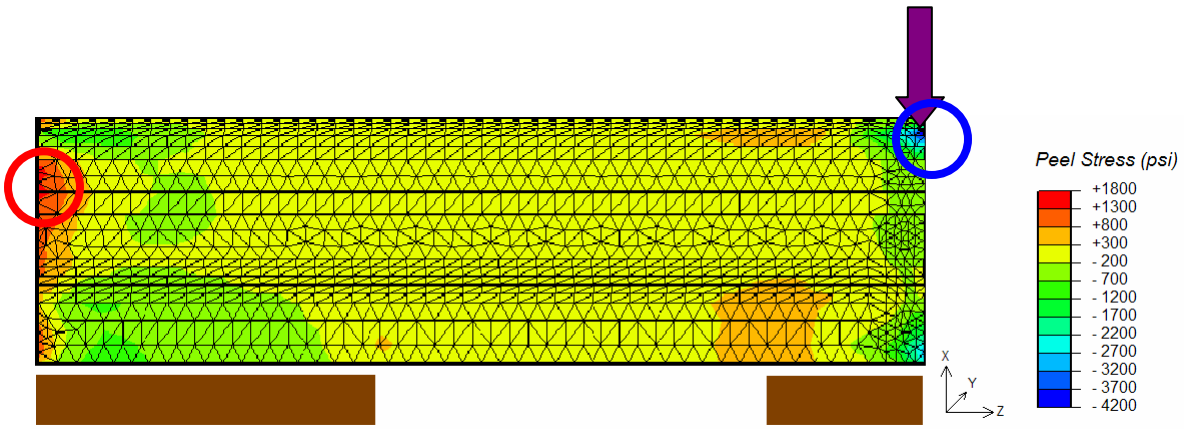

Figure 4.22: Peel Stress in Epoxy; 9-in. Ties; 48-in. Standard Joint Bars; Load at End Post

Figure 4.22 shows the peel stresses associated with the 48-in. joint bar. Similar to the 36-in. joint bar model, the maximum compressive peel stress occurs below the wheel load, with a compressive stress concentration also observed below the wheel load in the lower part of the

epoxy. The maximum tensile peel stress occurs at the edge of the epoxy away from the wheel load, with small tensile peel stress concentrations at the edge of the ties. The magnitudes of the maximum compressive and maximum tensile peel stresses are 1,726 psi and 3,854 psi, respectively. These stresses are slightly higher than those found using a 36-in. joint bar.

4.3 Joint Bar Moment of Inertia

4.3.1 Load at End Post

The displacements of the IJs using joint bars with increasing moments of inertia are shown in Figure 4.23.

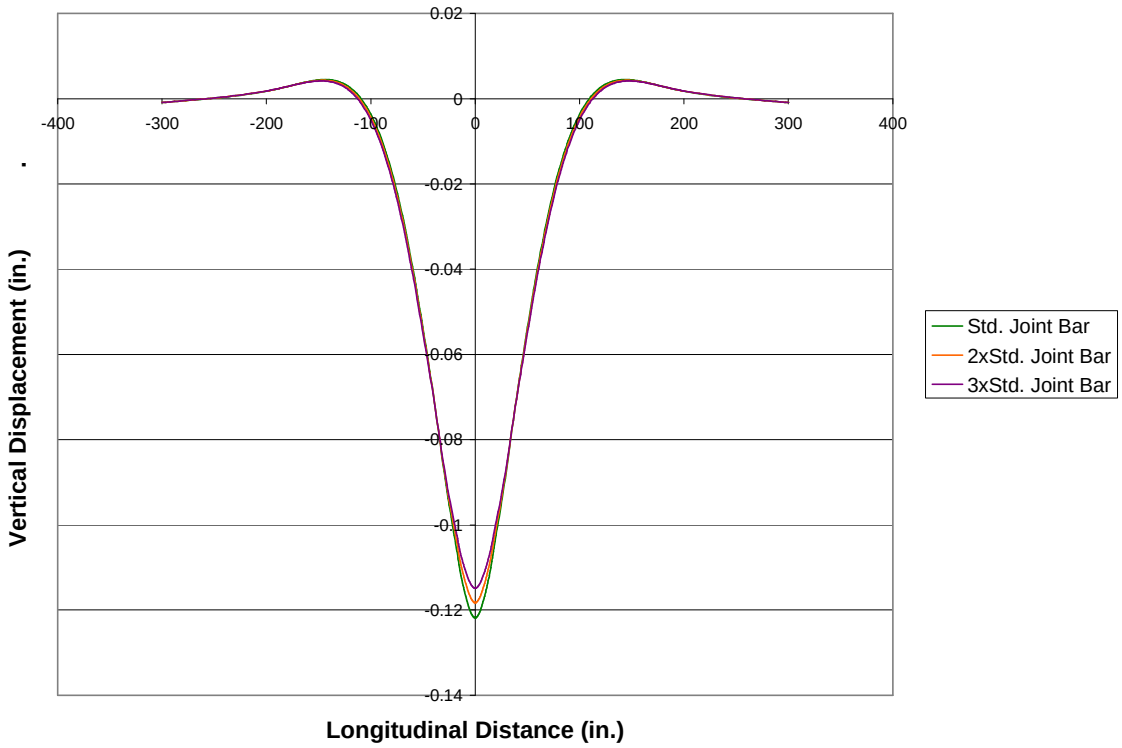

Figure 4.23: Displaced Shapes for Different Joint Bar Moments of Inertia

Since deflection is inversely related to the moment of inertia of a beam, an increased moment of inertia over the joint bar length decreases the maximum deflection of the joint bar. However, this effect of the increased joint bar moment of inertia is not significant over the entire model, since the 300 in. length of rail on either side of the end post is much greater than the 18 in. half length of the joint bar surrounding the end post. The deflected shapes of all three joint bars are indistinguishable after a longitudinal distance of 18 in. on either side of the end post. The

maximum deflection for a standard joint bar was 0.122 in., and the maximum deflections for the doubled and tripled moment of inertia joint bars are 0.118 in. and 0.115 in., respectively.

Shown in Figure 4.24 is a plot of the bending moment distribution through the rail and IJ for the increasing joint bar moments of inertia.

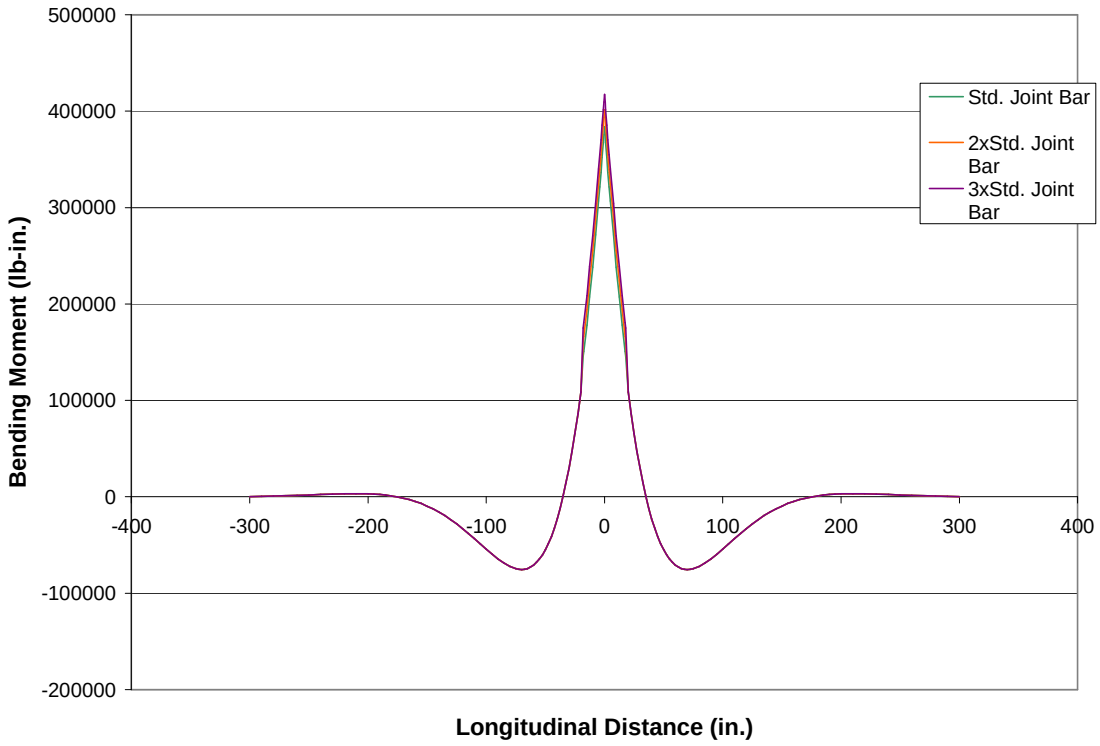

Figure 4.24: Bending Moment Distribution with Increasing Joint Bar Moments of Inertia

Again, one can see the localized effect of the increased joint bar moment of inertia. The shape of the bending moment distribution is consistent with that found by Heike Lohse-Busch (Lambrecht and Lohse-Busch, 2006), in which a discontinuity of the bending moment exists at the longitudinal distances corresponding to the ends of the joint bars.

Figures 4.25 and 4.26 show the out-of-plane shear stresses, τ_{yz}, of the epoxy for an IJ composed of a 36-in. joint bar with a doubled moment of inertia and a tripled moment of inertia, respectively. Both joints are supported by 9-in. ties and subjected to a vertical wheel load at the end post. Figures 4.27 and 4.28 show the out-of-plane shear stresses, τ_{xy}, for the same two joint models.

In both models, the maximum out-of-plane shear stress, τ_{yz}, has now moved to the edge of the epoxy away from the end post. The larger moments of inertia increase the stiffnesses of the joint

bars, attracting more load and causing the maximum shear stress location to move. This change in location places both maximum out-of-plane shear stresses, τ_{yz} and τ_{xy}, at the edge of the epoxy away from the end post, in the lower curve of the epoxy.

As with earlier models, the phenomenon of shear lag, where the shear stresses are minimal at the center of the epoxy and maximum at the edges, is illustrated. Also, out-of-plane shear stress τ_{xy} is again concentrated at the upper bend of the epoxy, along the edge away from the end post.

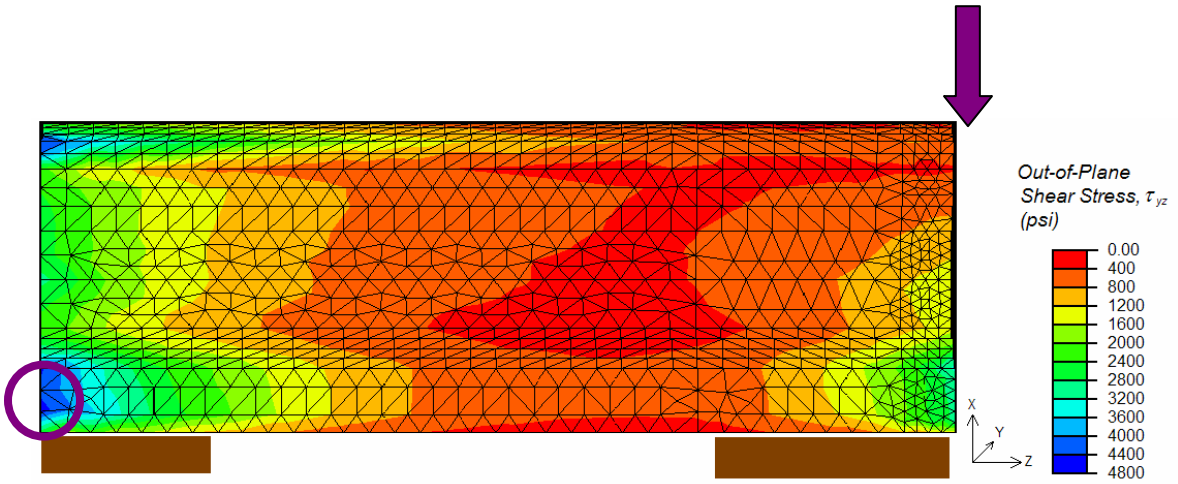

Figure 4.25: Out-of-Plane Shear Stress, τ_{yz}, in Epoxy; 9-in. Ties; 36-in. Joint Bars with 2*Std. Joint Bar Moment of Inertia; Load at End Post

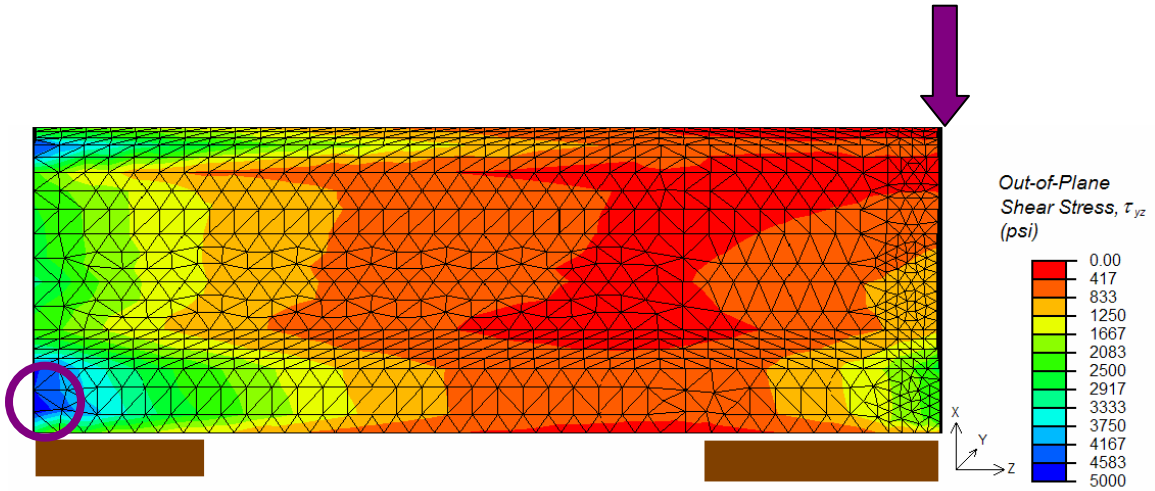

Figure 4.26: Out-of-Plane Shear Stress, τ_{yz}, in Epoxy; 9-in. Ties; 36-in. Joint Bars with 3*Std. Joint Bar Moment of Inertia; Load at End Post

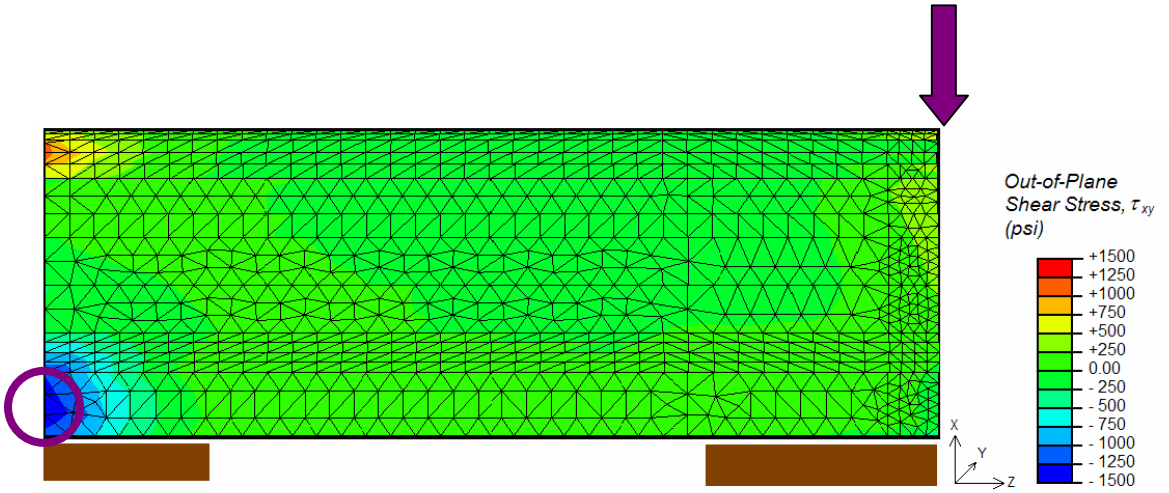

Figure 4.27: Out-of-Plane Shear Stress, τ_{xy}, in Epoxy; 9-in. Ties; 36-in. Joint Bars with 2*Std. Joint Bar Moment of Inertia; Load at End Post

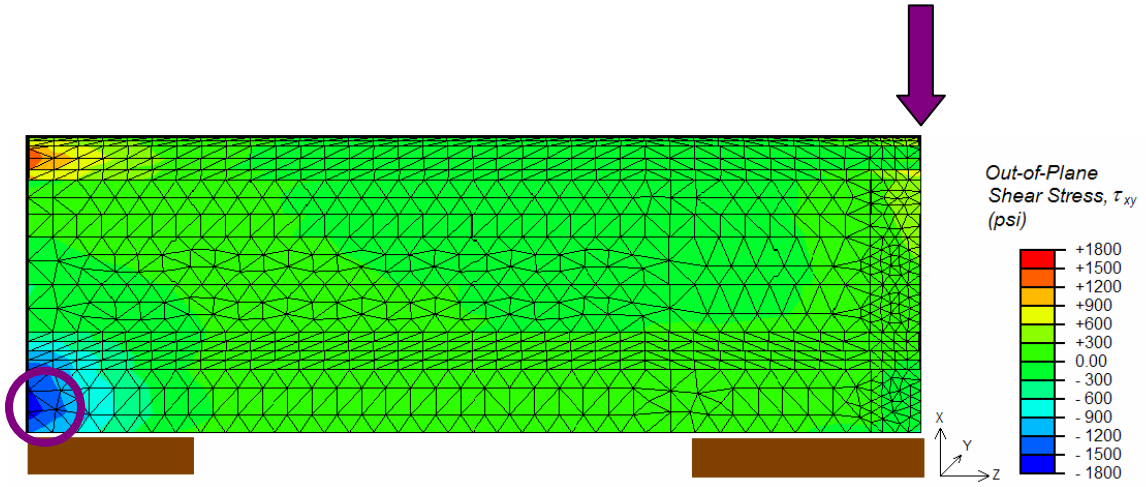

Figure 4.28: Out-of-Plane Shear Stress, τ_{xy}, in Epoxy; 9-in. Ties; 36-in. Joint Bars with 3*Std. Joint Bar Moment of Inertia; Load at End Post

The maximum τ_{yz} out-of-plane shear stresses for the doubled and tripled moment of inertia joint bars are 4,575 psi and 4,917 psi, respectively. While the doubled moment of inertia joint bar sees a decrease in this shear stress, the τ_{yz} shear stress for the tripled moment of inertia joint bar increases from the standard joint bar, which had a value of 4,647 psi.

The maximum τ_{xy} out-of-plane shear stresses for the doubled and tripled moment of inertia joint bars are 1,513 psi and 1,684 psi, respectively. These values have increased monotonically with the increasing moment of inertia, from the τ_{xy} out-of-plane shear stress of the standard joint bar, which had a value 1,157 psi.

The peel stresses associated with the increased moment of inertia joint bars subjected to loading at the end post are shown in Figures 4.29 and 4.30.

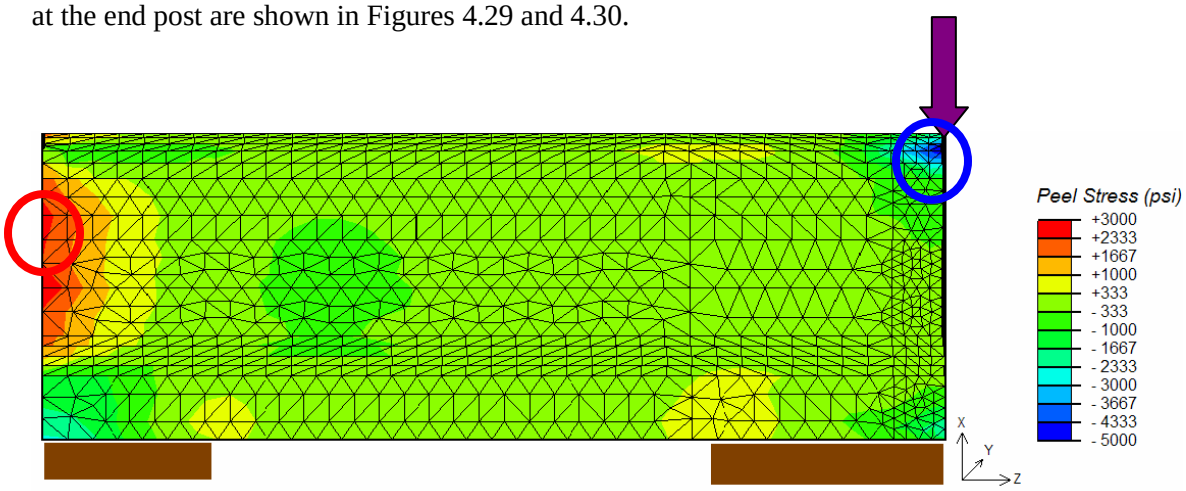

Figure 4.29: Peel Stress in Epoxy; 9-in. Ties; 36-in. Joint Bars with 2*Std. Joint Bar Moment of Inertia; Load at End Post

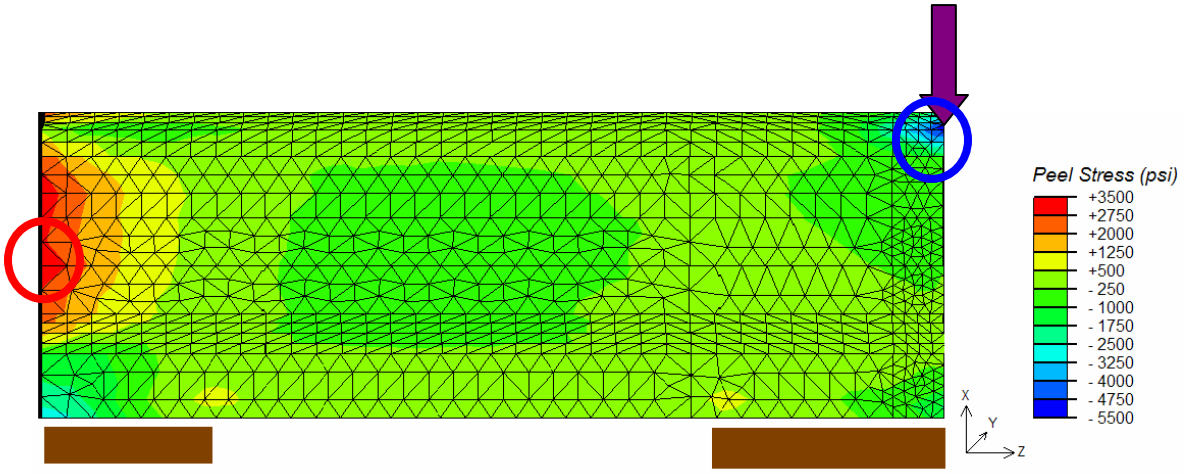

Figure 4.30: Peel Stress in Epoxy; 9-in. Ties; 36-in. Joint Bars with 3*Std. Joint Bar Moment of Inertia; Load at End Post

As with all of the other IJ models discussed earlier, the maximum compressive peel stresses for both the doubled and tripled moment of inertia joint bars occur below the application point of the vertical wheel load, as well as compressive stress concentrations in the lower portion of the epoxy above ties. Also, similar to the standard joint bar, the maximum tensile peel stress occurs at the edge of the epoxy away from the end post. The maximum compressive peel stresses for the doubled and tripled moment of inertia joint bars are 4,896 psi and 5,057 psi, respectively. The maximum tensile peel stresses for the doubled and tripled moment of inertia joint bars are 2,896

psi and 3,445 psi, respectively. As with the out-of-plane shear stress, τ_{xy}, the maximum peel stresses observed in the epoxy increase with the increasing joint bar moments of inertia.

The increasing peel stresses with increasing moments of inertia are consistent with the work of Hart-Smith (1973). In that investigation into the elastic peel stresses in double-lap joints, it was proposed that the maximum peel stress in the adhesive be defined by the following equation:

$$\sigma_{c_{max}} = \tau\left(\frac{3E_c'(1-\nu^2)t_o}{E_o\eta}\right)^{1/4} \tag{4.3}$$

where τ is the peak bond shear stress in the adhesive; E_c' and η are the Young's modulus and thickness of the adhesive, respectively; and E_o, ν, and t_o are the Young's modulus, Poisson's ratio, and thickness of the outer adherend, respectively. The relationship between the non-dimensionalized geometric thickness parameter, defined by equation 4.4, and the ratio of the peak bond peel stress to the peak bond shear stress, is shown in Figure 4.31. The approximated values of the parameter associated with the joint bars of increasing moment of inertia are also shown.

Non-Dimensionalized Geometric Thickness Parameter:

$$\frac{3E_c'(1-\nu^2)t_o}{E_o\eta} \tag{4.4}$$

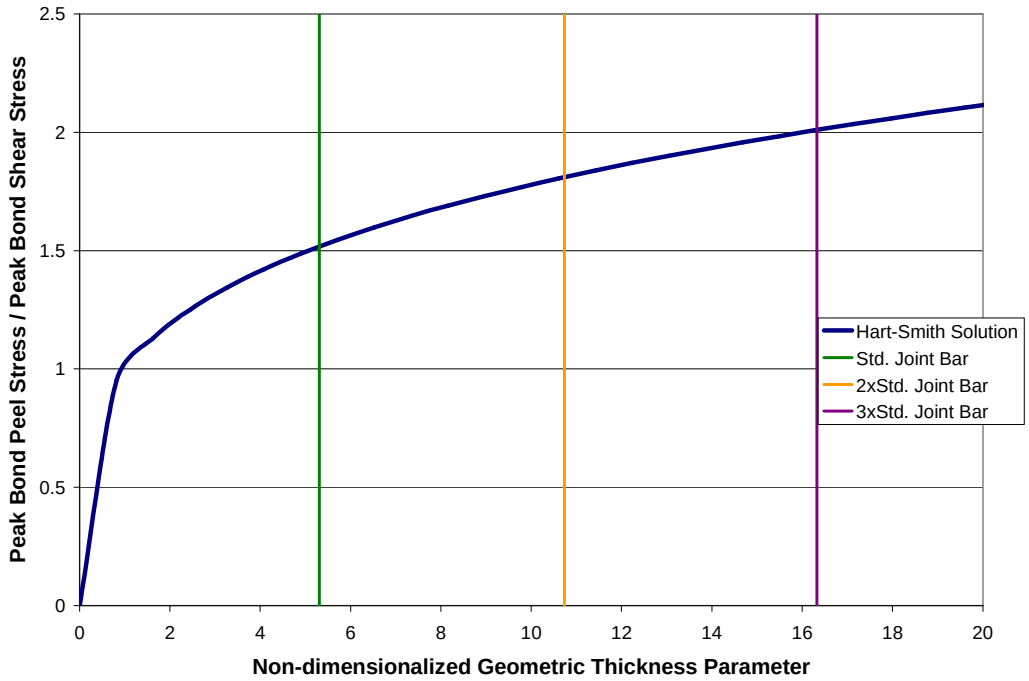

Figure 4.31: Elastic Peel Stresses in Double-Lap Joint

In the finite element model of the IJs with increasing joint bar moments of inertia, it was determined that the maximum out-of-plane shear stresses, both τ_{yz} and τ_{xy} , had very similar values for the varying moments of inertia. Thus, assuming that the peak bond shear stress is constant, maximum peel stress is directly related to the thickness of the outer adherend, meaning that as the stiffness of the outer adherend, or joint bars, increases, so does the peak maximum peel stress, as shown in Figure 4.31.

Hart-Smith also determined that the critical location, where the maximum peel stress and maximum shear stress occur, is at the termination of the outer adherends. This is consistent with the locations of maximum tensile peel stresses found in the finite element models throughout these results.

4.3.2 Load Between Ties

The displaced shapes of insulated joints composed of 36-in. joint bars with increasing moments of inertia, supported by 9-in. ties and subjected to an off-center wheel load, are depicted in Figure 4.32.

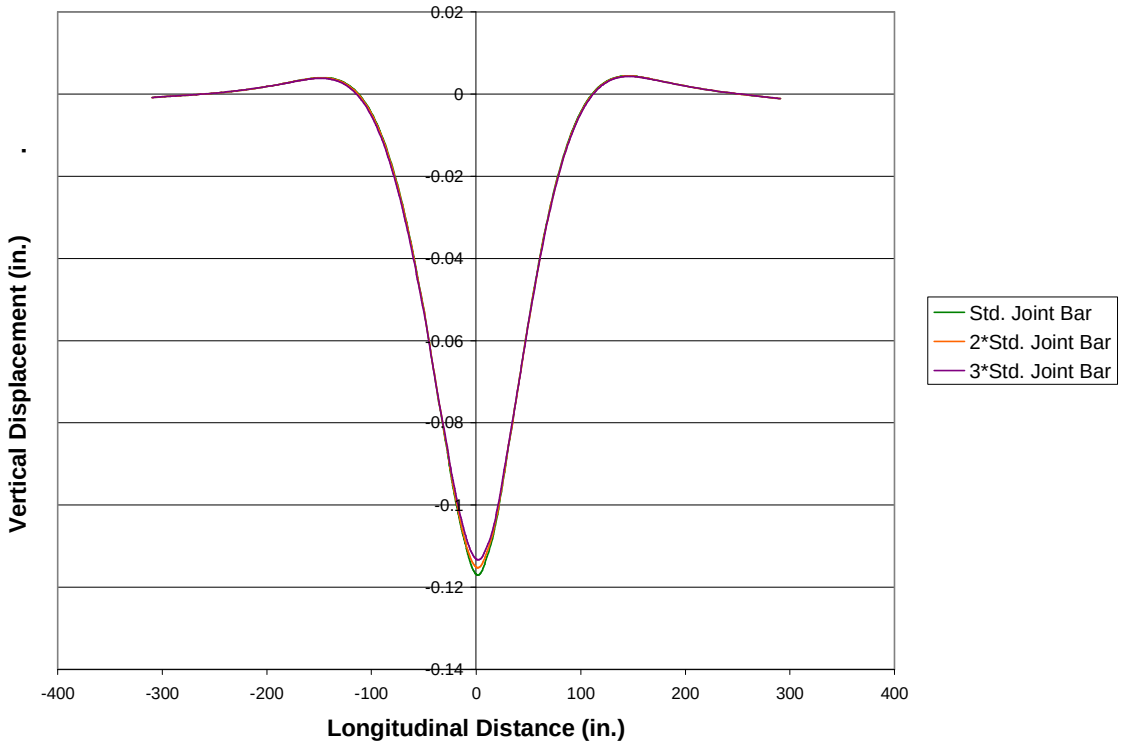

Figure 4.32: Displaced Shapes for Different Joint Bar Moments of Inertia; Load Between Ties

Again, the longitudinal distance of zero corresponds to the center of the wheel load application. As with the end post loading, the maximum deflections of the joint decrease with increasing moments of inertia. The maximum deflections of the standard, doubled, and tripled moment of inertia joint bars are 0.118 in., 0.116 in., and 0.114 in., respectively. However, this decrease in deflection is still over a small portion of the length, with the deflected shapes of the three models becoming indistinguishable at longitudinal distances close to the center of the loading. Also, as observed earlier, the maximum displacement of the joint does not occur directly below the center of the loading, due to the asymmetry of the "rail-joint" beam surrounding the load.

Figures 4.33 and 4.34 show the out-of-plane shear stresses, τ_{yz}, of the epoxy for an IJ composed of a 36-in. joint bar with a doubled moment of inertia and tripled moment of inertia, respectively. Both joints are supported by 9-in. ties and subjected to a vertical wheel load at between two ties. Figures 4.35 and 4.36 show the out-of-plane shear stresses, τ_{xy}, for these two joint models.

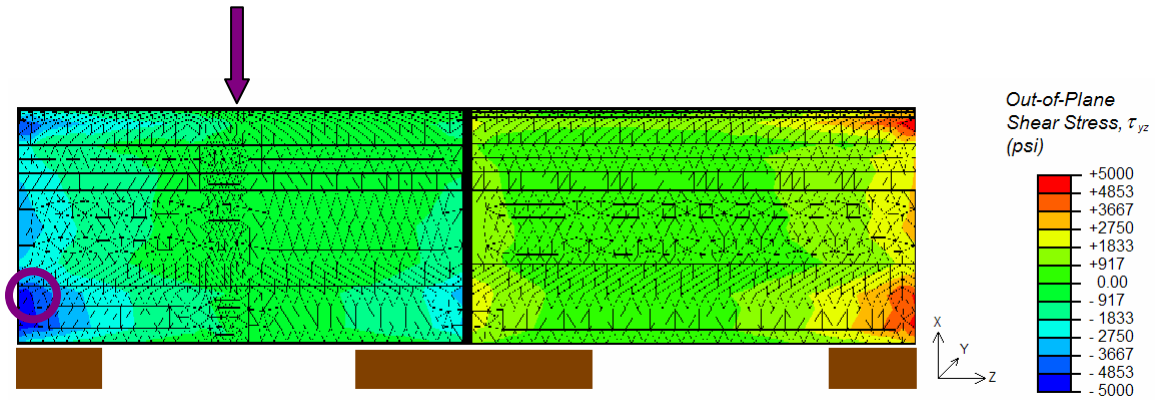

Figure 4.33: Out-of-Plane Shear Stress, τ_{yz}, in Epoxy; 9-in. Ties; 36-in. Joint Bars with 2*Std. Joint Bar Moment of Inertia; Load Between Ties

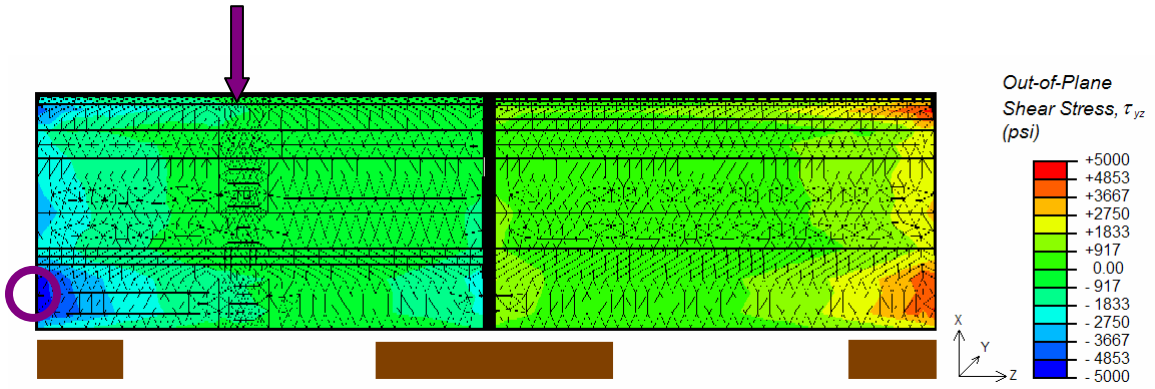

Figure 4.34: Out-of-Plane Shear Stress, τ_{yz}, in Epoxy; 9-in. Ties; 36-in. Joint Bars with 3*Std. Joint Bar Moment of Inertia; Load Between Ties

As seen with the end post loading, the maximum out-of-plane shear stress, τ_{yz}, shifts locations, from at the end post to the edge of the epoxy away from the end post. This again, is related to the increased stiffnesses of the joint bars and causes the both maximum out-of-plane shear stresses to occur at the edge away from the end post, in the bottom curve of the epoxy. The maximum out-of-plane shear stresses τ_{yz} for the standard, doubled, and tripled moment of inertia joint bars are 4,178 psi, 4,854 psi, and 5,209 psi, respectively. As opposed to the maximum τ_{yz} shear stresses found under the end post loading, these maximum values increase with an increasing joint bar moment of inertia. The maximum out-of-plane shear stresses, τ_{xy}, for the standard, doubled, and tripled moment of inertia joint bars are 1,212 psi, 1,554 psi, and 1,701 psi, respectively. The monotonic increases of these maximum τ_{xy} shear stresses are consistent with the increasing τ_{yz} shear stress values found with the end post loading of the same IJ models.

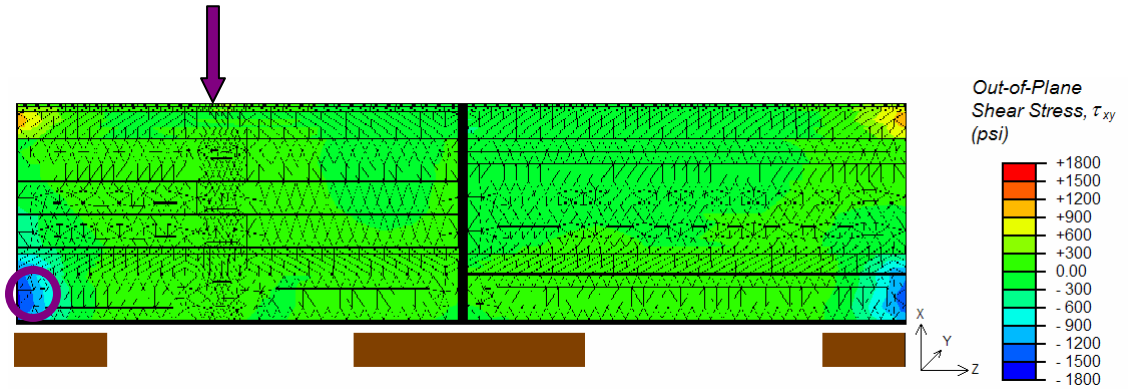

Figure 4.35: Out-of-Plane Shear Stress, τ_{xy}, in Epoxy; 9-in. Ties; 36-in. Joint Bars with 2*Std. Joint Bar Moment of Inertia; Load Between Ties

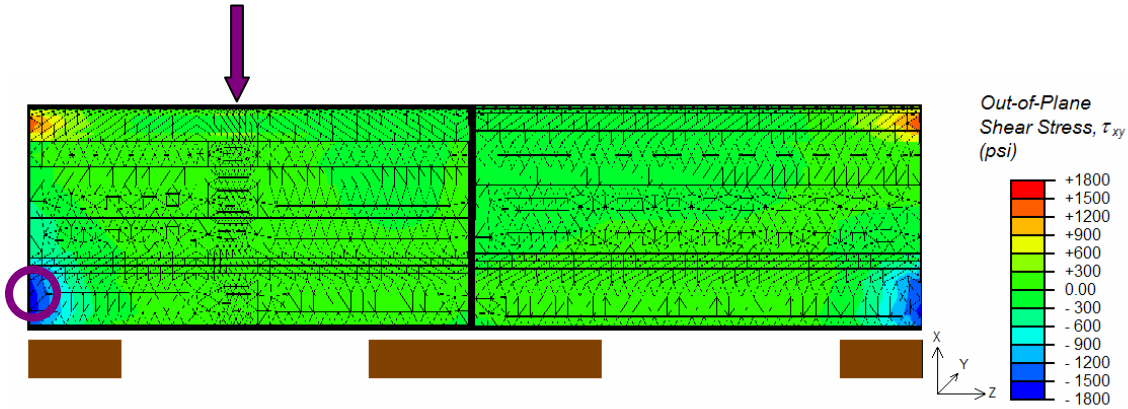

Figure 4.36: Out-of-Plane Shear Stress, τ_{xy}, in Epoxy; 9-in. Ties; 36-in. Joint Bars with 3*Std. Joint Bar Moment of Inertia; Load Between Ties

Figures 4.37 and 4.38 show the peel stresses associated with the increased moment of inertia joint bars subjected to loading between ties. Again, maximum compressive peel stresses occur below the vertical wheel loading. While the maximum tensile peel stresses again occur along an edge of epoxy away from the end post, with the increased moment of inertia joint bars, these maximums now occur in the epoxy connecting the joint bar to the unloaded length of rail.

The maximum compressive peel stresses for the standard, doubled, and tripled moment of inertia joint bars are 2,264 psi, 2,527 psi, and 2,594 psi, respectively. While the compressive stresses do increase with increasing moments of inertia, the rate of change for the increasing maximum tensile peel stresses is much more dramatic. The maximum tensile peel stresses for the standard, doubled, and tripled moment of inertia joint bars are 1,659 psi, 2,870 psi, and 3,464 psi, respectively.

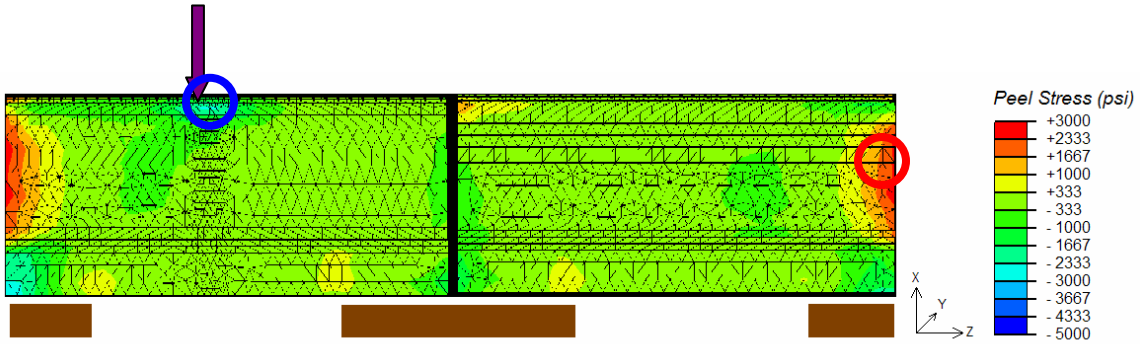

Figure 4.37: Peel Stress in Epoxy; 9-in. Ties; 36-in. Joint Bars with 2*Std. Joint Bar Moment of Inertia; Load Between Ties

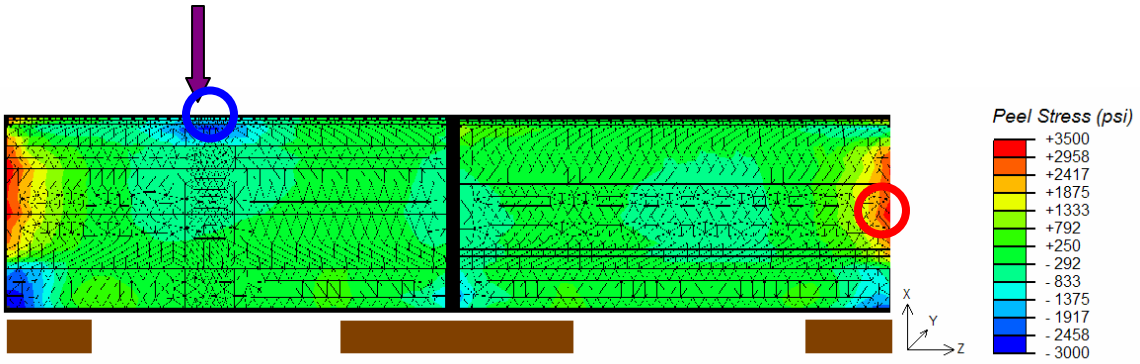

Figure 4.38: Peel Stress in Epoxy; 9-in. Ties; 36-in. Joint Bars with 3*Std. Joint Bar Moment of Inertia; Load Between Ties

CHAPTER 5 SUMMARY AND CONCLUSIONS

This goal of this research was to consider various designs of the supported insulated railroad joint to determine what practical changes could be made to the current design in order to increase the life expectancy of the IJ. Finite element models of these configurations were analyzed, varying tie width, joint bar dimensions, and wheel load locations. The resulting displacements, shear stresses, and peel stresses of these various arrangements were compared to ascertain each parameter's influence on the joint.

5.1 Summary of Results

5.1.1 Tie Width

Increasing the tie width from 9 in. to 11 in. decreases the maximum displacement of the joint by 24%. The effect of increasing the tie width on the maximum shear and peel stresses is very minimal, as shown below in Figures 5.1 and 5.2.

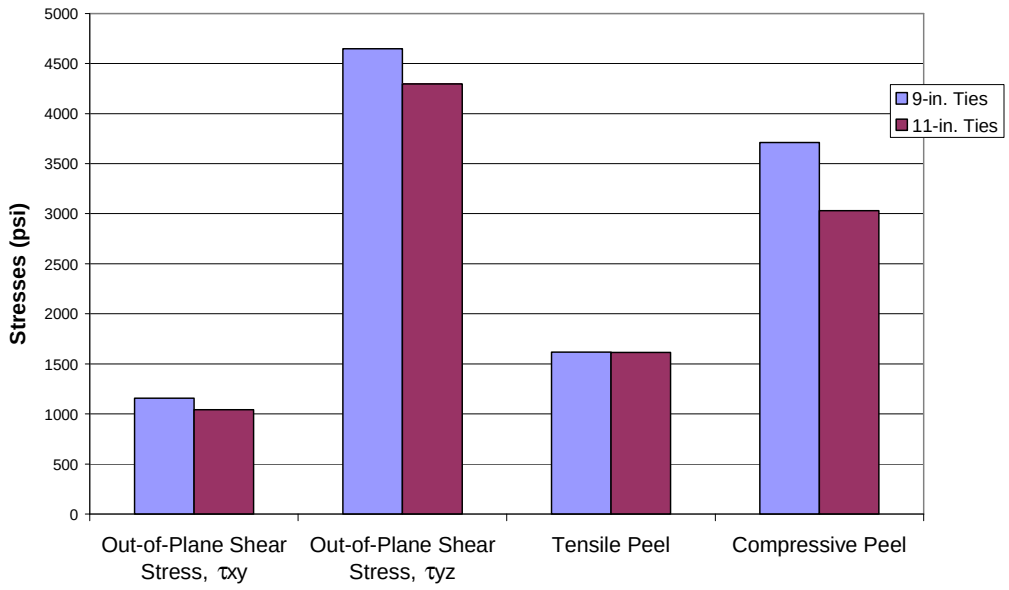

Figure 5.1: Comparing Maximum Stresses for Different Tie Widths; End Post Loading

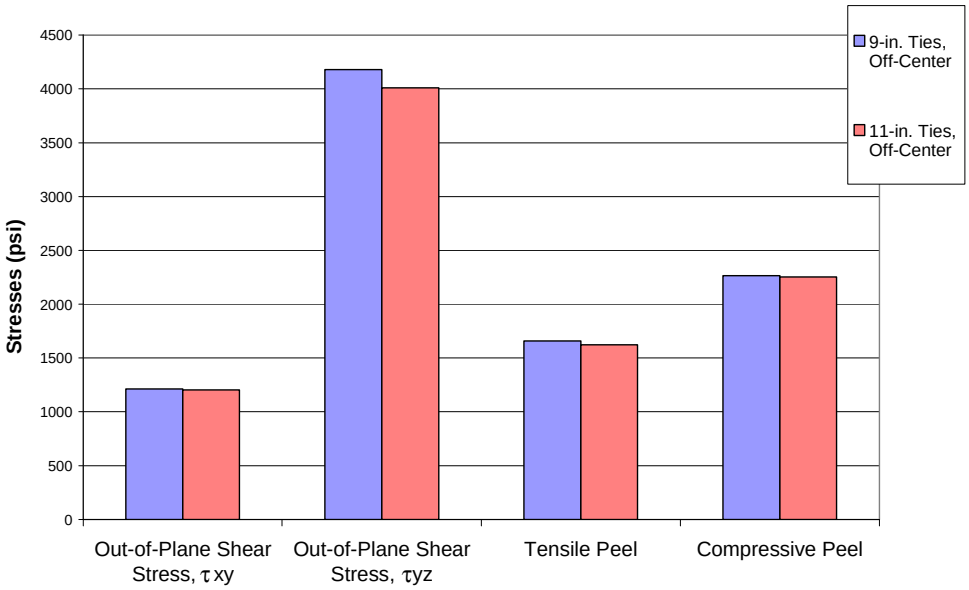

Figure 5.2: Comparing Maximum Stresses for Different Tie Widths; Load Between Ties

5.1.2 Joint Bar Length

Increasing the joint bar length from the standard 36 in. to 48 in. has virtually no effect on the maximum deflection. Similarly, the increased length has very little influence on the maximum stresses observed in the epoxy, as seen in Figure 5.3.

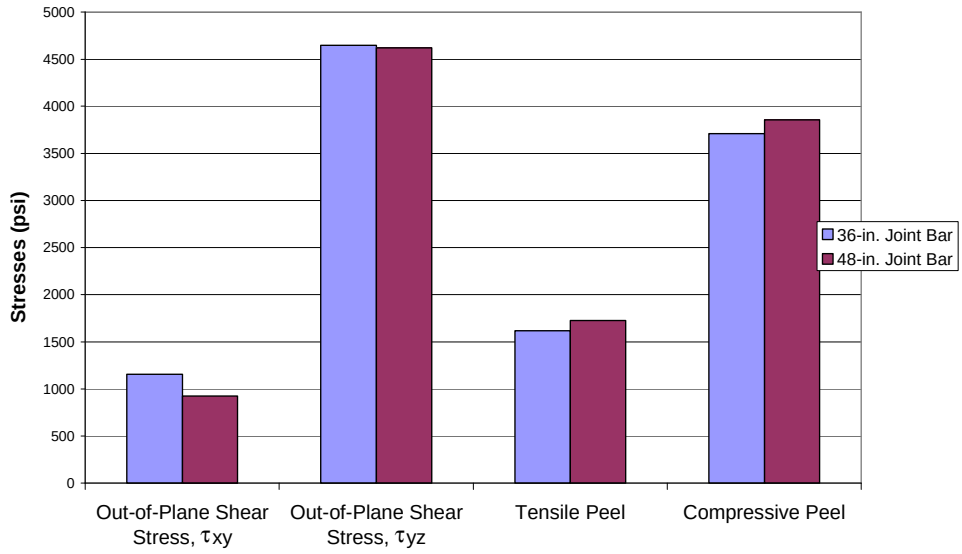

Figure 5.3: Comparing Maximum Stresses for Different Joint Bar Lengths

5.1.3 Joint Bar Moment of Inertia

Increasing the joint bar moment of inertia has a small effect on the maximum displacement, as shown below in Figure 5.4. The first bar corresponds to a continuous rail with no joint, supported by 9-in. ties, similar to the joint bar models also shown in the figure.

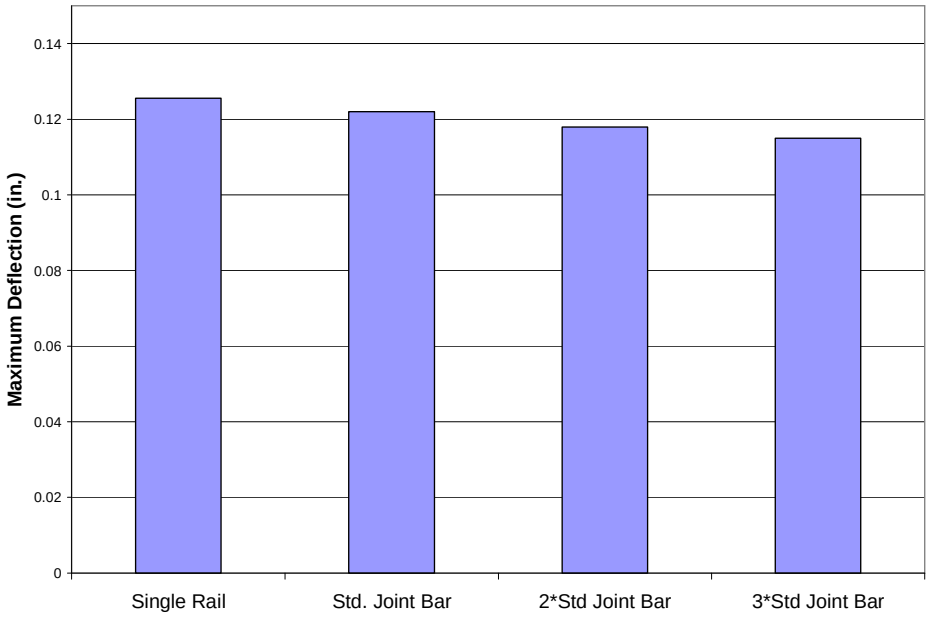

Figure 5.4: Maximum Displacements for Increasing Joint Bar Moments of Inertia

As one would suspect, adding the joint bars to the single length of single rail, which increases the moment of inertia and thus the stiffness of the "joint-rail beam", decreases the maximum deflection. This trend continues with doubling and tripling the moment of inertia of the joint bar.

Shown in Figure 5.5 is a plot of the relative displacement for to the native rail for the joints with increasing joint bar moments of inertia, longitudinally along the rail. This shows the values of the displacement found in the IJ finite element models, when the wheel load is at the end post as well as when it is placed between two ties. The displacements along the remaining lengths of rail are values from the earlier analysis of a single rail subjected to a vertical wheel load. As seen in the figure, when the end post of the joint is supported by a tie, a bump exists at over the length of the joint. The relative height of this bump increases as the joint bar moment of inertia increases. The existence of such a bump could cause the train to accelerate as it travels over the joint, increasing the impact forces on the joint from the wheel.

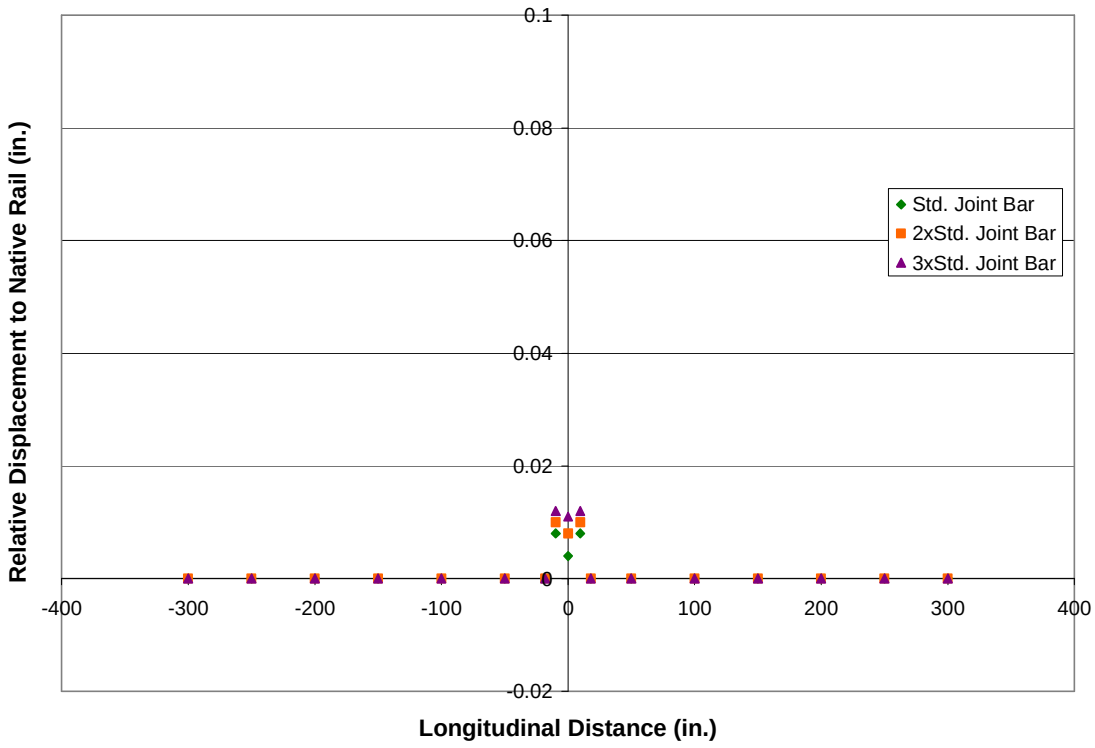

Figure 5.5: Relative Displacement Longitudinally Along Rail

However, as shown in Figure 5.6, the maximum peel stresses observed in the epoxy increase dramatically with the increasing moment of inertia, and the maximum shear stresses also tend to increase. This monotonic increase in stresses is also seen when the load is moved to a location halfway between two ties, as shown in Figure 5.7.

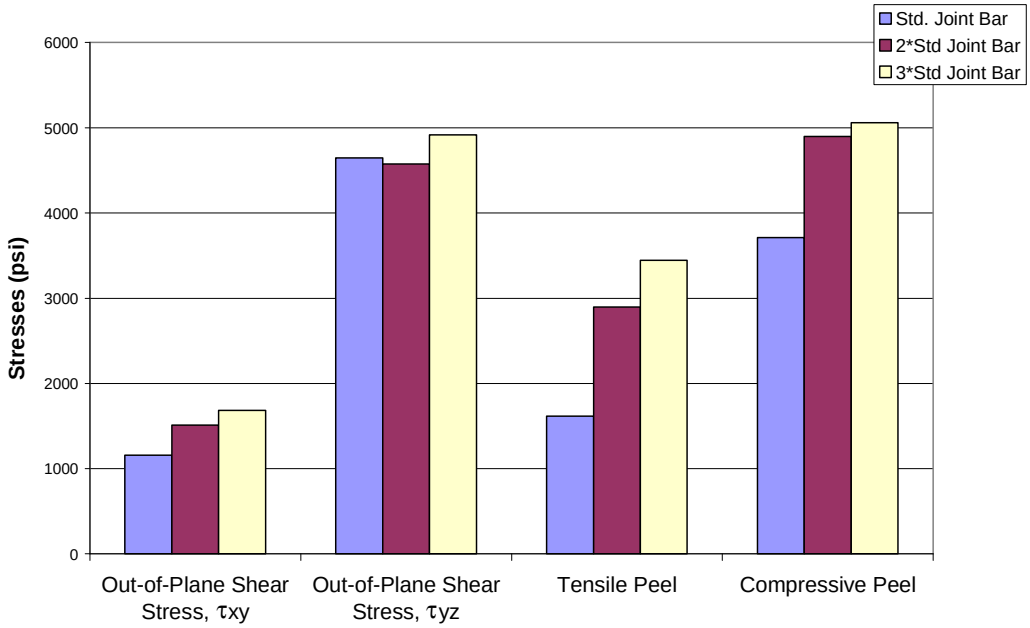

Figure 5.6: Comparing Maximum Stresses for Different Joint Bar Moments of Inertia; End Post Loading

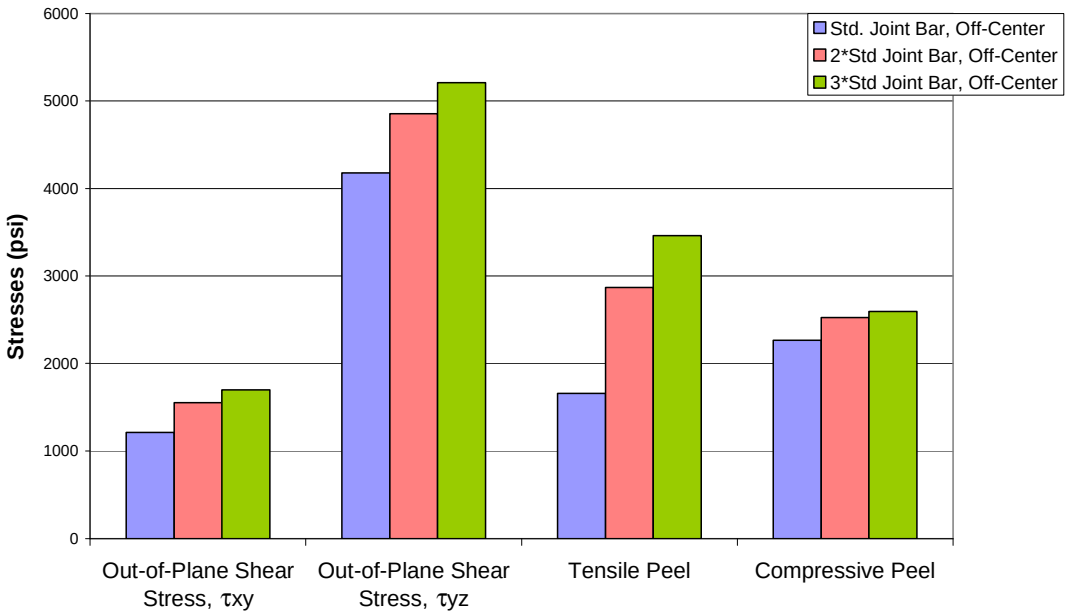

Figure 5.7: Comparing Maximum Stresses for Different Joint Bar Moments of Inertia; Load Between Two Ties

5.1.4 Wheel Load Location

Placing the vertical wheel load directly between the tie beneath the end post and an adjacent tie decreases the maximum displacement. This wheel load location also yields similar maximum shear and peel stresses, as well as similar relationships between those stresses for varying parameters, as when the loading was placed at the end post. However, in placing the wheel load between ties for the standard 36-in. joint bar models, the maximum tensile peel stress occurs at the end post, which may help cause many bond failures to initiate near the end post.

5.2 Conclusions

For all insulated joint finite element models analyzed, the displaced shape of the joint and surrounding rail follow the shape predicted by Hetényi's beam on elastic foundation theory for an infinite beam subjected to a single concentrated load (Hetényi, 1946).

In the epoxy between the joint bars and the rail, maximum out-of-plane shear stresses, as well as maximum tensile stresses, are consistently located along an edge of the epoxy, with the maximum shear stresses typically being found in the upper and lower curves of the epoxy near the top and bottom of the joint bar. The phenomenon of shear lag, as predicted by Volkersen (1946), is also observed for the out-of-plane shear stresses. The maximum compressive peel stress in the epoxy is found to be located just below the center of the application of the vertical wheel load. Compressive peel stress concentrations also tend to be located above tie locations.

From this research, increasing the tie width, the joint bar length, and the joint bar moment of inertia does not significantly decrease the maximum stresses present in the epoxy of the insulated rail joint. Increasing the joint bar moment of inertia has the opposite effect, dramatically increasing the stresses found in the epoxy.

In comparing these results of a supported IJ composed of standard 36-in. joint bar, supported by 9-in ties with a wheel load placed at the end post, with those of a suspended joint with the same components found by Adric Eckstein in earlier research, supporting the joint decreases the maximum displacement by 15% and decreases the maximum shear stress by 28%.

5.3 Recommendations for Further Research

While this thesis focused on the static loading of the insulated rail joint, very little research has been performed using finite element analysis to model the dynamic loading of the joint. Impact loads can be significantly higher than static loads, especially when combined with larger

displacements. From this research it was determined that by increasing the tie width, the maximum displacement of the joint was significantly decreased, while the stresses were minimally affected. This deflection decrease and resulting stresses could become more significant when impact loading is taken into account. Repeated dynamic loading of the joint also results in fatigue of the IJ, causing damage and wear on the rail head as well as degradation of the ballast and subgrade supporting the joint. This topic should be investigated.

The dynamics related to the wheel passing over the insulated joint can be used in modeling not only the standard butt joint, but the tapered joint as well. Earlier research conducted by Adric Eckstein, Seth Lambrecht, and Heike Lohse-Busch showed that by tapering the joint, the shear stresses in the epoxy could be reduced by two-thirds.

Finally, implementation of the design recommendations resulting from this and related work must ultimately be tested in the field to determine if in fact the life expectancy of the insulated railroad joint can be increased by varying some of the parameters considered here.

References

ABAQUS (2004). *ABAQUS/CAE User's Manual, v.6.5*, ABAQUS, Inc., Pawtucket, RI.

Adams, R. D., Comyn, J., and Wake, W. C. (1997). *Structural Adhesive Joints in Engineering*, 2nd ed. Chapman and Hall, London, UK.

Bogdanovich, A. E. and Kizhakkethara, I. (1999). "Three-dimensional Finite Element Analysis of Double-Lap Composite Adhesive Bonded Joint Using Submodeling Approach." *Composites Part B*, Vol. 30, pp. 537-551.

Burton, P. (1975). "A Review of Rail Wheel Contact Stress Problems." *Proceedings of Symposium on Railroad Track Mechanics.* Pergamon Press, Englewood Cliffs, NJ.

Campilho, R. D. S. G., de Moura, M. F. S. F., and Domingues, J. J. M. S. (2005). "Modeling Single and Double-Lap Repairs on Composite Materials." *Composites Science and Technology*, Vol. 65, pp. 1948-1958.

Chen, Y. C. (2003). "The Effect of Proximity of a Rail End in Elastic-Plastic Contact Between a Wheel and a Rail." *Proceedings of the Institution of Mechanical Engineers, Part F, Journal of Rail and Rapid* Transit, Vol. 217, pp. 189-201.

Chen, Y. C. and Kuang, J. H. (2002). "Contact Stress Variations Near the Insulated Rail Joints." *Proceedings of the Institution of Mechanical Engineers, Part F, Journal of Rail and Rapid Transit*, Vol. 216, No. 4, pp. 265-273.

Dillard, David A., Plaut, R., Dillard, John G. (2006) "2006 Project: Characterizing and Improving Insulated Joint Performance." Virginia Tech.

Davis, D. D., Collard, D., and Guillen, D. G. (2004). "Bonded Insulated Joint Performance in Mainline Track." *Technology Digest*, May, 2004.

Dukkipati, R. V. (2000). *Vehicle Dynamics*. CRC Press, Boca Raton, FL.

Eckstein, A., Lohse-Busch, H., Dillard, D. A., and Plaut, R. H. (2005). "Shear and Deflection Analysis in Conventional and Tapered Bonded Insulated Rail Joints." Technical Report, Virginia Tech, Blacksburg, VA.

Hart-Smith, L. J. (1973). "Adhesive-Bonded Double-Lap Joints." Technical Report, Langley Research Center, NASA, Hampton, VA.

Hua, Y., Crocombe, A. D., Wahab, M. A., and Ashcroft, I. A. (2006). "Modeling Environmental Degradation in EA9321-Bonded Joints Using a Progressive Damage Failure Model." *Journal of Adhesion*, Vol. 82, pp. 125-160.

Hertz, H. (1882). "Über die Berührung fester elastischer Körper." *J. reine und angewandte Mathematik*, Vol. 92, pp. 156-171.

Hetényi, M. (1946). Beams on Elastic Foundation: Theory with Applications in the Fields of Civil and Mechanical Engineering. The University of Michigan Press, Ann Arbor, MI.

Indraratna, B. and Wadud, S. (2005). *Mechanics of Ballasted Rail Tracks: A Geotechnical Prospective*. Taylor & Francis, London, UK.

Jeffs, T., Tew, G. P. (1991). "A Review of Track Design Procedures" *Railways of Australia*, Vol. 2.

Kerr, A. D. (2003). *Fundamentals of Railway Track Engineering.* Simmons-Boardman Books, Omaha, NE.

Kerr, A. D. and Cox, J. E. (1999). "Analysis and Tests of Bonded Insulated Rail Joints Subjected to Vertical Wheel Loads." *International Journal of Mechanical Sciences*, Vol. 41, pp. 1253-1272.

Lambrecht, S. and Lohse,Busch, H. (2006). "Improved Designs for Insulated Railroad Joints." Technical Report, Virginia Tech, Blacksburg, VA.

Matthews, F. L., Tsai, M. Y., and Morton, J. (1994). "Experimental and Numerical Studies of a Laminated Composite Single-Lap Adhesive Joint." *Journal of Composite Materials*, Vol. 29, No. 9, pp. 1254-1275.

Profillidis, V. A. (2000). *Railway Engineering*. Ashgate, Burlington, VT.

Volkersen, O. (1938). "Die Nietkraft Verteilung in zugbeanspruchten Nietverbindungen mit konstanten Laschenquerschnitten." *Luftfahrtforschung*, Vol. 15, pp. 41-47.

Wen, Z., Jin, X., and Zhang, W. (2005). "Contact-Impact Stress Analysis of Rail Joint Region Using the Dynamic Finite Element Method." *Wear*, Vol. 258, pp. 1301-1309.

Winkler, E. (1867). "Die Lehre von der Elasticitaet und Festigkeit." *H. Dominicus*, Tiel 1, 2.

Yang, C., Huang, H., Tomblin, J. S., and Sun, W. (2003). "Elastic-plastic Model of Adhesive-bonded Single-lap Composite Joints." *Journal of Composite Materials*, Vol. 38, pp. 293-309.

Zgoul, M. and Crocombe, A. D. (2003). "Numerical Modeling of Lap Joints Bonded with a Rate-Dependent Adhesive." *International Journal of Adhesion and Adhesives*, Vol. 24, pp. 355-366.

Appendix A

Mesh Convergence Study Details

The meshes used for the convergence study are described in the tables and figures below. All meshes were composed of solid tetrahedral elements of varying sizes. Shown in Figure A.1 is an isometric view of the finite element model rail used in the mesh convergence study. The yellow arrow shows where the vertical wheel load was applied, which is also the center of the length of rail.

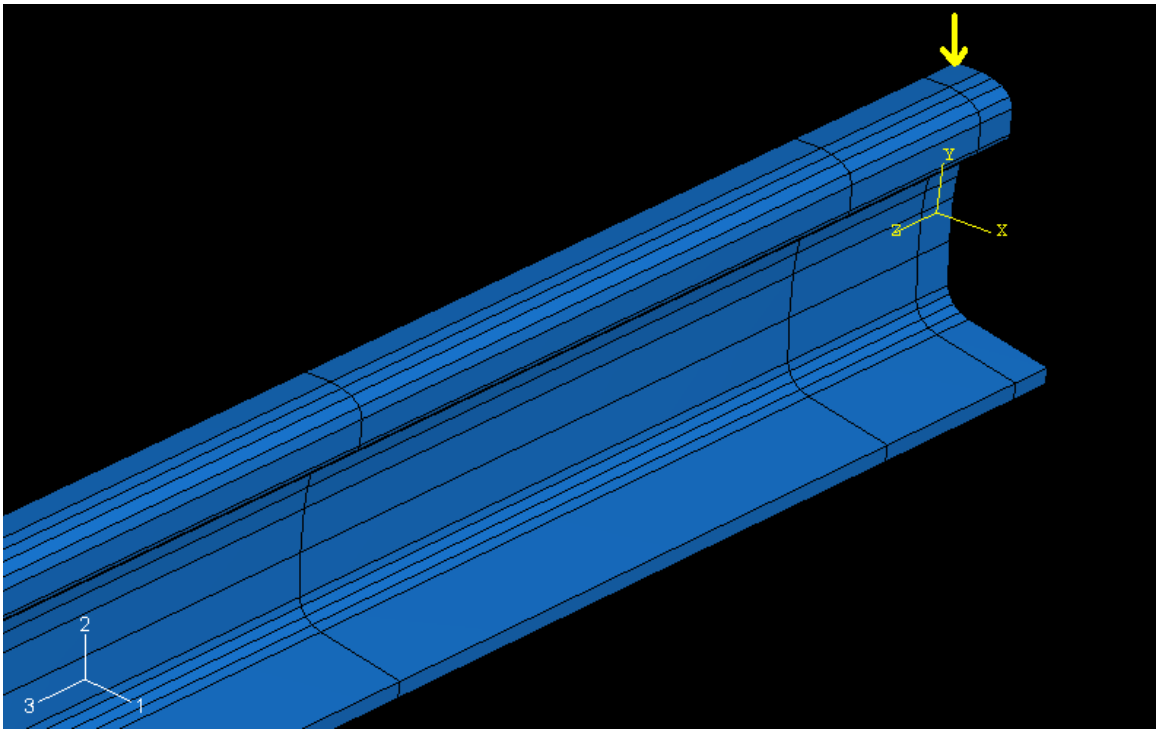

Figure A.1: Isometric View of Rail Model Used in Mesh Convergence Study

The following tables list the length of the region over which an element size was specified, as well as the distance from the center line of the rail (where the vertical wheel load and symmetry were applied) to the start of the region. Also noted in the tables is the element size used over the region, which is the length of the sides of the solid tetrahedral elements used in the finite element model. The figures depict both the entire mesh of the rail, as well as a close-up view of the region of the rail adjacent to the center line of the rail. The view of the meshes is of the plane of symmetry along the length of the rail, which is the Y-Z plane in Figure A.1.

A.1 Mesh 1

Distance from Center Line to Start of Region (in.)	Length of Region (in.)	Element Size (in.)
0	1	0.5
1	4	0.75
5	15	1.5
20	30	3
50	75	5
125	75	6.82
200	100	10

Table A.1: Mesh 1 Details

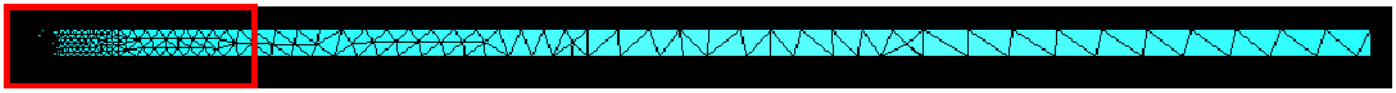

(a)

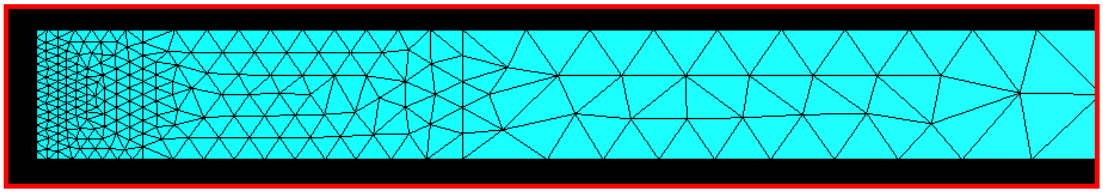

(b)

Figure A.2: Mesh 1: (a) Entire Rail Model, (b) Close-Up Near Load Application Point

A.2 Mesh 2

Distance from Center Line to Start of Region (in.)	Length of Region (in.)	Element Size (in.)
0	1	0.25
1	4	0.5
5	15	0.75
20	30	1.5
50	75	3
125	75	5
200	100	7

Table A.2: Mesh 2 Details

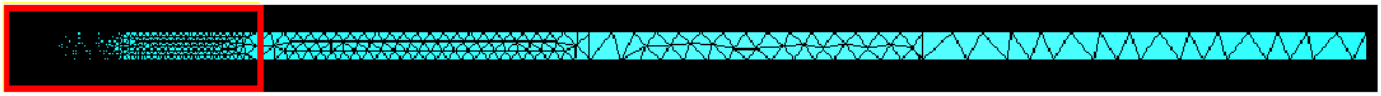

(a)

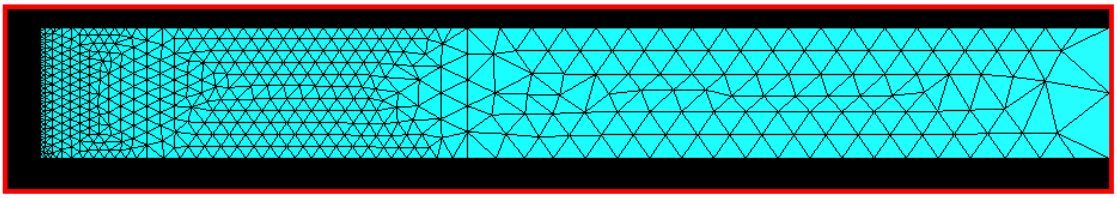

(b)

Figure A.3: Mesh 2: (a) Entire Rail Model, (b) Close-Up Near Load Application Point

A.3 Mesh 3

Distance from Center Line to Start of Region (in.)	Length of Region (in.)	Element Size (in.)
0	1	0.25
1	4	0.5
5	175	1
180	120	5

Table A.3: Mesh 3 Details

(a)

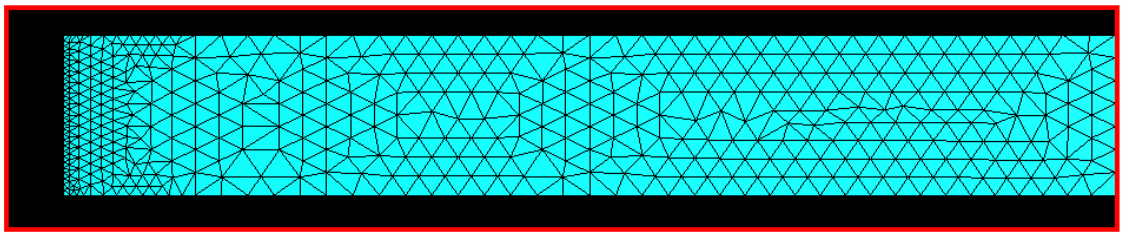

(b)

Figure A.4: Mesh 3: (a) Entire Rail Model, (b) Close-Up Near Load Application Point

A.4 Mesh 4

Distance from Center Line to Start of Region (in.)	Length of Region (in.)	Element Size (in.)
0	1	0.25
1	4	0.5
5	295	1

Table A.4: Mesh 4 Details

(a)

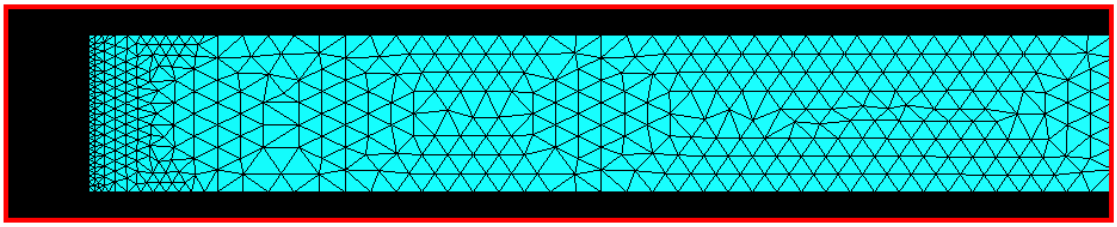

(b)

Figure A.5: Mesh 4: (a) Entire Rail Model, (b) Close-Up Near Load Application Point

Appendix B

Details of Mesh Used in Finite Element Models of Insulated Railroad Joints

The following figures depict the mesh used for the insulated railroad joint composed of a 136 RE rail and a 36-in. standard joint bar, subjected to a vertical wheel load at the end post, and supported by 9-in. ties. Similar meshes were used for all other configurations of the insulated railroad joints investigated in this research.

Figure B.1 shows an isometric view of the IJ mesh used in this research.

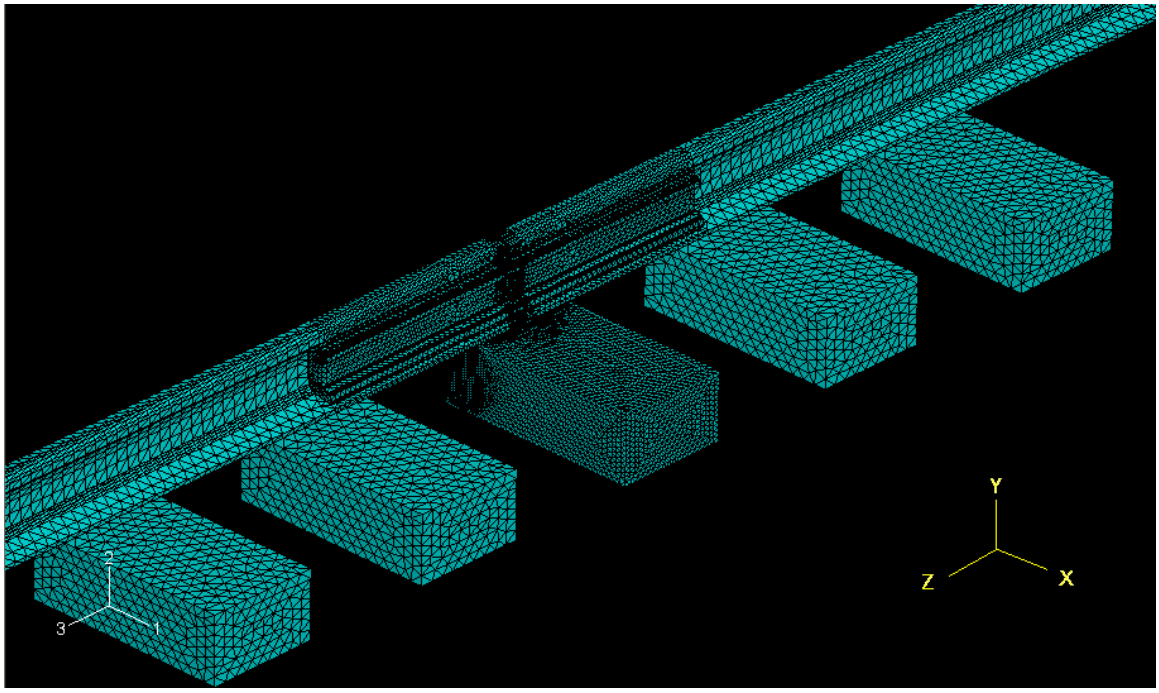

Figure B.1: Isometric View of IJ Model Mesh

Since the finite element mesh is symmetric about the center line of the joint, only half of the IJ and the extended rail are shown in Figures B.2 (a) and B.2 (b). Again, Figure B.2 (a) depicts the entire mesh of the rail, and Figure B.2 (b) shows a close-up view of the region of the rail adjacent to the center line of the joint. The view of the meshes is of the plane of symmetry along the length of the rail, which is the Y-Z plane in Figure B.1.

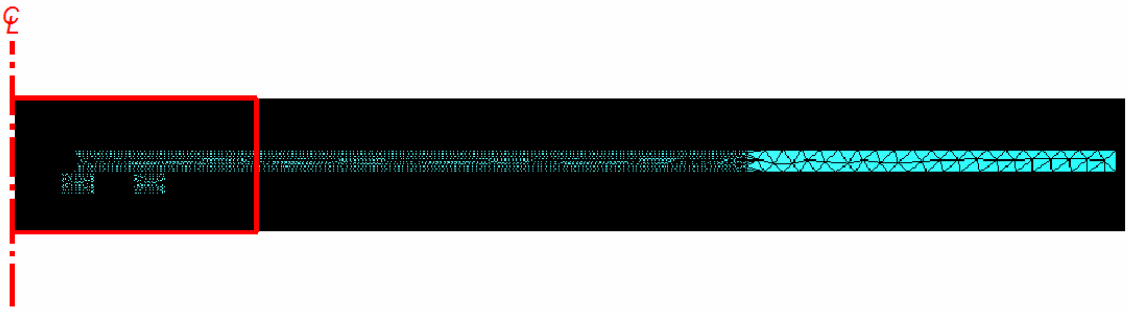

(a)

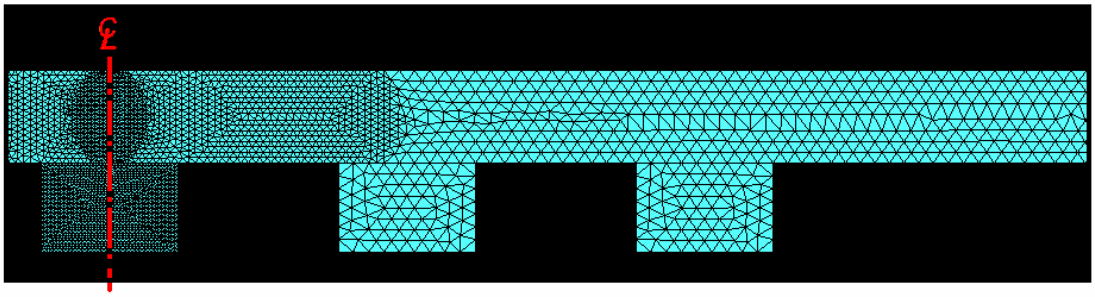

(b)

Figure B.2: IJ Model Mesh: (a) Half of Model, (b) Close-Up Near Load Application Point (End Post)

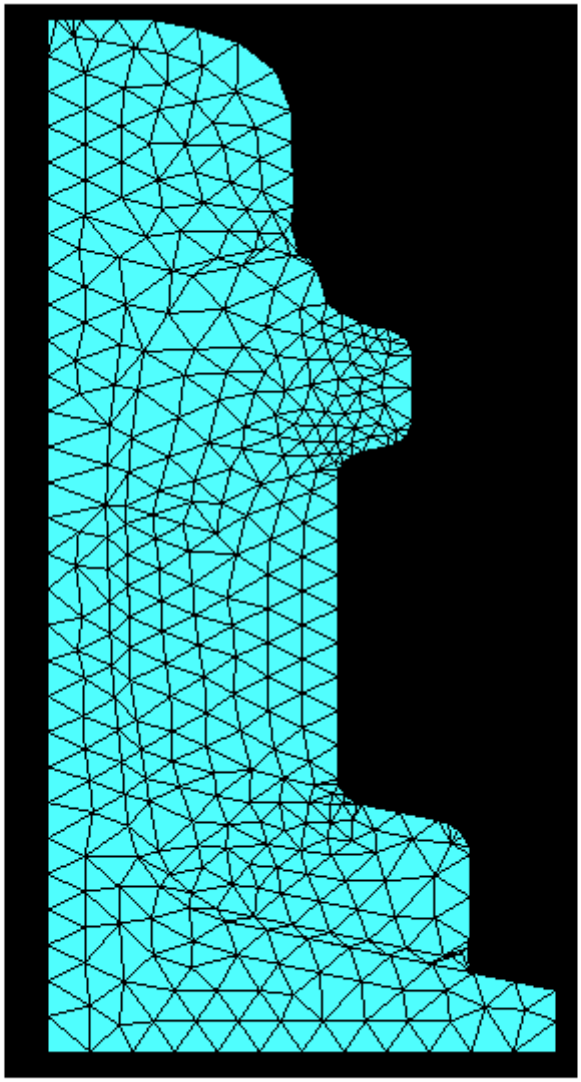

Figure B.3: Cross-section of IJ Model Mesh

Vita

Anne K. Himebaugh was born on October 15, 1981 in Mariemont, Ohio. She spent her childhood in Cincinnati, Ohio, graduating from Turpin High School in May 2000. She attended Purdue University and participated in their University Sponsored Cooperative Education Program. Anne graduated with a Bachelor of Science in Civil Engineering in May 2005. She then continued her studies at Virginia Polytechnic Institute and State University with a Via Fellowship to pursue a Master of Science in Civil Engineering. Upon the completion of her degree in December 2006, Anne will begin her career at Simpson, Gumpertz, and Heger in Waltham, Massachusetts.